Various Continuum Bone Remodelling Algorithms Applied to the Proximal Femur in Two and Three Dimensions

by
Martin Stülpner BSc(Hons)

A thesis submitted to the University of Cape Town
in partial fulfilment of the requirements for the degree of
Master of Science in Applied Science

Department of Mechanical Engineering
University of Cape Town
Rondebosch
South Africa
October 3, 1995

Dedicated to my parents, who have put up with me for so long, and to my sister Katrin, so that she may find her feet in the world, and travel down a path at least as enjoyable and rewarding as the one that I was privileged to have been able to follow.

„Kunst kommt von Können;
denn was man kann,
das ist keine Kunst nicht mehr."
Karl Stülpner

Acknowledgements:

I would like to acknowledge the assistance offered by my supervisor, Professor B.D. Reddy, as well as my co-supervisor, Mr T. Spirakis. Their enthusiasm and encouragement have been invaluable, and it is owing to the expertise of each of them in their own field that I have been able to largely achieve the goals that had been set at the beginning of this project. To Prof Reddy, thank you very much for reading and correcting so many revised versions of various chapters in such a short time. Special thanks also to Greg Starke, who was always prepared to help when I had a seemingly insurmountable problem, and put me back on the right track with his sensible, hands-on engineering approach and never-absent sense of humour. Thanks to Damian Conway for introducing me to some of the finer points of using the software, and to Mike Eastman for always being willing to listen to and answer computer-related questions. Thanks also to Chris Jacobs, formerly of Stanford University, who provided me with a basis to work from in the form of his PhD dissertation, and who was always on line to discuss bone remodelling via the internet. Very special thanks must go to Katy Sunter for looking after me so well when I had to work all night, and for always lending me moral support, encouraging me in my work, and for supplying me with neverending amounts of absolutely delicious food.

Contents

Abstract

This study investigates the behaviour of bone when it is subjected to mechanical loading. This is important in fields such as orthopaedics and implant design. Various models of bone remodelling are discussed, and a strain energy based as well as a strain remodelling based algorithm are applied in two and three dimensions. Properties such as dependence on initial conditions, development of physiologically realistic solutions and existence of long-term steady states are investigated. The strain based model has some advantages in that it is defined in terms of physiologically meaningful and measurable parameters and that it develops a long-term steady state solutions different from the case where the bone either resorbs completely or reaches cortical density.

Chapter 1

Introduction and Literature Review

Bone mechanics is the study of how bone reacts to mechanical influences. The aim is to model the behaviour of bone under normal physiological mechanical loading, as well as its adaptation to loading conditions that are not physiological. In this work, several mathematical and computer models are presented and their advantages and disadvantages discussed.

Bone mechanics has applications in orthopaedics, for example, where researchers and practicioners are interested in how the growth of a pathological bone differs from that of a healthy one, or how a common malady such as osteoarthritis is influenced by the mechanical loading conditions.

Another important motivation for studying bone mechanics is implant design. This is of concern to the hundreds of thousands of people around the world who rely on artificial joints or bone prostheses to make their lives easier. In 1983 already it was estimated that a total volume of 400 000 prosthetic joint implantations were performed annually [40]. Especially common are artificial hips and knees, but prostheses have also been designed for other joints such as elbows and fingers. Implants have been manufactured for more than thirty years now [61], and clearly a better understanding of the mechanical properties of the bone around such prostheses will lead to improved prosthesis design and longer trouble-free prosthesis life. Computer simulations allow new prosthesis shapes to be designed, thus avoiding the need to implant the new design into a patient, and then to evaluate its performance *in situ*, as was the approach in the early stages of implant design [15].

The study of bone mechanics can be traced back as far as Galileo [1], who studied the

influence that the size of an animal has on the structure of its bones. He had earlier demonstrated that the dimensions of a structure determine the size of its components, and applied this principle to the skeleton. Galileo understood that bone is a material but at the same time forms a structure.

Today it is understood that bone has to function on three levels: on a material level, a structural level and a system level [68]. The most important function of bone as a material is to supply the body with calcium and other minerals needed for survival. Bone material is arranged so as to form structures which perform a load-carrying function in the body: the bony skeleton supports the rest of the anatomy, provides some stiffness, and protects various organs such as the heart and the brain from outside influences. The way in which bone reacts to external loads by laying down new bone tissue in certain places and dissolving tissue in others is called *remodelling*. An in-depth discussion of this is provided in Section 1.2, but it can be pointed out at this stage that the ability of bone to remodel indicates that bone works as a feedback system which adapts to mechanical stimulation by altering its structure. To simulate bone on the material, structural and system levels is a very challenging engineering problem indeed as mechanical, biological and biochemical variables have to be taken into account [17].

The layout of the rest of this chapter is as follows. In Section 1.1, a description of the aims and the layout of the thesis as a whole is given. In Section 1.2, a closer look at the mechanical properties of bone in general and remodelling in particular is taken. Some of the physiology relevant to bone remodelling is described in Section 1.3 and the idea of a remodelling stimulus is discussed in Section 1.4. Finally, in Section 1.5, the study of bone mechanics is motivated by considering some aspects of prosthesis design. The purpose of the chapter is to give an introduction to the work in orthopaedic biomechanics and lay the groundwork for the chapters that follow.

1.1 Aims and Layout

The chief objective of this study is to investigate theories of bone remodelling, and to solve the remodelling equations using a finite element model of a real-life geometry such as the proximal femur (see Section 1.3 for details). The goal is to reproduce physiological structure by applying the correct remodelling laws in the correct loading environment to an initially uniformly dense piece of bone. This study builds on the work of Cowin [25], Jacobs [47] and others.

The layout of this thesis is as follows: Chapters 2 and 3 are devoted to an overview of the mechanical and computational background necessary for the study in question. Thus in Chapter 2, basic continuum mechanics is reviewed and in Chapter 3, the finite element method, which is the numerical method to be used in this study, is presented. Chapter 4 reviews a strain energy based bone remodelling algorithm developed by Carter, Jacobs and others [47] [13], which forms the basis on which further work in this thesis is built. In Chapter 5 more literature is reviewed with the aim of establishing strain as the main remodelling criterion, and a strain-based remodelling algorithm is presented. Chapter 6 shows how the work reviewed in Chapter 4 is extended to three dimensions. Computational results are presented in Chapter 7, and in Chapter 8, these results are discussed and conclusions presented.

1.2 Mechanical Properties of Bone and Bone Remodelling

Bones provide a solid foundation to which muscles and tendons are attached. They are, however, only a part of the vertebrate physiology: without the surrounding and penetrating tissue they are brittle and not nearly as solid as in vivo. For example, wet bone specimens yield and undergo plastic deformation, while dry specimens undergo brittle failure. Thus when one considers the mechanical behaviour of cancellous bone, one has to draw the distinction between bone *in vivo* and dead bone, for these exhibit completely different structural responses to applied loads.

Modern methods of determining physical properties such as elastic or shear moduli include ultrasonic techniques, holography, and even mechanical testing [30] [28] [3]. As bone as a material is inherently anisotropic, a large number of structural constants are required to describe its material properties. The elasticity tensor C linking the stress σ and the elastic strain ϵ has a total of 21 independent components. Bone exhibits some structural symmetry and so it can be modelled as orthotropic, which means that the number of independent components of C reduces to 9 [3]. The problem about mechanical testing is that one can only obtain a maximum of 4 out of these 9 structural constants from one test specimen [3]. Also, there are many experimental complications that occur when bone is tested mechanically. An example is that measured properties such as the elastic modulus are highly dependent on experimental boundary conditions such as the friction between the testing rig and the bone surface [76]. Another complication is that the stress-strain

curve appears to be nonlinear due to edge effects of crushing bone struts when the bone is cut and first loaded [76]. This is an experimental artifact as, for small deformations at least, bone is a cellular solid which is linear elastic [2].

The most interesting feature in living bone tissue is *remodelling*: bone growth adapts to external stresses. If the force applied to the bone is greater than a certain equilibrium value, the bone grows or increases its density (this is termed *apposition*). If it is less than an equilibrium value, the bone starts dissolving or *resorbing*. This is why astronauts have to do regular exercise while they are in orbit: if they do not, their bones will resorb because the usual gravitational force of the Earth is not present in orbit. The gradient in bone density in the group of lumbar vertebrae that is present in the Earth's gravitational field has been shown to vanish in astronauts that have spent long periods of time in space [26]. According to Field and Kenyon [33], bone grows in such a way as to offer maximal structural support using a minimum of calcified material. It was the observation of the orientations of bone struts in a cross-section of the human femoral head and a comparison of this with the principal stress trajectories in a so-called Cullmann crane (see Figure 1.1) that led to the formulation of Wolff's law (1892), which states that the trabeculae, the small struts making up the bone matrix, grow along the principal stress trajectories. This has subsequently, after decades of debate among both orthopaedic researchers and biomechanical engineers, been proved inaccurate [26]. When one talks about Wolff's law today, the implicit understanding is that bone adapts to loading conditions. How exactly this happens is the subject of a large body of research, both in the medical and mechanics fields.

According to Cowin [22] [24], there is an equilibrium state of loading under which a certain section of bone undergoes no remodelling at all. An example of such loading would be a daily walk to work. If a person walks 2 km to work every day, this corresponds to an equilibrium loading state. If the same person were to start running a marathon a day with a 50kg backpack then this loading would exceed the equilibrium distribution, and remodelling would occur in bones such as the femur. For example, it has been shown that the humerus of the playing arm of a Wimbledon tennis player has 30% larger cross-sectional area than the non-playing arm [26]. Another factor that can change the force field acting on a certain portion of bone is the introduction of an implant which causes a redistribution of loads in the bone.

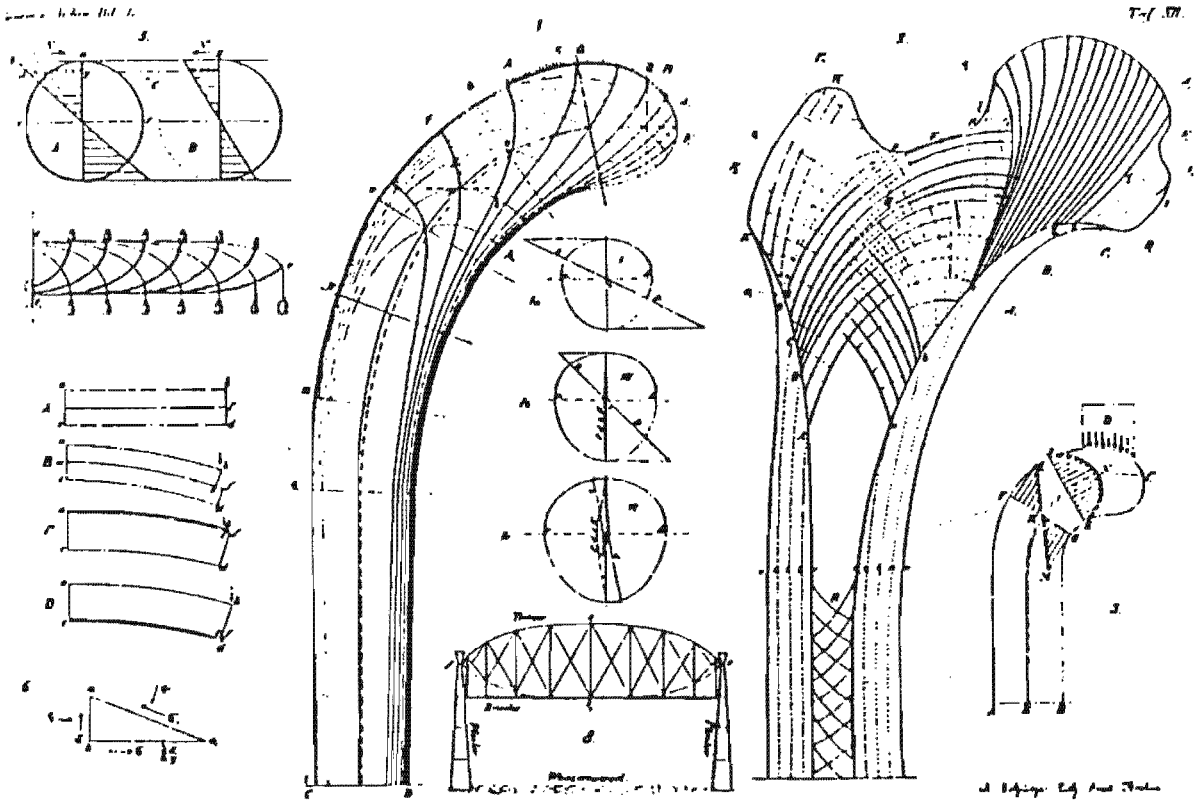

Figure 1.1: Stress Trajectories Calculated for Cullman's Crane and the Human Femoral Head.

1.3 Relevant Physiology

The physiology discussed below is that of bones that contain some volume of spongy bone, for instance long bones such as the femur or small bones such as the vertebrae. Bones such as the skull and the ribs, which contain little or no spongy bone, are not considered in this work. The bones of interest here consist of a large volume of cellular solid on the inside (*cancellous* bone) and a solid on the outside (*cortical* bone) (see Figure 1.2). However, both cancellous and cortical bone consist of the same bone matrix material; all solid bone matrix is made up of of calcified tissue and living cells called *osteocytes* that are found in tiny gaps in the bone matrix called *lacunae*. It is the amount of matrix material per unit volume (*apparent density*) and the manner in which the matrix is structured that make cancellous and cortical bone different.

Cancellous bone is anisotropic and is made up of *lamellae* in which the collagen fibres are oriented in parallel arrays. Lacunae are distributed evenly in these lamellar arrays and are interconnected by *canaliculae* and *Volkmann canals* through which nutrients for the osteocytes diffuse. Cortical bone is more organised in architecture as it needs to maintain a thickness sturdy enough for protection, yet it also needs to be able to absorb enough

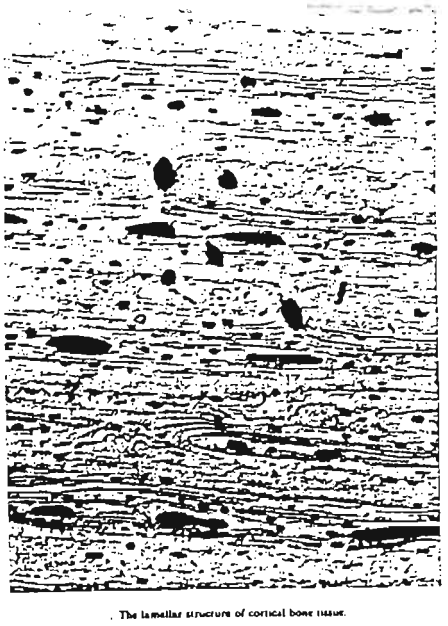

The lamellar structure of cortical bone tissue.

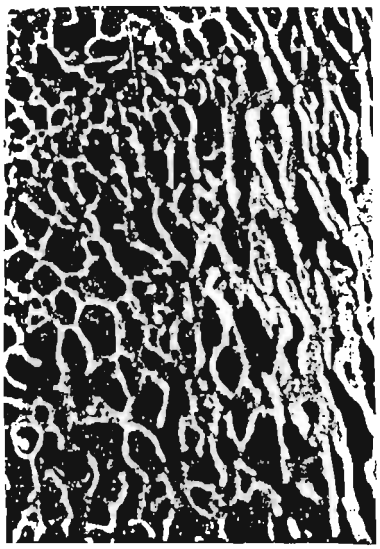

The porous structure of cancellous bone structure.

Figure 1.2: Some Pictures of Cortical and Cancellous Bone.

nutrients for the osteocytes to survive. The smallest structural element in cortical bone is the *osteon*, which is as strut consisting of bone fibres wrapped concentrically around a so-called *Haversian canal*. These osteons or *Haversian systems* take much longer to grow than lamellar bone, and are arranged longitudonally in the cortex, i.e. the hard shell, of long bones [4].

There are several different cells engaged in the process of growing bone, replacing and dissolving it (see Figure 1.3). When considering bone, one has to take into account that everything is changing all the time: cells regenerate constantly. The turnover time for healthy bone is of the order of 200 days [9]. Also, once the tissue calcifies there is more solid bone matrix than there are bone cells living in the matrix: mineral salts account for about 60% of bone volume in calcified bone matrix. The following is a summary of the different cells active in living bones, and what their functions are with regard to the calcified tissue.

osteogenic cells These can develop into *chondroblasts* or *osteoblasts*, and are found on the surface of bone matrix. They constitute the periosteum (top layer of cells on the bone surface) and form a single layer of cells that covers all surfaces within the bone cavity and line all vascular channels such as Volkmann canals and Haversian canals [4].

osteoblasts These are the cells that form bone matrix. They are found on the surface of already existing bone and continually lay down fresh bone matrix.

osteocytes As mentioned already, these cells live inside the calcified bone matrix in

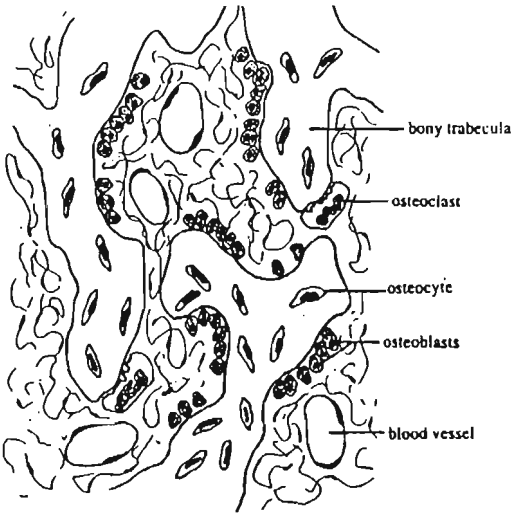

Figure 1.3: Several Different Cells Important in Bone Remodelling.

spaces called lacunae. It is believed that an osteocyte evolves out of an osteoblast once the osteoblast is completely surrounded by calcified tissue and can lay down no more. Osteocytes are interconnected by cytoplasmic processes which lie in the canaliculae, Volkmann canls and Haversian canals, and form a network of cells like the neurons in the brain. It is conjectured that they are strain sensors and are responsible for sending out remodelling signals [49] [35] [26]. There are more osteocytes in osteoporotic bone than in healthy bone [29].

osteoclasts These are multinuclear cells responsible for dissolving the calcified bone matrix. They are not evolved from osteogenic cells but rather from macrophages [9]. By dissolving the calcified tissue of the bone matrix, osteoclasts make minerals available to be carried away in the blood stream. It is not known how these cells cope with osteocytes when they impinge upon them [9] [79] [4].

These are only a few of the myriad living cells found in bone. Omitted here is the bone marrow, which fills the gaps between trabeculae and supplies the osteocytes and other cells attached to the bone matrix with enough nutrients to survive. The marrow forms a fluid inside the cellular solid of the spongy bone, which does not have a large effect on the mechanical properties of bone as a structure. Cowin et al. [17] have taken this fluid into account in some of the early models of bone, but since the marrow is not directly involved in the remodelling process, it will not be considered here. All the cells described above have a distinct function in the remodelling process.

All of the analyses performed in this study use the human hip joint as a domain (see Figure 1.4). Some medical terminology used for describing the geometry of the femur

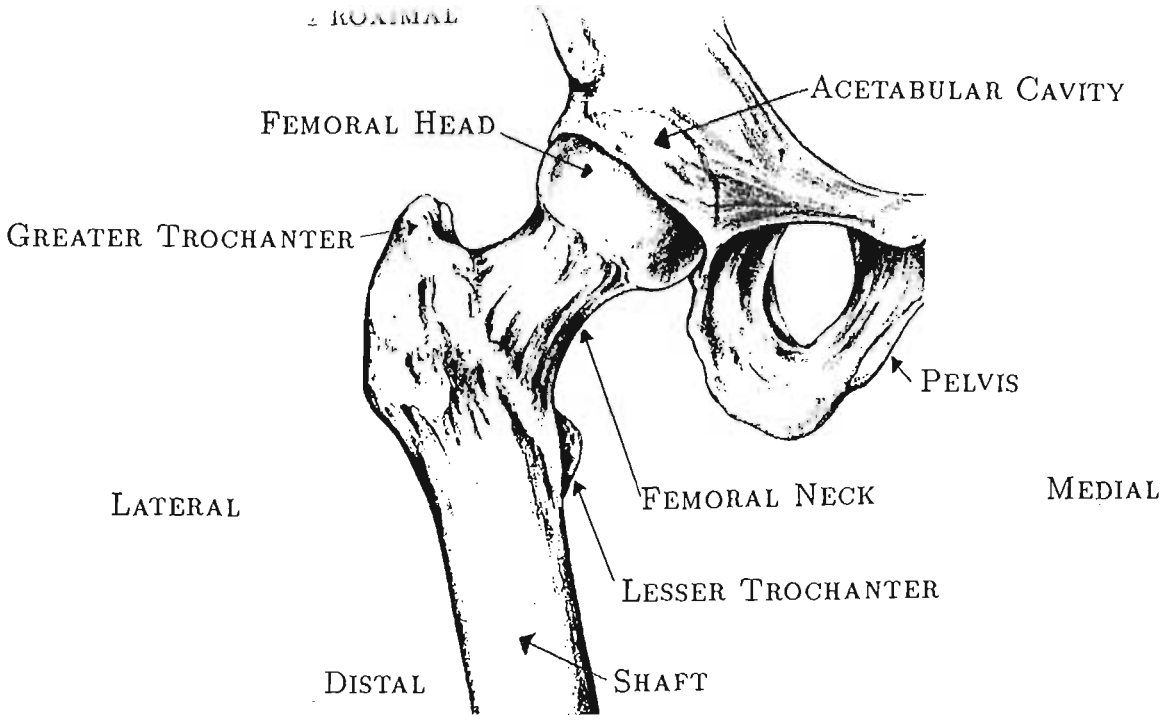

Figure 1.4: Anatomy of the human femur with some of the features that will be referred to later.

and the pelvic bone is given in the caption of Figure 1.4. The coordinate system outlined in Figure 1.4 will be used to describe locations on the bone geometry. There are four directons in the coordinate system of the femur, and they are described by the following terms: *distal* means in the vicinity of the joint, while *proximal* means away from the joint towards the knee. This is like a north-south coordinate. The terms *medial* and *lateral* refer to a position near the central vertical plane of the body and away from this plane respectively. This is like an east-west coordinate. There are also the coordinates of *frontal* (in front) and *sagittal* (at the back), but these will not be used in this study.

1.4 Remodelling Stimuli

When attempting to simulate the way in which bone responds to mechanical loads, it is important to consider the causes of bone remodelling. There are many possible triggers that could cause bone tissue to start the remodelling process. Examples are stress (σ), put forward by Pauwels [64], strain (ϵ), suggested by numerous authors including Turner [77], or strain energy (U), as proposed by Carter [12] and Huiskes [42]. Carter [11] and Currey [29] have also suggested that mechanical microdamage may act as a remodelling stimulus. Repeated loading of bone in everyday activities, or prolonged exercise, can lead to microscopic damage in the bone matrix, which may the stimulus which controls increase in bone mass. Research by Starkebaum [72] and Pollack [66] indicates that

electrical potentials generated by fluid flow in the bone canaliculae may be a stimulus for remodelling. This idea will be discussed further in Chapter 5. Clearly a scalar quantity such as the strain energy density is the most convenient to work with in a mathematical model, since this constitutes a single remodelling reference measure, as opposed to three for a vector remodelling stimulus or even more for a tensor remodelling stimulus. Huiskes [78] and Jacobs [47] have used a strain energy density based approach to set up finite element models of bones.

Experimental research [73] [51] indicates that strain is the actual remodelling criterion in nature. This could mean that, even though the bone is weaker in one direction than another, the same deformation threshold will always cause remodelling to set in. Lanyon et al [52] have found in experiments that dynamic loading can cause much more substantial remodelling than static loading of equivalent strain. With all these different results considered, it is quite clear that it is difficult to determine exactly what mechanical quantity is responsible for bone remodelling. Any mathematical model of the remodelling process will have to be as realistic as possible, while also being simple enough to use. In Chapter 4, a strain energy based remodelling algorithm as proposed by Carter and Jacobs [47] [12] will be discussed in detail. In Chapter 5 it will be argued that strain is a more appropriate variable to use as a remodelling stimulus, and a remodelling algorithm based on a scalar measure of strain will be presented.

1.5 Implant Design

How can the study of bone mechanics assist with the design of implants? The obvious problem of implants (see Figure 1.5 for an example of a hip joint replacement implant) is that these entail the introduction of a foreign material in close contact with living tissue. There is a mismatch of different properties, for instance elastic modulus (stiffness) and fracture toughness. An implant in the body is subject to corrosion, wear and fatigue loading. Huiskes et al. [41] [42] have investigated the mechanical effects that a prosthesis has on the surrounding bone. To simulate the remodelling process in the bone material, they have used a strain energy based remodelling criterion, in which remodelling occurs so as to satisfy

$$S - S_{ref} = 0$$

with S the average elastic energy per unit mass, and S_{ref} a reference average elastic energy per unit mass, ie. the amount of energy per unit mass that would induce no remodelling

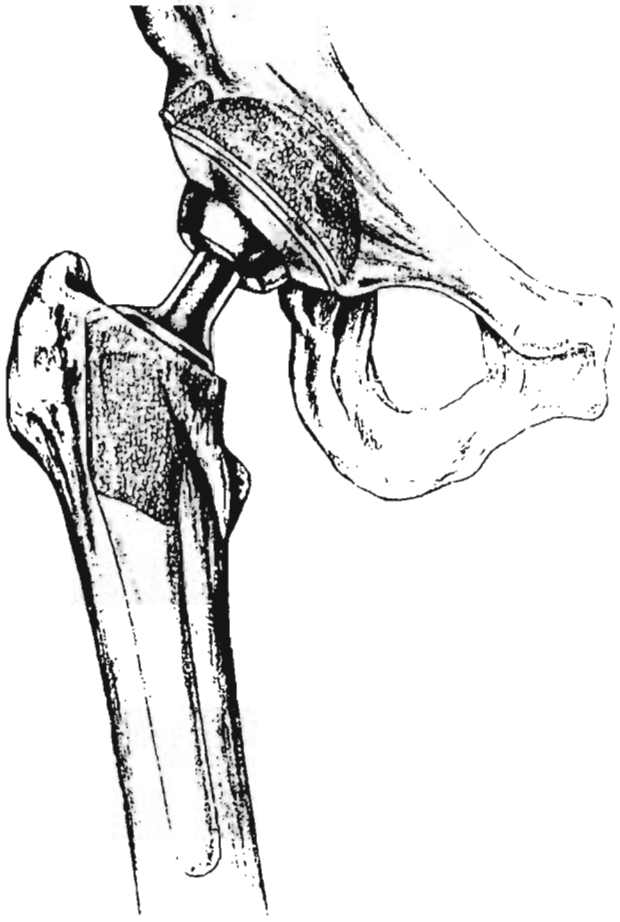

Figure 1.5: A Typical Femural Head Prosthesis.

reaction at all. A model similar to this will be described in Chapter 4.

Lanyon et al. [53] have found experimentally that a minimum effective strain signal is necessary to stimulate remodelling. This could be different in each individual, and account for differences observed in orthopaedic practice. Huiskes et al. [42] were able to show that once the prosthesis is in place, parts of the surrounding bone that normally experience stress are shielded by the harder prosthesis stem and therefore resorb with time. This stress shielding can be reduced by using a prosthesis with a more flexible stem, but greater flexibility will require a stronger interface bond between the implant and the bone. Another major design factor is the actual shape of the prosthesis: on testing four different prosthesis designs using a two-dimensional finite element mesh, Huiskes discovered that the stress patterns for each of the designs differed vastly [41] . Some solutions to this problem of stress shielding include the use of a layer of cement between bone and implant in order to make the stiffness gradient at the material interfaces smoother. The cement is pressed into the hollowed-out bone before the implant is inserted, and then hardens after the operation is complete. This provides a material of intermediate stiffness between the

bone and the prosthesis, and can alleviate some of the stress shielding. Problems with this approach include difficulties in obtaining an airbubble-free layer of cement. Also, the heat generated by the chemical reaction of the cement hardening can kill off bone stock surrounding the implant, which is not desirable in osteoporotic patients who might have very little bone stock left.

Another solution is the design of implants with special surface coatings to enable bone tissue to grow into [62]. These coatings can consist of tiny cobalt-chromium beads sintered onto the implant surface, titanium plasma sprayed on the surface, or titanium fibres compacted randomly on the surface. Porous surface layers of differing porosity can be bonded to the implant in this manner [27]. A problem with this approach is that due to micromotion, the tissue growing into the porous layer does not calcify, but rather forms a layer of fibrous tissue growing deep into the implant surface, which means that the implant is very loose and yet almost impossible to remove.

Huiskes's finite element models have helped to explain why prostheses tend to work loose with time, and why bone stock is lost [42] [44]. Increased knowledge of bone remodelling can only improve on these insights. In Chapter 4 a model for cancellous bone similar to that of Huiskes will be discussed and an attempt will be made to bring it in line with recent experimental findings. Before this can be attempted, an introduction to the relevant mathematical and mechanical framework needs to be provided. This is the purpose of Chapters 2 and 3.

Chapter 2

Continuum Mechanics and Bone Structure Evolution

This chapter introduces the basic mechanics needed to model the real-life phenomenon of bone remodelling. The concept of approximating the highly discontinuous structure of trabecular bone as a continuous medium with certain mechanical properties will be discussed. The model takes the form of a system of partial differential equations, and their approximate solution by the finite element method will be explained in Chapter 3.

The approach described here relies on the principles of continuum mechanics to put the mechanical behaviour of bone into a mathematical framework. References on continuum mechanics include Chadwick [14] and Lai, Rubin and Krempl [50]. Rather than looking at the statics or dynamics of single particles in space, the bone is assumed to be a continuous medium. This is an idealization since no real material forms a continuum on a sufficiently small scale: every material consists of molecules which are arranged in such a fashion that there is matter in some places and other places are void. It is, however, useful to assume a material to have properties which vary smoothly when one wants to determine large scale characteristics such as deformation or density. In bone mechanics the assumption of material continuity limits one to a scale that is of the order of a tenth of a millimeter, as below this size the material exhibits distinct discontinuities such as trabeculae. The trabeculae form a lattice structure of narrow rods and plates which are between 70 and 200 μm thick [22].

The main feature of continuum mechanics is that properties such as displacement or stress are assumed to vary smoothly over the continuum, and balance laws such as the balance

of mass or and of momentum are required to hold on arbitrary volumes of the continuum [14]. For example, the balance of mass equation of classical non-relativistic physics which states that no mass can be created or destroyed, reads

$$\frac{dm}{dt} = 0 \tag{2.1}$$

when only one particle of mass m or a system of particles which have a combined mass of m is considered. In continuum mechanics, the same balance law takes the form

$$\frac{d}{dt}\int_{R_t} \rho\, dV = 0 \tag{2.2}$$

where ρ is the density and R_t denotes an arbitrary volume of the continuum. The density ρ is assumed to vary smoothly over R_t. The smoothness assumption automatically makes it impossible to include any fine structure such as microscopic cracks or trabecular struts in the model, though these features need to be accounted for using equivalent macroscopic quantities.

2.1 Vectors and Tensors

Since continuum mechanics, and bone mechanics in particular, uses the language and techniques of tensor analysis, a number of results from vector and tensor analysis are reviewed and collected together in this section. More comprehensive treatments may be found in the texts by Lai, Rubin and Krempl [50] and Chadwick [14].

The vectors and tensors used in this study are defined relative to three-dimensional Euclidean space E. An origin is assumed to be chosen once and for all, and the position vector of any point relative to this origin is denoted by $\boldsymbol{x}$. Generally, vectors are denoted by lower case boldface letters.

The dot or scalar product of two vectors $\boldsymbol{a}$ and $\boldsymbol{b}$ is denoted by $\boldsymbol{a}\cdot\boldsymbol{b}$, and the vector cross product by $\boldsymbol{a}\times\boldsymbol{b}$. The magnitude or norm of a vector $\boldsymbol{a}$ is defined by

$$|\boldsymbol{a}| = \sqrt{\boldsymbol{a}\cdot\boldsymbol{a}}. \tag{2.3}$$

Two vectors $\boldsymbol{a}$ and $\boldsymbol{b}$ are said to be orthogonal if $\boldsymbol{a}\cdot\boldsymbol{b} = 0$.

Similar to the origin, an orthonormal basis $B = \{\boldsymbol{e}_i\}_{i=1}^3$ is chosen once and for all; thus, the members of the basis satisfy

$$\boldsymbol{e}_i\cdot\boldsymbol{e}_j = \delta_{ij} \tag{2.4}$$

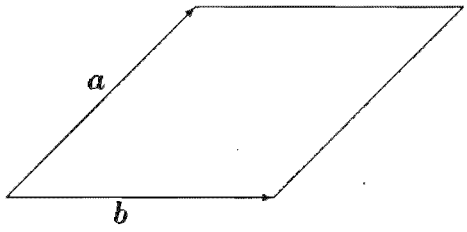

Figure 2.1: Parallellogram spanned by two vectors a and b.

where the Kronecker delta δ_{ij} takes the value 1 when $j = i$, and 0 otherwise. Here and henceforth all indices are assumed to run over $1, 2, 3$. We also make use of the Einstein summation convention, in terms of which summation over a repeated index is assumed. Thus any vector may be expressed in terms of the basis $\{e_i\}_{i=1}^3$ according to

$$\boldsymbol{a} = a_i \boldsymbol{e}_i \tag{2.5}$$

in which summation is implied on i; the numbers a_i are the components of $\boldsymbol{a}$ relative to this basis.

Another operator that works similarly to the Kronecker delta is the alternator ϵ_{ijk}, which is 1 when i, j, k form a cyclic permutation of 1,2, and 3, -1 when i, j, k is a non-cyclic permutation of 1,2, and 3, and 0 when either i, j or k are repeated. This operator is used to define the vector product of the basis vectors:

$$\boldsymbol{e}_i \times \boldsymbol{e}_j = \epsilon_{ijp} \boldsymbol{e}_p \tag{2.6}$$

Hence the vector product of two vectors $\boldsymbol{a}$ and $\boldsymbol{b}$ becomes

$$\boldsymbol{a} \times \boldsymbol{b} = (a_p \boldsymbol{e}_p) \times (b_q \boldsymbol{e}_q) = a_p b_q \boldsymbol{e}_p \times \boldsymbol{e}_q = \epsilon_{pqr} a_p b_q \boldsymbol{e}_r \tag{2.7}$$

It can be proved that the magnitude of this vector product equals the area of the parallellogram spanned by these two vectors (see Figure 2.1).

Second-order tensors, often referred to simply as tensors, are denoted by boldface letters (sometimes lower case Greek and other times upper case Roman), and may be regarded as linear maps from the space of vectors into itself. The action of a tensor $\boldsymbol{\sigma}$ on a vector $\boldsymbol{a}$ is denoted by $\boldsymbol{\sigma a}$, and is a vector $\boldsymbol{b}$, say:

$$\boldsymbol{\sigma a} = \boldsymbol{b}. \tag{2.8}$$

The identity tensor I is defined to be the tensor that leaves every vector unchanged, that is,

$$\boldsymbol{I}\boldsymbol{a} = \boldsymbol{a} \quad \text{for all vectors } \boldsymbol{a}. \tag{2.9}$$

The tensor product of two vectors $\boldsymbol{a}$ and $\boldsymbol{b}$ is a second-order tensor $\boldsymbol{a} \otimes \boldsymbol{b}$ defined by

$$(\boldsymbol{a} \otimes \boldsymbol{b})\boldsymbol{c} = (\boldsymbol{c} \cdot \boldsymbol{b})\boldsymbol{a} \quad \forall \boldsymbol{c} \in \mathrm{E} \tag{2.10}$$

In particular, the identity tensor can be written as

$$\boldsymbol{I} = \boldsymbol{e}_p \otimes \boldsymbol{e}_p \tag{2.11}$$

since

$$(\boldsymbol{e}_p \otimes \boldsymbol{e}_p)\boldsymbol{a} = (\boldsymbol{a} \cdot \boldsymbol{e}_p)\boldsymbol{e}_p = a_i(\boldsymbol{e}_i \cdot \boldsymbol{e}_p)\boldsymbol{e}_p = \boldsymbol{a}$$

The components of a tensor $\boldsymbol{\sigma}$ are defined by

$$\sigma_{ij} = \boldsymbol{e}_i \cdot (\boldsymbol{\sigma}\boldsymbol{e}_j), \tag{2.12}$$

so that $\boldsymbol{\sigma}$ can be written as

$$\boldsymbol{\sigma} = \sigma_{pq}\boldsymbol{e}_p \otimes \boldsymbol{e}_q. \tag{2.13}$$

The components of $\boldsymbol{\sigma}$ can be conveniently written as a 3×3 matrix:

$$\boldsymbol{\sigma} = \begin{pmatrix} \sigma_{11} & \sigma_{12} & \sigma_{13} \\ \sigma_{21} & \sigma_{22} & \sigma_{23} \\ \sigma_{31} & \sigma_{32} & \sigma_{33} \end{pmatrix} \tag{2.14}$$

The *trace* of a tensor is defined as

$$\mathrm{tr}\boldsymbol{\sigma} = \sigma_{ii} \tag{2.15}$$

The trace is invariant with respect to the basis B, ie. if the tensor is transformed into a coordinate system with a different basis, the trace of the tensor remains the same. The *deviatoric part* $\hat{\boldsymbol{\sigma}}$ of a tensor $\boldsymbol{\sigma}$ is defined as

$$\begin{aligned} \hat{\boldsymbol{\sigma}} &= \boldsymbol{\sigma} - \tfrac{1}{3}\mathrm{tr}(\boldsymbol{\sigma})\boldsymbol{I} \\ \text{or } \hat{\sigma}_{ij} &= \sigma_{ij} - \tfrac{1}{3}\sigma_{kk}\delta_{ij} \end{aligned} \tag{2.16}$$

Clearly the trace of a deviatoric tensor is zero, since

$$\mathrm{tr}\hat{\boldsymbol{\sigma}} = \hat{\sigma_{ii}} = \sigma_{ii} - \tfrac{1}{3}\sigma_{pp}\delta_{ii} = \sigma_{ii} - \sigma_{pp} = 0. \tag{2.17}$$

A tensor $\boldsymbol{\sigma}$ is said to be invertible if there exists a tensor $\boldsymbol{\tau}$ with the property that

$$\boldsymbol{\sigma\tau} = \boldsymbol{\tau\sigma} = \boldsymbol{I}. \tag{2.18}$$

If $\boldsymbol{\sigma}$ is invertible, then its inverse $\boldsymbol{\tau}$ is denoted by $\boldsymbol{\sigma}^{-1}$. The matrix of components of $\boldsymbol{\sigma}^{-1}$ is the inverse of the matrix of components of $\boldsymbol{\sigma}$.

The determinant $\det \boldsymbol{\sigma}$ of a tensor $\boldsymbol{\sigma}$ is defined to be the determinant of the matrix of components of $\boldsymbol{\sigma}$. Like the trace, this is a scalar invariant. In the case of a 2×2 matrix $\boldsymbol{A}$ given by

$$\boldsymbol{A} = \begin{pmatrix} a & b \\ c & d \end{pmatrix},$$

one has the useful result

$$\boldsymbol{A}^{-1} = \frac{1}{\det \boldsymbol{A}} \begin{pmatrix} d & -b \\ -c & a \end{pmatrix}. \tag{2.19}$$

The transpose $\boldsymbol{\sigma}^T$ of a tensor $\boldsymbol{\sigma}$ is the tensor defined by

$$\boldsymbol{b} \cdot \boldsymbol{\sigma}^T \boldsymbol{a} = \boldsymbol{a} \cdot \boldsymbol{\sigma b} \tag{2.20}$$

for all vectors $\boldsymbol{a}, \boldsymbol{b}$. The matrix of components of $\boldsymbol{\sigma}^T$ is the transpose of the matrix of components of $\boldsymbol{\sigma}$, that is,

$$\sigma^T_{ij} = \sigma_{ji}. \tag{2.21}$$

The tensor $\boldsymbol{\sigma}$ is symmetric if $\boldsymbol{\sigma}^T = \boldsymbol{\sigma}$, and skew-symmetric if $\boldsymbol{\sigma}^T = -\boldsymbol{\sigma}$. For the tensor composition $\boldsymbol{\sigma\tau}$,

$$(\boldsymbol{\sigma\tau})^T = \boldsymbol{\tau}^T \boldsymbol{\sigma}^T \tag{2.22}$$

holds, since

$$\begin{aligned} \boldsymbol{a} \cdot (\boldsymbol{\sigma\tau})^T \boldsymbol{b} &= \boldsymbol{b} \cdot \boldsymbol{\sigma\tau a} && (2.23) \\ &= \boldsymbol{b} \cdot \boldsymbol{\sigma}(\boldsymbol{\tau a}) && (2.24) \\ &= (\boldsymbol{\tau a}) \cdot \boldsymbol{\sigma}^T \boldsymbol{b} && (2.25) \\ &= \boldsymbol{\sigma}^T \boldsymbol{b} \cdot \boldsymbol{\tau a} && (2.26) \\ &= \boldsymbol{a} \cdot \boldsymbol{\tau}^T \boldsymbol{\sigma}^T \boldsymbol{b} && (2.27) \end{aligned}$$

using equation (2.20).

A tensor $\boldsymbol{\sigma}$ is said to be positive-definite if

$$\boldsymbol{a} \cdot \boldsymbol{\sigma a} > 0 \text{ for all vectors } \boldsymbol{a}, \tag{2.24}$$

and $\boldsymbol{a} \cdot \boldsymbol{\sigma a} = 0$ if and only if $\boldsymbol{a} = \boldsymbol{0}$.

A non-zero unit vector $\boldsymbol{v}$ is denoted as an eigenvector of $\boldsymbol{\sigma}$ if there exists a *real* number μ, the corresponding eigenvalue of $\boldsymbol{\sigma}$, such that

$$\boldsymbol{\sigma v} = \mu \boldsymbol{v}. \tag{2.25}$$

In the case of a symmetric tensor, three eigenvalues μ_1, μ_2 and μ_3 exist, and the corresponding set of eigenvectors $\boldsymbol{v}_1, \boldsymbol{v}_2, \boldsymbol{v}_3$ is orthonormal [14]. Any symmetric tensor $\boldsymbol{S}$ can thus be expressed as

$$\boldsymbol{S} = \boldsymbol{SI} = \boldsymbol{S}(\boldsymbol{v}_r \otimes \boldsymbol{v}_r) = (\boldsymbol{S}\boldsymbol{v}_r) \otimes \boldsymbol{v}_r = \sum_{r=1}^{3} \mu_r (\boldsymbol{v}_r \otimes \boldsymbol{v}_r); \tag{2.26}$$

this is called the *spectral representation* of $\boldsymbol{S}$. In matrix form,

$$\boldsymbol{S} = \begin{pmatrix} \mu_1 & 0 & 0 \\ 0 & \mu_2 & 0 \\ 0 & 0 & \mu_3 \end{pmatrix}; \tag{2.27}$$

with respect to the basis $\boldsymbol{v}_1, \boldsymbol{v}_2, \boldsymbol{v}_3$ [50]. The trace of this tensor is given by $\mathrm{tr}\boldsymbol{S} = \mu_1 + \mu_2 + \mu_3$. As stated earlier, the trace is a coordinate invariant quantity, hence the trace of any symmetric tensor is given by the sum of its eigenvalues.

A tensor that maps a second-order tensor to another second-order tensor is called a fourth-order tensor and has four indices. Given second-order tensors $\boldsymbol{\sigma}$, $\boldsymbol{\tau}$ and fourth-order tensor $\boldsymbol{C}$,

$$\begin{aligned} \boldsymbol{C\sigma} &= \boldsymbol{\tau} \\ \text{or } C_{ijkl}\sigma_{kl} &= \tau_{ij}. \end{aligned} \tag{2.28}$$

A fourth-order tensor C_{ijkl} has $3 \times 3 \times 3 \times 3 = 81$ components.

2.2 Tensor Analysis

In this study, the scalar, vector and tensor variables are typically functions of position and time. In addition to indicial and matrix notation for vectors and tensors, the derivative notation $f_{i,j} = \frac{\partial f_i}{\partial x_j}$ for spacial derivatives is employed throughout. Several vector

and tensor fields arise by taking spacial derivatives in different ways. These fields are summarised here. The *gradient of a scalar field* ϕ is the vector grad ϕ or $\nabla\phi$ defined by

$$\text{grad}\,\phi \;=\; \nabla\phi \;=\; \frac{\partial\phi}{\partial x_p}e_p. \tag{2.29}$$

The *gradient of a vector field* $\boldsymbol{u}$ is the second-order tensor grad $\boldsymbol{u}$ or $\nabla\boldsymbol{u}$ defined by

$$\text{grad}\,\boldsymbol{u} \;=\; \nabla\boldsymbol{u} \;=\; \frac{\partial u_p}{\partial x_q}\boldsymbol{e}_p \otimes \boldsymbol{e}_q. \tag{2.30}$$

The *divergence of a vector field* $\boldsymbol{u}$ is the scalar div $\boldsymbol{u}$ or $\nabla\cdot\boldsymbol{u}$ defined by

$$\text{div}\,\boldsymbol{u} \;=\; \nabla\cdot\boldsymbol{u} \;=\; \frac{\partial u_p}{\partial x_p}. \tag{2.31}$$

The *divergence of a tensor field* $\boldsymbol{\sigma}$ is the vector div $\boldsymbol{\sigma}$ or $\nabla\cdot\boldsymbol{\sigma}$ defined by

$$\text{div}\,\boldsymbol{\sigma} \;=\; \nabla\cdot\boldsymbol{\sigma} \;=\; \frac{\partial\sigma_{pq}}{\partial x_p}e_q. \tag{2.32}$$

Use will also be made of the Green-Gauss integral theorem, two versions of which are

$$\begin{aligned} \int_R \text{div}\,\boldsymbol{u}\,dV \;&=\; \int_{\partial R}\boldsymbol{u}\cdot\boldsymbol{n}\,dA \\ \text{and}\quad \int_R \text{div}\,\boldsymbol{\sigma}\,dV \;&=\; \int_{\partial R}\boldsymbol{\sigma}\boldsymbol{n}\,dA \end{aligned} \tag{2.33}$$

where $\boldsymbol{u}$ and $\boldsymbol{\sigma}$ are a vector field and a tensor field respectively, and R is a region with boundary ∂R; $\boldsymbol{n}$ is the outward unit vector normal to ∂R.

2.3 Basic Continuum Mechanics

The basic problem of continuum mechanics is the following: given a body which occupies a domain R_0 at a time $t = 0$, find the deformed shape of the body, as well as the internal forces in the body at time $t > t_0$, given a prescribed loading history. The deformed shape is described by the *displacement vector* $\boldsymbol{u}(\boldsymbol{x}, t)$ (see figure 2.2), while the state of local deformation is captured in the strain tensor ϵ, defined by

$$\epsilon = \tfrac{1}{2}(\nabla\mathrm{u} + \nabla^T\mathrm{u}) \quad \text{or} \quad \epsilon_{ij} = \tfrac{1}{2}(u_{i,j} + u_{j,i}) \tag{2.34}$$

Because the displacement gradients in bone mechanics are small, that is, $|u_{i,j} \ll 1|$, it is acceptable to use the linear or infinitesimal strain tensor (2.34) rather than its nonlinear

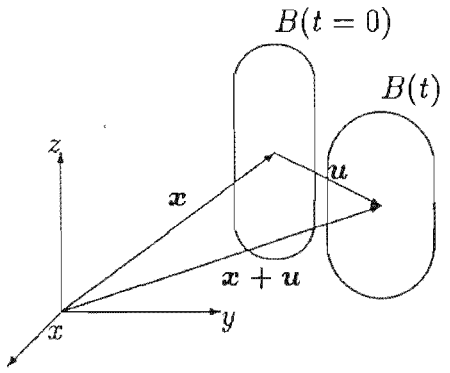

Figure 2.2: Undeformed and deformed shapes in a typical continuum mechanics problem; a point originally at position $\boldsymbol{x}$ moves to position $\boldsymbol{x}+\boldsymbol{u}$ after time t. The deformations are exaggerated.

finite strain counterpart. In bone mechanics one deals with small strains, and all the models presented in this work will assume linear elastic, small strain behaviour of the cancellous bone.

Internal forces are measured with the aid of the *stress tensor* $\boldsymbol{\sigma}$ which, like the strain tensor ϵ, is symmetric as a consequence of the principle of angular momentum. The traction $\boldsymbol{t}$ on any plane with unit normal $\boldsymbol{n}$ can be computed using the stress tensor:

$$\boldsymbol{t} = \boldsymbol{\sigma}\boldsymbol{n} \tag{2.35}$$

As the number of load cycles that a bone such as the femur is subjected to is very large and a dynamic loading analysis would involve huge computational effort, all loads in this work are applied in a quasistatic manner. That means that inertial forces due to acceleration can be neglected. The principle of balance of momentum leads to a set of equations known as *Cauchy's equations of motion* [50]. For the quasistatic case they reduce to the equations of equilibrium

$$\operatorname{div}\boldsymbol{\sigma} + \boldsymbol{f} = \boldsymbol{0} \quad \text{or} \quad \sigma_{ij,j} + f_i = 0; \tag{2.36}$$

the vector $\boldsymbol{f}$ denotes the body force, ie. the sum of all external forces except the boundary conditions, exerted on the body.

Equations (2.36), together with the displacement-strain equations (equation (2.34)), give nine equations in fifteen unknowns. These equations are independent of the properties of

the material. In order to make this set of equations solvable, a further set of 6 equations linking $\boldsymbol{\sigma}$ and $\boldsymbol{\epsilon}$ are required. These are called the *constitutive equations*, and they capture the features of a particular material model. In this study, isotropic linear elastic material behaviour is assumed. In a linear elastic solid[1] , $\boldsymbol{\sigma}$ and $\boldsymbol{\epsilon}$ are related to each other linearly, in the form

$$\boldsymbol{\sigma} = C\boldsymbol{\epsilon} \quad \text{or} \quad \sigma_{ij} = C_{ijkl}\epsilon_{kl}, \tag{2.37}$$

where C is the fourth-order elasticity tensor. For isotropic materials the components of C depend only on two independent constants, which are called the *Lamé* constants and are defined as follows:

$$\lambda = \frac{\nu E}{(1+\nu)(1-2\nu)} \tag{2.38}$$

$$\mu = \frac{E}{2(1+\nu)} \tag{2.39}$$

Here, E and ν are the Young's modulus and Poisson's ratio respectively and can be determined from experiment.

In terms of the Lamé constants, the stress-strain relation for a linear elastic material is

$$\sigma_{11} = \lambda \mathrm{tr}\epsilon + 2\mu\epsilon_{11} \tag{2.40}$$

$$\sigma_{22} = \lambda \mathrm{tr}\epsilon + 2\mu\epsilon_{22} \tag{2.41}$$

$$\sigma_{33} = \lambda \mathrm{tr}\epsilon + 2\mu\epsilon_{33} \tag{2.42}$$

$$\sigma_{12} = 2\mu\epsilon_{12} \tag{2.43}$$

$$\sigma_{13} = 2\mu\epsilon_{13} \tag{2.44}$$

$$\sigma_{23} = 2\mu\epsilon_{23} \tag{2.45}$$

However, the two material constants E and ν are not constant in time but depend on a set of internal variables which evolve with time, and which depend on the apparent density. This is the subject of the following Section.

[1]Most bone material in the skeleton is very brittle, but this depends on the kind of loads it is subjected to. The bone in deer's antler is quite ductile for example, as it needs to absorb large amounts of impact energy [28]. The bone in a narwhal's auditory complex, the bulla, on the other hand, is extremely stiff and also very brittle as it needs to transmit sound waves. The cancellous bone in the human femur is somewhere in between as it needs to be both stiff and impact-absorbing. It is reasonable to say that during regular usage, this bone undergoes only small deformations and therefore behaves as a linear elastic, non-ductile solid.

2.4 Constitutive Equations for Bone

2.4.1 Density remodelling

The simplest model of bone remodelling is one that takes into account only changes in the specific density. The bone changes its porosity, mineral content, X-ray opacity and weight. If V is the total volume of a bone specimen and m_s the mass of all the solid contained in this specimen (i.e. the cell walls), then the specific density ρ^* is defined by

$$\rho^* = \frac{m_s}{V}. \tag{2.46}$$

A solid with volume fraction V_s/V less than 0.3 is considered to be a cellular solid [2]. This is the case for most cancellous bone, but not for cortical bone. However, in this study, bone of any density is assumed to have the ability to remodel. The constitutive equations for a material with density remodelling consist of the linear elastic law (2.37), in which $\boldsymbol{C}$ depends on a remodelling variable e, together with an evolution equation for e. This pair of equations takes the form

$$\boldsymbol{\sigma} = (\xi_0 + \mathrm{e})\boldsymbol{C}(\mathrm{e})\boldsymbol{\epsilon}, \tag{2.47}$$

$$\dot{\mathrm{e}} = A(\mathrm{e}) + \boldsymbol{A}(\mathrm{e})\cdot\boldsymbol{\epsilon}, \tag{2.48}$$

where ξ_0 denotes an initial volume fraction and e is the change in volume fraction as time progresses. The scalar function $A(\mathrm{e})$ and the second-order tensor function $\boldsymbol{A}(\mathrm{e})$ have to be determined using physiological parameters or biological insight into the remodelling process. Together with Cauchy's equations and the strain-displacement relations this represents 16 equations in the 16 unknowns σ_{ij}, ϵ_{ij}, u_i, e. Cowin et al. [18] have solved these equations analytically for the specific case of a medullary pin inserted into cancellous bone, taking $A(\mathrm{e})$ as a quadratic scalar function and $A_{ij}(\mathrm{e})$ as a linear tensor function. Note that remodelling depends explicitly on the strain $\boldsymbol{\epsilon}$, and hence this is a strain-driven model.

2.4.2 Periosteal and endosteal surface remodelling

In a different model of cancellous bone, Cowin et al.[19] examine free surface remodelling. Here, the bone changes its actual shape both at the periosteal and endosteal surfaces, the periosteal surface being the outside surface of the bone and the endosteal surface the inside surface of a hollow bone shaft (see Figure 2.3). Instead of a density evolution

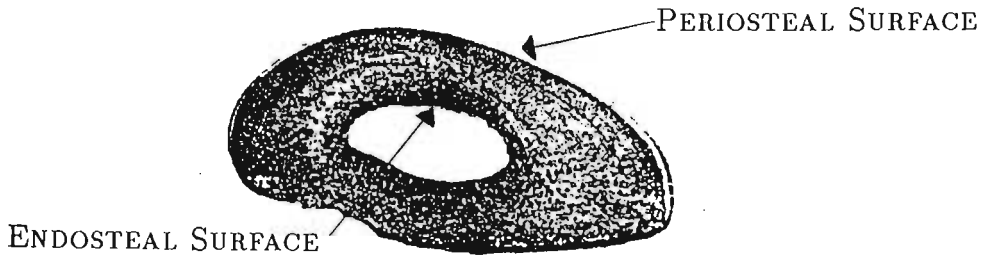

Figure 2.3: Cross-section of a long bone shaft with the periosteal and endosteal surfaces labelled.

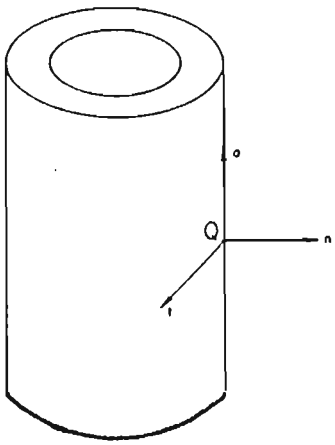

Figure 2.4: Surface Remodelling on a Cylinder.

equation such as equation (2.48), a surface evolution equation is given by

$$v = G_{ij}(\boldsymbol{n})[\epsilon_{ij} - \epsilon^0_{ij}] \tag{2.49}$$

where u is the surface speed in a direction normal to the remodelling surface, ϵ^0_{ij} is the remodelling equilibrium strain (see Figure 2.4), and G_{ij} are the components of a constant second-order tensor. One can rewrite this in terms of the stress σ_{ij} in the form

$$v = H_{ij}(\boldsymbol{n})[\sigma_{ij} - \sigma^0_{ij}], \tag{2.50}$$

where σ^0_{ij} and H_{ij} are defined in a similar manner as ϵ^0_{ij} and G_{ij}. Cowin et al. [20] have carried out uniaxial stress experiments where the coefficients G_{ij} can be chosen in such a way that the numerical calculations give the same results as the actual animal studies. The animal studies consisted of rendering limbs in certain animals (beagles, pigs) inactive, or overstimulating them by applying cyclic loads and monitoring the deposition or resorption of bone tissue on the endosteal and periosteal surface in certain cross-sections. Ulnar

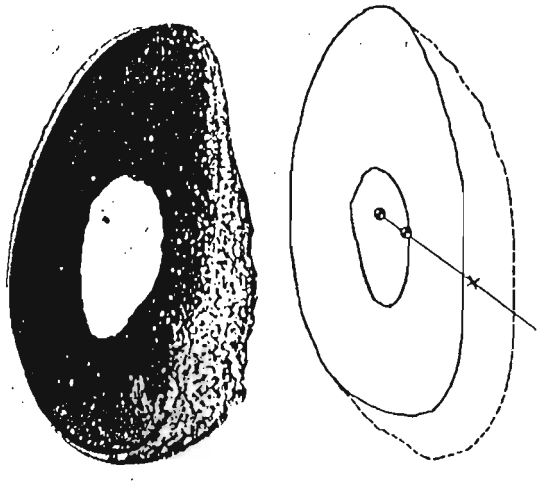

Figure 2.5: Comparing experimentally induced surface remodelling in animals with the theory. Taken from Cowin.

osteotomy experiments of sheep by Lanyon et al. [51] that will be discussed in Chapter 5 were also used by Cowin et al. to determine these coefficients [20] (see Figure 2.5).

No method of calculating these coefficients theoretically has been found to date, and this is a major shortcoming of both the internal and surface remodelling models: there is a large number of parameters involved which are not easily deduced from theoretical considerations. Cowin has been able to show, using this model, that a medullary pin fitted tightly into a cylindrical cancellous bone shell (such as a femoral prosthesis stem into the femural shaft) will eventually work loose as a result of the surface remodelling taht takes place.

2.4.3 Fabric-material relationships

As was pointed out, the models described above do not take into account trabecular orientation. This can, however, be included in a continuum model by incorporating as a variable the general orientation of trabeculae. While density represents a first order (scalar) characterisation of the cancellous bone material, density and trabecular orientation together give a second order characterisation which is tensorial in nature, as explained below.

The fabric orientation is quantified by using a mean intercept length matrix. Trabeculae in cancellous bone form sets of regionally parallel fibres. The architecture of these fibres can be measured by drawing a line at an angle θ to the horizontal and by measuring the average distance between fibres along this line (see Figure 2.6). This is the mean intercept

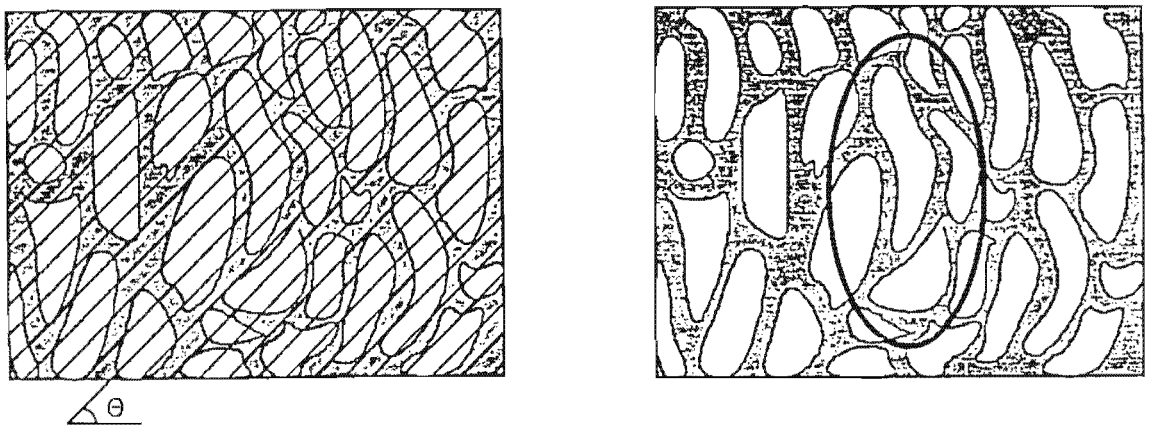

Figure 2.6: Measuring the Mean intercept Length in a sample of cancellous bone: test lines as well as the mean intercept length ellipse superimposed on the cancellous bone tissue structure it represents. Taken from Cowin.

length L, which can be represented as a function of angle by the expression [22]

$$\frac{1}{L^2(\theta)} = M_{11}\cos^2\theta + M_{22}\sin^2\theta + 2M_{12}\sin\theta\cos\theta \tag{2.51}$$

Taking three such measurements for different values of θ, one can determine the components of $\boldsymbol{M}$ and plot the ellipse given by (2.51). Harrigan and Mann [38] showed that, in three dimensions, this can be generalised to

$$\frac{1}{L^2(\boldsymbol{n})} = \boldsymbol{n}\cdot\boldsymbol{M}\boldsymbol{n} \tag{2.52}$$

where L is the mean intercept length along a unit normal vector $\boldsymbol{n}$. Hence in three dimensions, all the components of the positve definite second-order tensor $\boldsymbol{M}$ can be determined by measuring the mean intercept length L along various unit normal vectors. Equation (2.52) is the equation of an ellipsoid in three dimensions which presents an appropriate visualisation of the anisotropy of the material [22]. If the ellipsoid is a sphere, then the material has no preferred orientation and is therefore isotropic, even though on a local level there is a high degree of anisotropy. If the fabric ellipsoid is not spherical the material is anisotropic, and the ratios of the major and minor axes of the fabric ellipsoid are a measure of the directions of trabecular orientation.

Cowin [22] has incorporated the idea of fabric orientation in the constitutive equations by introducing the fabric tensor $\boldsymbol{A}$, which is defined by

$$\boldsymbol{A} = \boldsymbol{M}^{-1/2}$$

The square root of $\boldsymbol{M}$ is well-defined as $\boldsymbol{M}$ is a positive definite tensor (see equation (2.52)) because $L^2 > 0$ always. Trabecular orientation is characterised by the eigenvectors (direction of material orientation) and eigenvalues (magnitude of anisotropy) of $\boldsymbol{M}$. The

problem with this model is the relation between the fabric tensor and the elasticity tensor. Cowin [21] has shown that if one assumes that the anisotropy of the cancellous bone is due only to the trabecular structure, i.e. the bone matrix material is isotropic, the relationship of the elasticity tensor and the fabric tensor is given by

$$\begin{aligned} C_{ijkl} &= a_1\delta_{ij}\delta_{kl} + a_2(A_{ij}\delta_{kl} + \delta_{ij}A_{kl}) + \\ &\quad a_3(A_{kq}A_{ql}\delta_{ij} + \delta_{kl}A_{iq}A_{qj}) + \\ &\quad b_1A_{ij}A_{kl} + \\ &\quad b_2(A_{kq}A_{ql}A_{ij} + A_{kl}A_{iq}A_{qj}) + \\ &\quad b_3A_{is}A_{sj}A_{kq}A_{ql} + \\ &\quad c_1(\delta_{ik}\delta_{jl} + \delta_{il}\delta_{jk}) + \\ &\quad c_2(A_{ik}\delta_{lj} + \delta_{il}A_{kj} + A_{il}\delta_{jk} + \delta_{ik}A_{lj} + \\ &\quad c_3(A_{ir}A_{rk}\delta_{lj} + \delta_{li}A_{kr}A_{rj} + \\ &\quad A_{ir}A_{rl}\delta_{kj} + \delta_{ik}A_{lr}A_{rj}) \end{aligned} \tag{2.53}$$

where a_i, b_i, c_i are all functions of the apparent density ρ^*, $\mathrm{tr}\boldsymbol{A}$, $\mathrm{tr}\boldsymbol{A}^2$, and $\mathrm{tr}\boldsymbol{A}^3$. Equation (2.53) is stated without proof as this would take up too much space here. One can theoretically evaluate all components of $\boldsymbol{C}$ using this expression, and it can be shown that if two eigenvalues of $\boldsymbol{M}$ are coincident, then the symmetry reduces to transversely isotropic symmetry, while if all eigenvalues of $\boldsymbol{M}$ are equal, the material exhibits isotropic symmetry [22]. The practical problem in applying this model lies in evaluating the parameters a_i, b_i, c_i. Cowin et al. [25] have done this in a strain based evolutionary bone remodelling algorithm with encouraging results; some of these results will be discussed below.

In order to include the fabric characterization discussed above, Cowin et al. introduce the deviatoric part of the fabric tensor $\boldsymbol{M}$ into the constitutive equations, as this is a measure of the *relative* fabric orientation, and assume that the elastic modulus depends only on the relative fabric orientation. This deviator is denoted by $\boldsymbol{K}$ and is defined as in equation (2.16). The tensor $\boldsymbol{K}$ has only five independent components as it is both symmetric and traceless, ie. $K_{ij} = K_{ji}$ and $K_{ii} = 0$. The constitutive relations are given by

$$\begin{aligned} \boldsymbol{\sigma} &= \boldsymbol{C}(\boldsymbol{K}, \mathrm{e})\boldsymbol{\epsilon}, \\ \dot{\boldsymbol{K}} &= \dot{\boldsymbol{K}}(\boldsymbol{K}, \boldsymbol{\epsilon}, \mathrm{e}), \\ \dot{\mathrm{e}} &= \dot{\mathrm{e}}(\boldsymbol{K}, \boldsymbol{\epsilon}, \mathrm{e}), \end{aligned}$$

where e is the change in volume fraction as defined above. The variables $\boldsymbol{K}$ and e are fixed at remodelling equilibrium but vary during the remodelling process. Cowin next

introduces the assumption that e depends only on the normal strain and $\boldsymbol{K}$ only on the deviatoric strain, so that the change in density and the change in fabric orientation are decoupled. This is not an assumption that is justified from a physiological point of view, but it makes calculations easier since the constitutive relations reduce to

$$\boldsymbol{\sigma} = \boldsymbol{C}(\boldsymbol{K}, \mathrm{e})\boldsymbol{\epsilon}, \tag{2.54}$$

$$\dot{\boldsymbol{K}} = \dot{\boldsymbol{K}}(\boldsymbol{K}, \hat{\boldsymbol{\epsilon}}), \tag{2.55}$$

$$\dot{\mathrm{e}} = \dot{\mathrm{e}}(\mathrm{tr}\boldsymbol{\epsilon}, \mathrm{e}), \tag{2.56}$$

One can express $\dot{\boldsymbol{K}}$ and $\dot{\mathrm{e}}$ explicitly as matrix polynomials. The linear approximations of equations (2.56), which include the small strain assumption (2.34), as well as restricting all terms to be proportional to $\boldsymbol{\epsilon}$, e, e^2, $\boldsymbol{K}$ and $\boldsymbol{K}^2$ and discarding all higher order terms [25], are then given by

$$\begin{aligned}\boldsymbol{\sigma} &= (g_1 + g_2\mathrm{e})(\mathrm{tr}\boldsymbol{\epsilon})\boldsymbol{I} + (g_3 + g_4\mathrm{e})\boldsymbol{\epsilon} + g_5(\boldsymbol{K}\boldsymbol{\epsilon} + \boldsymbol{\epsilon}\boldsymbol{K}) + \\ &\quad g_6(\boldsymbol{I}\mathrm{tr}(\boldsymbol{K}\boldsymbol{\epsilon}) + \mathrm{tr}(\boldsymbol{\epsilon})\boldsymbol{K}) \qquad (2.57)\\ \dot{\boldsymbol{K}} &= (h_1 + h_3\mathrm{e})(\hat{\boldsymbol{\epsilon}} - \hat{\boldsymbol{\epsilon}^0}) + \\ &\quad h_2[\boldsymbol{I}(\mathrm{tr}\boldsymbol{K}(\boldsymbol{\epsilon}) - \boldsymbol{\epsilon}^0)) - \tfrac{3}{2}(\boldsymbol{K}(\boldsymbol{\epsilon}) - \boldsymbol{\epsilon}^0) + (\boldsymbol{\epsilon} - \boldsymbol{\epsilon}^0)\boldsymbol{K}] + \\ &\quad h_4(\mathrm{tr}\boldsymbol{\epsilon} - \mathrm{tr}\boldsymbol{\epsilon}^0)\boldsymbol{K} \qquad (2.58)\\ \dot{\mathrm{e}} &= (f_1 + f_2\mathrm{e})(\mathrm{tr}\boldsymbol{\epsilon} - \mathrm{tr}\boldsymbol{\epsilon}^0) + f_3(\mathrm{tr}\boldsymbol{K}(\boldsymbol{\epsilon} - \boldsymbol{\epsilon}^0)) \qquad (2.59)\end{aligned}$$

where g_i, h_i, f_i are constants and $\hat{\boldsymbol{\epsilon}}$ is the deviatoric part of $\boldsymbol{\epsilon}$ as defined in equation (2.16). The reference strain tensor $\boldsymbol{\epsilon}^0$ is the strain under which no remodelling takes place, i.e. the remodelling equilibrium strain. These equations demonstrate the complexity of adding a fabric evolution equation to the density remodelling law described in [18]. An application of this theory is shown in Figure 2.7 using a stress field that rotates as time progresses. Principal coordinate axes of strain and fabric "follow" those of the stress state.

The disadvantage of this theory is that a large number of parameters (g_i, h_i, f_i) have to be found either experimentally or approximated using biological insight. Cowin admits that he "does not have this biological insight"[25]. Also, this theory can only be applied away from boundaries. To simulate remodelling near bone-implant interfaces, a modified theory of surface remodelling will have to be combined with the fabric evolution theory [25].

According to Huiskes [45], the parameters mentioned above can be evaluated purely by using a full-scale finite element model on a trabecular level of a cubic specimen of trabecular bone. Van Rietbergen et al. [75] have found a method, using a video imaging technique,

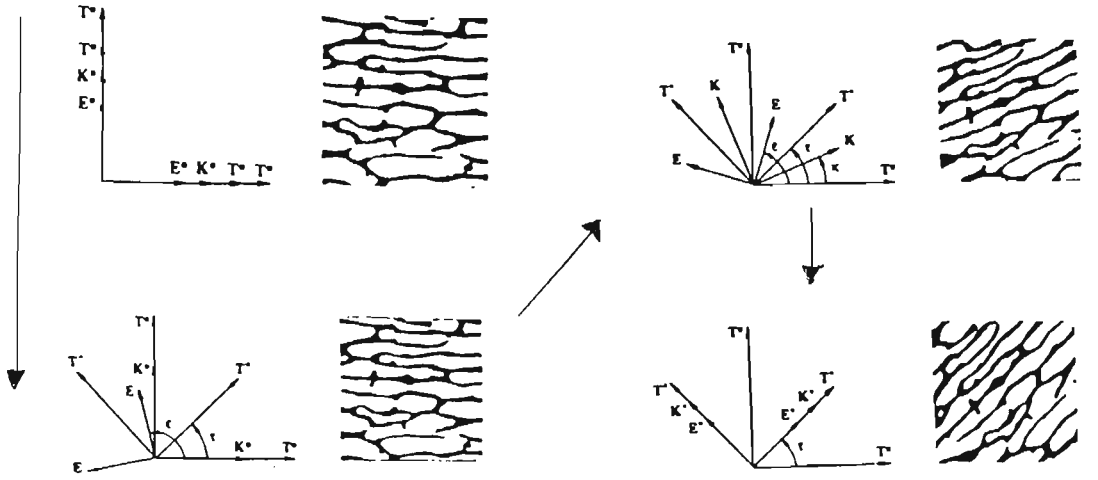

Figure 2.7: Anisotropic remodelling in a sample of cancellous bone; this sequence shows the evolution of the trabecular architecture from a remodelling equilibrium characterised by stress, strain and fabric denoted as T^0, E^0 and K^0 respectively to a remodelling equilibrium characterised by T^*, E^* and K^* respectively. Taken from Cowin.

to triangularize a cubic specimen of trabecular bone into isotropic linear elastic finite elements which are much smaller than the trabecular struts. They performed a stress analysis of the actual trabecular structures in a cubic piece of cancellous bone. This technique is non-destructive, and one can conduct mechanical experiments as well as numerical finite element simulations using the same geometry of trabecular bone [76]. As the trabecular bone is very complex in structure, the scale of the finite elements is very small. Van Rietbergen et al. have used almost 300 000 finite elements to reconstruct a $10mm$ cubic specimen [75]. It will become clear why this is problematic later on when the finite element method is described in detail. Using special solving routines, they have simulated compressive load cases on all faces of the cubic specimen and, using the finite element method, have found mechanical properties such as Young's moduli and Poisson's ratios in all three perpendicular directions. By scrutinising the geometry of the specimen, they could calculate the constants linking fabric and mechanical properties, and also make observations about how boundary conditions such as friction on the compression piston interface affect measurements of mechanical parameters [45]. As mentioned before, these boundary effects can cause experimental complications, particularly in compression tests, as they distort the apparent properties measured [76]. Unfortunately, the computer power available at the present time is not sufficient to run such an analysis on a full-scale model of a whole bone.

Chapter 3

The Finite Element Method

The finite element method is a technique for the numerical solution of partial differential equations. The method entails triangulation (subdivision) of the domain of the equations into several subdomains (finite elements), and approximation of the solution on each subdomain by continuous functions such as polynomials. The global solution is then the superposition of the solution on each subdomain. The finite element method is extensively applied in engineering to solve a wide range of complex problems in both solid and fluid mechanics (see Figure 3.1 for an example of a simple beam subdivided into finite elements). In bone mechanics the method has been in use for more than two decades [40]. Computational analysis using the finite element method is equivalent to conducting numerical experiments: the results of these experiments can be compared with results of *in vivo* experiments, and the parameters or the remodelling algorithm used in the numerical experiment can be adjusted appropriately [20]. Finite element analysis is particularly

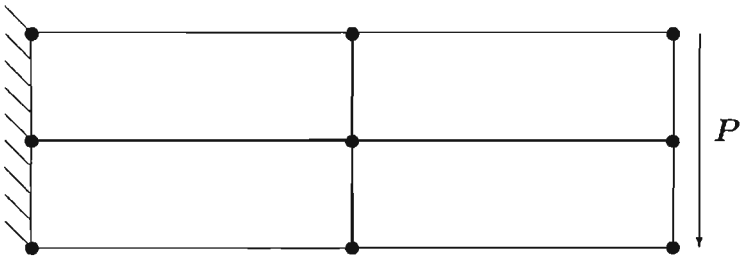

Figure 3.1: Cantilever beam with a bending load partitioned into four-noded quadrilateral finite elements. Its state at any point in time can be described by the displacement of each node (u,v) as well as the stress field on each element.

useful in implant design, as various geometries can be tested numerically without the risk of pathological failure.

References on the finite element method which may be consulted for further information include Cook [16] and Burnett [10]. There are many other books on the subject.

3.1 The Variational Problem

The equations that have to be solved are the linearised displacement-strain relations (2.34) and the equations of equilibrium (2.36), supplemented by the set of constitutive equations (2.37) and a set of boundary conditions, here assumed to be prescribed displacements $\boldsymbol{u}_0$ on a part ∂R_1 of the boundary, and prescribed tractions $\boldsymbol{t}_0$ on the remaining boundary ∂R_2. As mentioned in Section 2.4.1, the elasticity tensor $\boldsymbol{C}$ in equation (2.37) may depend on some internal variables which evolve in time, but at each iteration the equations nevertheless take the form of small strain linear elastic constitutive equations. The displacement $\boldsymbol{u}$ and the stress $\boldsymbol{\sigma}$ must satisfy the given boundary conditions, i.e. loads or movement constraints. Before this problem can be solved on a specific domain R using the finite element method, it has to be reformulated in a *variational form.*

In order to formulate the problem correctly, some appropriate function spaces must be defined [57]. The first of these is the space $L_2(R)$ of square-integrable functions, that is

$$L_2(R) = \left\{ v : \int_R v^2 \, dV < \infty \right\}. \tag{3.1}$$

Using this space, one can define the Sobolev space H^1 according to

$$H^1(R) = \left\{ v : v \in L_2(R), \ \frac{\partial v}{\partial x_i} \in L_2(R), \ i = 1,2,3 \right\}. \tag{3.2}$$

Both L_2 and H^1 are inner product spaces with inner products $(.,.)$ and norms $||.||$ defined by

$$(u,v)_{L_2} = \int_R uv \, dV, \tag{3.3}$$

$$||v||_{L_2} = \sqrt{(v,v)_{L_2}}, \tag{3.4}$$

for L_2 and

$$(u,v)_{H^1} = \int_V (uv + \nabla u \cdot \nabla v) \, dV, \tag{3.5}$$

$$||v||_{H^1} = \sqrt{(v,v)_{H^1}}, \tag{3.6}$$

for H^1. More details about Sobolev spaces can be found in Marti [58].

In order to solve this problem one chooses a space of admissible functions $\boldsymbol{u}$ and test functions $\boldsymbol{v}$ from the respective Sobolev spaces

$$V := \left\{\boldsymbol{v} : v_i \in H^1(R),\ v_i|_{\partial R_1} = 0\right\} \tag{3.7}$$

$$U := \left\{\boldsymbol{u} : u_i \in H^1(R),\ u_i|_{\partial R_1} = (u_0)_i\right\}. \tag{3.8}$$

In this study, the only displacement boundary conditions used are $u_i = 0$ on R_1, hence V and U are the same space and will subsequently be referred to as V.

Multiplying both sides the equation of equilibrium (2.40) by $\boldsymbol{v} \in V$ and integrating, one has

$$\int_R \boldsymbol{v}\cdot\operatorname{div}\boldsymbol{\sigma}\, dV + \int_R \boldsymbol{v}\cdot\boldsymbol{f}\, dV = 0. \tag{3.9}$$

Note that

$$\operatorname{div}(\boldsymbol{\sigma v}) = \boldsymbol{\sigma}\cdot\nabla\boldsymbol{v} + \boldsymbol{v}\cdot\operatorname{div}\boldsymbol{\sigma}; \tag{3.10}$$

this is an identity that is reminiscent of the product rule of differentiation in one dimension, and can be proved using partial derivatives. Substitution in (3.9)

$$\int_R \operatorname{div}(\boldsymbol{\sigma v})\, dV - \int_R \boldsymbol{\sigma}\cdot\nabla\boldsymbol{v}\, dV = -\int_R \boldsymbol{v}\cdot\boldsymbol{f}\, dV. \tag{3.11}$$

With the aid of the divergence theorem (2.37), the first term reduces to

$$\int_R \operatorname{div}(\boldsymbol{\sigma v})\, dV = \oint_{\partial R} (\boldsymbol{\sigma v})\cdot\boldsymbol{n}\, ds \tag{3.12}$$

which can be reduced using the boundary conditions. Let ∂R_1 be the part of the boundary where the displacement is specified, and let an external traction $\boldsymbol{t}_0$ be specified on the remaining boundary ∂R_2. The boundary integral (3.12) then reduces to

$$\begin{aligned}\oint_{\partial R} (\boldsymbol{\sigma v})\cdot\boldsymbol{n}\, ds &= \int_{\partial R_1} (\boldsymbol{\sigma v})\cdot\boldsymbol{n}\, ds + \int_{\partial R_2} (\boldsymbol{\sigma v})\cdot\boldsymbol{n}\, ds \\ &= \int_{\partial R_2} \boldsymbol{t}_0\cdot\boldsymbol{n}\, ds \end{aligned} \tag{3.13}$$

since $\boldsymbol{v} = 0$ where the displacement is specified on the boundary, and because $\boldsymbol{\sigma v}\cdot\boldsymbol{n} = \boldsymbol{\sigma n}\cdot\boldsymbol{v}$ since $\boldsymbol{\sigma}$ is symmetric, and $\boldsymbol{\sigma n} = \boldsymbol{t}_0$ according to (2.39).

Note that the product $\boldsymbol{\sigma}\cdot\nabla\boldsymbol{v}$ can be rewritten as $\boldsymbol{\sigma}\cdot\boldsymbol{\epsilon}(\boldsymbol{v})$ since (writing $\boldsymbol{L} = \nabla\boldsymbol{v}$ for convenience)

$$\boldsymbol{\sigma}\cdot\nabla\boldsymbol{v} = \boldsymbol{\sigma}\cdot\boldsymbol{L}$$

$$
\begin{aligned}
&= \sigma_{ij} L_{ij} \\
&= \tfrac{1}{2}(\sigma_{ij} + \sigma_{ji}) L_{ij} \\
&= \tfrac{1}{2}(\sigma_{ij} L_{ij} + \sigma_{ij} L_{ji}) \\
&= \tfrac{1}{2}\sigma_{ij}(L_{ij} + L_{ji}) \\
&= \boldsymbol{\sigma}\cdot\boldsymbol{\epsilon}(\boldsymbol{v}). \qquad (3.14)
\end{aligned}
$$

Hence the *variational* or *weak* formulation of the problem becomes, using equations (2.41), (3.13) and (3.14):
Find $\boldsymbol{u} \in U$ such that for arbitrary $\boldsymbol{v} \in V$

$$\int_R \boldsymbol{C}\boldsymbol{\epsilon}(\boldsymbol{u})\cdot\boldsymbol{\epsilon}(\boldsymbol{v})\, dV = \int_R \boldsymbol{v}\cdot\boldsymbol{f}\, dV + \int_{\partial R_2} \boldsymbol{t}_0\cdot\boldsymbol{v}\, ds \qquad (3.15)$$

3.2 The Discrete Problem

In the general case, equation (3.15) cannot be solved analytically. One way of constructing an approximate solution is to use the Galerkin method, in which V is replaced by finite-dimensional subspaces V^h [57]. Whereas V is an infinite-dimensional space spanned by an infinite number of basis functions, that is

$$V = \text{span}\,\{\phi_i\}_{i=1}^{\infty}, \qquad (3.16)$$

and V^h is a finite-dimensional subspace of V spanned by N basis functions:

$$V^h = \text{span}\,\{\phi_i\}_{i=1}^{N} \qquad (3.17)$$

The parameter h satisfies $0 < h < 1$ and is a measure of how closely V^h resembles V. One appropriate definition would be $h = 1/\dim V^h$. The approximate solutions and test functions are given by

$$\boldsymbol{u}_h = \sum_{i=1}^{N} \boldsymbol{a}_i \phi_i \qquad (3.18)$$

$$\boldsymbol{v}_h = \sum_{i=1}^{N} \boldsymbol{b}_i \phi_i \qquad (3.19)$$

respectively where $\boldsymbol{a}_i$ and $\boldsymbol{b}_i$ are vectors of constants in the Galerkin approximation. The problem (3.15), when posed on V^h, now reduces to

$$\int_R \boldsymbol{C}\boldsymbol{\epsilon}(\boldsymbol{u}_h)\cdot\boldsymbol{\epsilon}(\boldsymbol{v}_h)\, dV = \int_R \boldsymbol{v}_h\cdot\boldsymbol{f}\, dV + \int_{\partial R_2} \boldsymbol{t}_0\cdot\boldsymbol{v}_h\, ds \qquad (3.20)$$

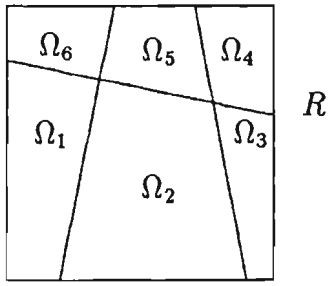

Figure 3.2: Subdivision of a two-dimensional domain R into finite elements Ω_e. The collection of all the elements is called the *finite element mesh.*

The Galerkin method does not specify how the basis $\{\phi_i\}$ should be chosen, and the finite element method is a procedure for making such a choice systematically. In the finite element method, the domain R is divided into nonoverlapping subdomains Ω_e such that the following conditions hold:

$$\Omega_e \bigcap \Omega_f = \emptyset \text{ for } e \neq f \quad \text{and} \quad \bigcup_{e=1}^{E} \overline{\Omega_e} = \overline{R} \tag{3.21}$$

Equation (3.20) then takes the form

$$\begin{aligned} \int_{\Omega_1} C\epsilon(\boldsymbol{u}_h^{(1)})\cdot\epsilon(\boldsymbol{v}_h^{(1)})\, d\Omega_1 + \int_{\Omega_2} C\epsilon(\boldsymbol{u}_h^{(2)})\cdot\epsilon(\boldsymbol{v}_h^{(2)})\, d\Omega_2 + \ldots \\ + \int_{\Omega_e} C\epsilon(\boldsymbol{u}_h^{(e)})\cdot\epsilon(\boldsymbol{v}^{(e)})\, d\Omega_e \\ = \int_{\Omega_1} \boldsymbol{v}_h^{(1)}\cdot\boldsymbol{f}\, d\Omega_1 + \int_{\Omega_2} \boldsymbol{v}_h^{(2)}\cdot\boldsymbol{f}\, d\Omega_2 + \ldots \\ + \int_{\Omega_e} \boldsymbol{v}_h^{(e)}\cdot\boldsymbol{f}\, d\Omega_e \\ + \int_{\partial R_2} \boldsymbol{t}\boldsymbol{v}_h^{(1)}\cdot\boldsymbol{n}\, ds + \int_{\partial R_2} \boldsymbol{t}\boldsymbol{v}_h^{(2)}\cdot\boldsymbol{n}\, ds + \cdots \\ + \int_{\partial R_2} \boldsymbol{t}\boldsymbol{v}_h^{(e)}\cdot\boldsymbol{n}\, ds \end{aligned} \tag{3.22}$$

where $\boldsymbol{u}_h^{(e)}$ denotes the restriction of $\boldsymbol{u}_h$ to element Ω_e. An example of the subdivision of a domain into finite elements is given in Figure 3.2. The crux of the finite element method lies in choosing an appropriate basis for the displacements. This is done as depicted in Figure 3.3; note that all basis functions have small support: they are zero outside a "small" region. Polynomial basis functions of compact support on R are chosen in such a way that

$$\boldsymbol{u}_h(\boldsymbol{x}_j) \;=\; \boldsymbol{a}_j \tag{3.23}$$

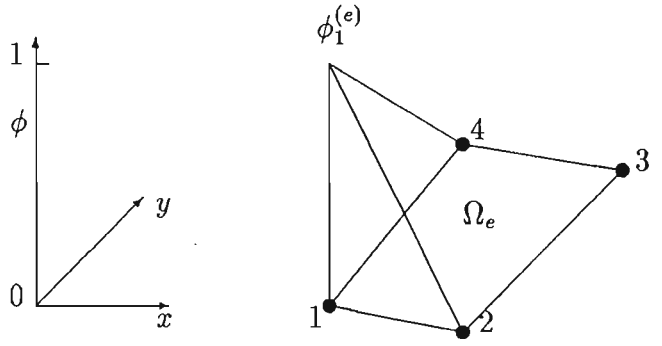

Figure 3.3: Bilinear basis function in two dimensions.

and

$$\boldsymbol{u}_h(\boldsymbol{x}) = \sum_{i=1}^{N} \boldsymbol{a}_i \phi_i. \tag{3.24}$$

The displacement on a particular element can be expanded using only the basis functions corresponding to the nodes of that element, as all other basis functions are zero on this element. Thus for a four-noded quadrilateral element with bilinear basis functions, the displacement on one element is given by

$$\boldsymbol{u}_h(\boldsymbol{x}) = \sum_{i=1}^{4} \boldsymbol{a}_i \psi_i^{(e)} \tag{3.25}$$

where $\boldsymbol{a}_i$ is a the vector of displacements at node i and $\psi_i^{(e)}$ is the restriction of basis function ϕ_i to element Ω_e. ψ_i is the non-zero basis function at node i. The approximate solution on each element Ω_e then satisfies

$$\int_{\Omega_e} C\epsilon(\boldsymbol{u}_h^{(e)})\cdot\epsilon(\boldsymbol{v}_h^{(e)})\, d\Omega_e = \int_{\Omega_e} \boldsymbol{v}_h^{(e)}\cdot\boldsymbol{f}\, d\Omega_e + \int_{\partial\Omega_e} \boldsymbol{t}\cdot\boldsymbol{v}_h\, ds + \int_{\partial R_2} \boldsymbol{t}_0\cdot\boldsymbol{v}_h\, ds, \tag{3.26}$$

where the second term of the right-hand side is the force exerted on each element by the surrounding elements, and the third term on the right-hand side is the force exerted on the element by the boundary tractions; this is only non-zero if part of the element boundary corresponds to part of ∂R_2.

As some of the analyses are carried out under a two-dimensional plane strain conditions, further details will be given for this case. In a two-dimensional plane strain situation, the displacement in the z-direction is zero, and the displacement field satisfies, in vector form,

$$\boldsymbol{u}^T = \begin{pmatrix} u(x,y) & v(x,y) & 0 \end{pmatrix}. \tag{3.27}$$

This means that the strain ϵ can be written as a 3-vector as all out of plane strain components are constrained to be zero: thus

$$\epsilon = \begin{pmatrix} \epsilon_{11} \\ \epsilon_{22} \\ 2\epsilon_{12} \end{pmatrix} = \begin{pmatrix} \partial u/\partial x \\ \partial v/\partial y \\ \partial u/\partial y + \partial v/\partial x \end{pmatrix}. \tag{3.28}$$

The stress is defined in the same manner as

$$\boldsymbol{\sigma} = \begin{pmatrix} \sigma_{11} \\ \sigma_{22} \\ \sigma_{12} \end{pmatrix}; \tag{3.29}$$

there is an out-of-plane component σ_{33} which does not enter the analysis because the corresponding strain ϵ_{33} is zero and hence this component will not contribute to the product $\boldsymbol{\epsilon}\cdot\boldsymbol{\sigma}$. Thus in two dimensions the product $\boldsymbol{\sigma}\cdot\boldsymbol{\epsilon}$ reduces to

$$\begin{aligned} \boldsymbol{\sigma}\cdot\boldsymbol{\epsilon} &= \sigma_{ij}\epsilon_{ij} \\ &= \sigma_{11}\epsilon_{11} + \sigma_{12}\epsilon_{12} + \sigma_{21}\epsilon_{21} + \sigma_{22}\epsilon_{22} \\ &= \sigma_{11}\epsilon_{11} + 2\sigma_{12}\epsilon_{12} + \sigma_{22}\epsilon_{22} \\ &= \boldsymbol{\sigma}^T\boldsymbol{\epsilon}. \end{aligned} \tag{3.30}$$

In this work, bone is assumed to exhibit isotropic behavior so that the tensor C_{ijkl} only has two independent components, for example the elastic modulus E and Poisson's ratio ν (see Section 2.3). For plane strain, the stress-strain relationship becomes

$$\boldsymbol{\sigma} = \boldsymbol{D}\boldsymbol{\epsilon} \tag{3.31}$$

where the 3×3 matrix $\boldsymbol{D}$ is defined by [10]

$$\boldsymbol{D} = \frac{E}{(1+\nu)(1-2\nu)} \begin{pmatrix} 1-\nu & \nu & 0 \\ \nu & 1-\nu & 0 \\ 0 & 0 & \frac{1-2\nu}{2} \end{pmatrix}. \tag{3.32}$$

The strains can be evaluated using (2.34), to give

$$\boldsymbol{\epsilon}(\boldsymbol{u}_h) = \boldsymbol{B}\boldsymbol{a} \tag{3.33}$$

$$\boldsymbol{\epsilon}(\boldsymbol{v}_h) = \boldsymbol{B}\boldsymbol{b}, \tag{3.34}$$

where the matrix $\boldsymbol{B}$ consists of basis function derivatives:

$$\boldsymbol{B} = \begin{pmatrix} \phi_{1,x} & 0 & \phi_{2,x} & 0 & \phi_{3,x} & 0 & \phi_{4,x} & 0 \\ 0 & \phi_{1,y} & 0 & \phi_{2,y} & 0 & \phi_{3,y} & 0 & \phi_{4,y} \\ \phi_{1,y} & \phi_{1,x} & \phi_{2,y} & \phi_{2,x} & \phi_{3,y} & \phi_{3,x} & \phi_{4,y} & \phi_{4,x} \end{pmatrix} \tag{3.35}$$

The left hand side of the variational problem (3.26) now becomes, for a particular element Ω_e

$$\begin{aligned}\int_{\Omega_e} C\epsilon(\boldsymbol{u}_h)\cdot\epsilon(\boldsymbol{v}_h)\,d\Omega &= \int_{\Omega_e} \boldsymbol{\sigma}(\boldsymbol{u}_h)\cdot\epsilon(\boldsymbol{v}_h)\,d\Omega_e \\ &= \int_{\Omega_e} \epsilon(\boldsymbol{v}_h)^T\boldsymbol{\sigma}(\boldsymbol{u}_h)\,d\Omega_e \\ &= \boldsymbol{b}^T\int_{\Omega_e} \boldsymbol{B}^T\boldsymbol{D}\epsilon(\boldsymbol{u}_h)\,d\Omega_e \\ &= \boldsymbol{b}^T\left(\int_{\Omega_e} \boldsymbol{B}^T\boldsymbol{D}\boldsymbol{B}\,d\Omega\right)\boldsymbol{a}. \end{aligned} \tag{3.36}$$

Similarly, by introducing a matrix $\boldsymbol{\Phi}$ such that

$$\boldsymbol{\Phi} = \begin{pmatrix} \phi_1 & \phi_1 & \phi_1 \\ \phi_2 & \phi_2 & \phi_2 \\ \phi_3 & \phi_3 & \phi_3 \\ \phi_4 & \phi_4 & \phi_4 \end{pmatrix}, \tag{3.37}$$

the right hand side becomes

$$\text{RHS} = \boldsymbol{b}^T\int_{\Omega_e} \boldsymbol{\Phi}^T\boldsymbol{f}\,d\Omega + \boldsymbol{b}^T\int_{\partial\Omega_e} \boldsymbol{\Phi}^T\boldsymbol{t}_e\,ds + \boldsymbol{b}^T\int_{\partial R_2} \boldsymbol{\Phi}^T\boldsymbol{t}_0\,ds \tag{3.38}$$

Here the symmetry of $\boldsymbol{D}$ and (2.22) have been used. Since $\boldsymbol{v}_h$ is a field of arbitrary displacements, and hence $\boldsymbol{b}$ a vector of arbitrary displacements, it follows that

$$\boldsymbol{K}_e\boldsymbol{a} = \boldsymbol{F}_e, \tag{3.39}$$

where

$$\boldsymbol{K}_e = \int_{\Omega_e} \boldsymbol{B}^T\boldsymbol{D}\boldsymbol{B}\,d\Omega \tag{3.40}$$

and

$$\boldsymbol{F}_e = \int_{\Omega_e} \boldsymbol{f}\,d\Omega + \int_{\partial\Omega_e} \boldsymbol{t}_e\phi\,ds + \int_{\partial R_2} \boldsymbol{t}_0\phi\,ds \tag{3.41}$$

are called the element stiffness matrix and the element load vector respectively. These may be calculated on each element by the technique of mapping to the master element and using Gauss integration (see Section 3.3). Since the element load vector consists of loads applied to the element due to body forces, external surface tractions, as well as forces exerted by other surrounding elements, this equation cannot be solved on an element level if the solution for the surrounding elements is not known. Each element stiffness matrix and element loading vector form part of a global stiffness matrix $\boldsymbol{K}$ and

a global loading vector $\boldsymbol{F}$ which are assembled element by element. Since the domain R is partitioned into nonoverlapping finite elements Ω_e, this is possible:

$$\int_R \cdots = \sum_{e=1}^{E} \int_{\Omega_e} \cdots .$$

According to Newton's third law of motion, the forces applied by one element on a neighbouring one are equal and opposite to those applied by the neighbouring element on the original one, hence inter-element forces cancel, and only external forces have to be evaluated in the global equation

$$\boldsymbol{K}\boldsymbol{a} \;=\; \boldsymbol{F}. \tag{3.42}$$

Here, the vector $\boldsymbol{a}$ contains the displacements of every node in the model, and the force vector F contains only body forces and external tractions. The stiffness matrix $\boldsymbol{K}$ is a $2n \times 2n$ matrix, with n the total number of nodes in the model, since each node has two displacement degrees of freedom. Equation (3.42) is linear and has solution

$$\boldsymbol{a} \;=\; \boldsymbol{K}^{-1}\boldsymbol{F}. \tag{3.43}$$

The computational effort depends on the size of $\boldsymbol{K}$, which in turn is governed by the total number of degrees of freedom in the model. Thus a model such as that set up by Van Rietbergen [75] using 300 000 elements to model individual trabecular structures is very expensive to run and needs vast amounts of computer resources. To analyse a whole bone using this technique is impossible with today's hardware. The macroscopic approach, on the other hand, allows one to analyse a whole bone: a fully three-dimensional remodelling analysis using a continuum algorithm on a femur divided into 6000 elements only has about 18000 displacement degrees of freedom. A further complication of the approach based on single trabecular structures is that at least some of these trabeculae undergo finite strains, the small strain approximation is no longer be valid, and the strain-displacement relationship becomes nonlinear. It is computationally very expensive to solve these nonlinear equations, since at each step not one but several different stiffness matrices have to be inverted until the solution $\boldsymbol{a}$ is found [16]. This sort of approach may become feasible in the future. At the moment, existing methodologies used for solving complex engineering problems such as the loading on a bone, which is made complicated both by its geometry and by the behaviour of the bone material, favour a continuum mechanics or macroscopic approach.

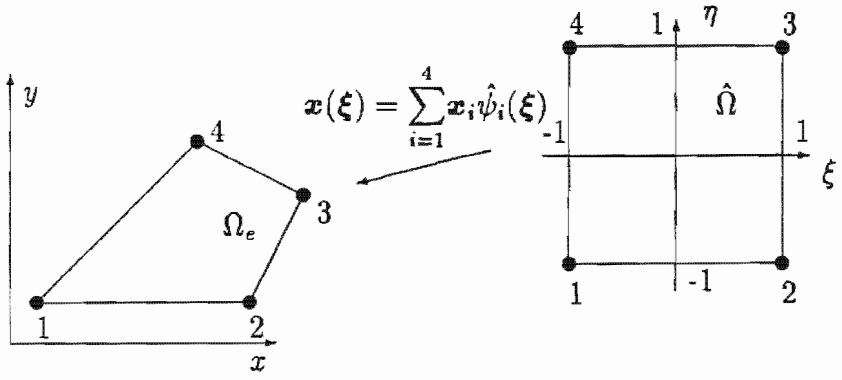

Figure 3.4: Two-dimensional map from a master element to a 4-noded quadrilateral element.

3.3 Evaluation of Integrals

To make the calculation of integrals easier, each four-noded quadrilateral element is mapped onto a standard master element $\hat{\Omega}$, where all the integrations are performed numerically. This map takes the form

$$\boldsymbol{x} = \boldsymbol{x}(\boldsymbol{\xi}) \tag{3.44}$$

and in the case of plane strain is a two-dimensional map:

$$\begin{pmatrix} x \\ y \end{pmatrix} = \begin{pmatrix} x(\xi,\eta) \\ y(\xi,\eta) \end{pmatrix} \tag{3.45}$$

(see Figure 3.4). The bilinear basis functions shown in Figure 3.3 on the master element are easy to determine by using the fact that

$$\psi_i(\boldsymbol{\xi}_j) = \delta_{ij}$$

where δ_{ij} is the Kronecker delta (see equation (2.4)). They are

$$\begin{aligned} \hat{\psi}_1 &= \tfrac{1}{4}(1-\xi)(1-\eta) \\ \hat{\psi}_2 &= \tfrac{1}{4}(1+\xi)(1-\eta) \\ \hat{\psi}_3 &= \tfrac{1}{4}(1+\xi)(1+\eta) \\ \hat{\psi}_4 &= \tfrac{1}{4}(1-\xi)(1+\eta) \end{aligned} \tag{3.46}$$

VUing these basis functions, the map in equation (3.45) can conveniently be rewritten as

$$\boldsymbol{x}(\boldsymbol{\xi}) = \sum_{i=1}^{n} \boldsymbol{x}_i \hat{\psi}_i(\boldsymbol{\xi}) \tag{3.47}$$

where i runs over all nodes of the element ($i = 1$ to 4 in the bilinear quadrilateral case) and $\boldsymbol{x}_i$ is the position vectors of node i in the element.

In order to transform the matrix $\boldsymbol{B}$ (see equation (3.35)) onto the master element, one can use the chain rule to obtain

$$\begin{pmatrix} \frac{\partial}{\partial \xi} \\ \frac{\partial}{\partial \eta} \end{pmatrix} = \begin{pmatrix} \frac{\partial x}{\partial \xi} & \frac{\partial y}{\partial \xi} \\ \frac{\partial x}{\partial \eta} & \frac{\partial y}{\partial \eta} \end{pmatrix} \begin{pmatrix} \frac{\partial}{\partial x} \\ \frac{\partial}{\partial y} \end{pmatrix} \tag{3.48}$$

The 2×2 matrix in (3.48) is called the *Jacobian matrix* of the transformation and is denoted by

$$\boldsymbol{J} = \frac{\partial \boldsymbol{x}}{\partial \boldsymbol{\xi}} \tag{3.49}$$

In the finite element method, convex quadrilaterals are used, and for these $\det \boldsymbol{J} > 0$ holds. For a convex quadrilateral, the mapping of the basis function derivatives onto the master element is given by

$$\begin{pmatrix} \frac{\partial \phi_i}{\partial \xi} \\ \frac{\partial \phi_i}{\partial \eta} \end{pmatrix} = \boldsymbol{J}^{-1} \begin{pmatrix} \frac{\partial \phi_i}{\partial \xi} \\ \frac{\partial \phi_i}{\partial \eta} \end{pmatrix}. \tag{3.50}$$

The matrix $\boldsymbol{B}$ can be rewritten in terms of the basis function derivatives on the master element as $\widehat{\boldsymbol{B}}$. Hence by calculating the derivatives of the basis functions as well as the Jacobian matrix for each element one can do all the integration on the master element. The infinitesimal volume element in the case of plane strain reduces to

$$d\Omega_e = t \det \boldsymbol{J}\, d\xi d\eta, \tag{3.51}$$

where t is the thickness which has to be specified for each element. If one denotes $\det \boldsymbol{J}$ by J, then the integrals[1] over the master element become

$$\boldsymbol{K}_e = \int_{\hat{\Omega}} \widehat{\boldsymbol{B}}^T \boldsymbol{D} \widehat{\boldsymbol{B}} t\, J\, d\xi d\eta, \tag{3.52}$$

$$\boldsymbol{F}_e = \int_{\hat{\Omega}} \boldsymbol{f}\, t\, J\, d\xi d\eta. \tag{3.53}$$

After mapping an integral onto the master element, it is evaluated numerically by using Gauss integration, as dicussed in Dhate and Touzot [31] or Burnett [10]. This means that the integral over the element is replaced by the sum of the integrand evaluated

[1]Note: the external force part of the load vector $\boldsymbol{F}$ (see equation (3.41)) is not evaluated here; this is because most of the loads in this study are concentrated nodal loads, which are applied directly to the nodes concerned without any integration calculations. In Section 6.3, application of external loads which are distributed over an element surface will be discussed.

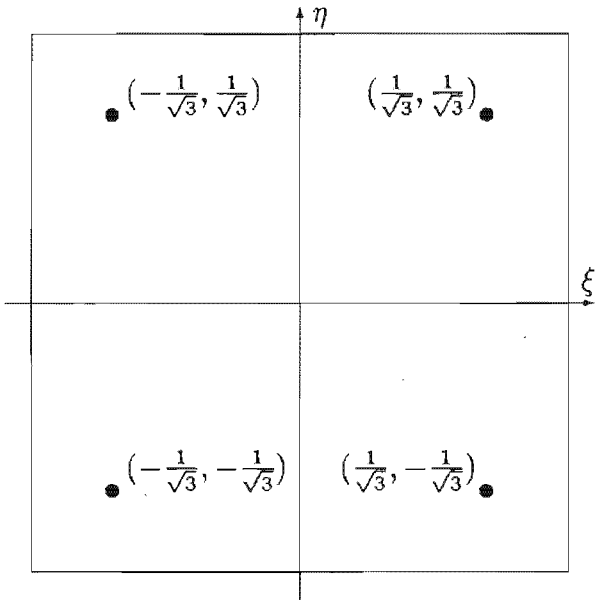

Figure 3.5: Gauss points needed for exact integration on a four-noded quadrilateral master element $\hat{\Omega}$ with bilinear basis functions.

at various strategically chosen points in the domain ("Gauss points") that are weighted appropriately. For bilinear basis functions, the Gauss points that will give an exact evaluation of the integral lie at $(-\frac{1}{\sqrt{3}}, -\frac{1}{\sqrt{3}})$; $(\frac{1}{\sqrt{3}}, -\frac{1}{\sqrt{3}})$; $(-\frac{1}{\sqrt{3}}, \frac{1}{\sqrt{3}})$; $(\frac{1}{\sqrt{3}}, \frac{1}{\sqrt{3}})$ in the $\xi - \eta$ plane (see Figure 3.5) and all have weight 1 so that the integral reduces to

$$\int_{\hat{\Omega}} \boldsymbol{f}(\xi, \eta) J(\xi, \eta)\, d\xi d\eta \;=\; \sum_{i=1}^{4} \boldsymbol{f}(\boldsymbol{p}_i) J(\boldsymbol{p}_i) \tag{3.54}$$

where $\boldsymbol{p}_i$ are the coordinates of each Gauss point. This approximation will evaluate the integral exactly providing that the shape functions are bilinear [31].

Chapter 4

Continuum Model for Isotropic Density Remodelling

There are two schools of thought that have developed theories utilizing a scalar approach to bone remodelling: the University of Nijmegen school (Huiskes et al.) [78] [42] and the Stanford University school (Carter et al.) [47] [13] [12]. Huiskes et al. use the strain energy density U as a remodelling stimulus [42], whereas Carter et al. use a daily stress level stimulus ψ [12]. According to Carter et al., researchers have tried to show that apparent density and trabecular orientation adjust themselves to optimise some objective function which could be different from stress ratio: e.g. strain energy density [12]. In a realistic model this strain energy density function has to include damage accumulation as well as static stress. It is assumed that some homeostatic state exists in which no bone is lost or gained. The stimulus required for maintenance of bone is a function of stress magnitudes, loading cycles and apparent density. Both these schools of thought have developed isotropic material models with the state of bone being characterized by a single scalar: the apparent density ρ^*, which will simply be denoted by ρ from now on. The theory of the Stanford group will be described in some more detail below; this model will henceforth be referred to as the SE algorithm.

4.1 Similarities of Bone and Damage Mechanics

The model presented below represents one of the simplest approaches one can take when simulating bone remodelling, yet the formulae may seem quite confusing at first glance.

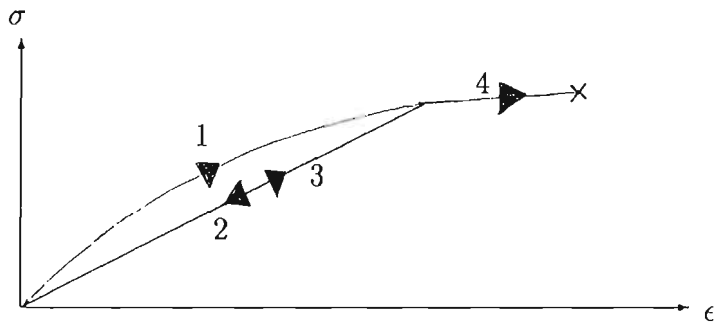

Figure 4.1: Stress-strain curve of a material undergoing tensile loading in the sequence 1-2-3-4: as the material is loaded, the damage increases, resulting in a decreasing elastic modulus. The material is elastic as loading (1,3) and unloading (2) causes no permanent deformation.

It is helpful to outline the basic features of the model before delving into the details of the formulation.

The model is simple in that it involves only elastic deformations, so that plastic effects are neglected. What makes it different from a normal linear elastic model is that the material properties change with time (see Section 2.4.1), reflecting the real-life ability of bone to remodel. One can draw a parallel with damage mechanics, where the stiffness of a material undergoing damage depends on a damage parameter d which changes as the load is applied [71]. In reality, every material contains some flaws, cracks or microvoids that grow when the material is loaded in a tensile manner. Under compression, the microcracks close and hence the material retains its elastic properties, but in tension the cracks grow, making the material weaker. This is referred to as damage, and in a damaged material the elastic modulus E changes according to

$$E = (1-d)E_0, \tag{4.1}$$

where E_0 is the original (undamaged) modulus of the material and $d(t)$ is such that

$$0 \leq d(t) \leq d_r < 1 \tag{4.2}$$

with d_r the value of d where the material ruptures [71] (see Figure 4.1). The constitutive equations for a damage model include an evolution equation for $d(t)$, which is of the form

$$\dot{d} = f(d, \epsilon, \sigma). \tag{4.3}$$

In damage mechanics, the material degrades continually so that the damage parameter increases as time progresses (ie $\dot{d} \geq 0$), whereas bone has the ability both to degrade

(resorption) and to strengthen (apposition). The elastic properties depend directly on the relative density ρ, and this parameter can be seen in the same light as the damage parameter d in damage mechanics. Thus the equations for bone remodelling consist of the elastic constitutive equations together with an evolution equation

$$\dot{\rho} = g(\rho, \epsilon, \sigma) \tag{4.4}$$

for the density. The explicit form of these equations will be given in the following Sections.

4.2 Surface and Internal Remodelling Combined

The first step towards producing a general continuum theory for bone remodelling is to combine the internal (density), and the surface remodelling approaches, since the two are really caused by the same phenomenon, namely surface deposition of bone matrix by the osteoblast cells. This is quite obvious on the bone's outer surface, which can actually be seen to grow or shrink according to the loads applied (see Figure 2.4). Density remodelling is really caused by bone deposition or resorption on the bone-marrow interface wherever there is available surface area, such as around trabeculae or on any free surface. Hence remodelling is very slow at very low or very high apparent density, as there is not very much surface available for bone deposition in either case. The amount of available bone surface, ie. the free surface area per typical unit volume of bone, as a function of density (specific surface area) was quantified by Martin [59] [60]. He showed that to a very good approximation, specific surface area (denoted by S_V) is a fifth order polynomial in the porosity $\hat{p} = 1 - \frac{\rho}{\hat{\rho}}$, where $\hat{\rho}$ is the density of the bone material itself, ie. bone with no porosity (cortical bone still has a porosity of 5 %; its density is denoted by ρ_c.). Martin has shown that this holds for all kinds of bone, both young and mature, as well as bone taken from various regions of the body [60]. The dependence of S_V on $\hat{p}$ is given by

$$S_V = 0.03226\hat{p} - 0.09394\hat{p}^2 + 0.13396\hat{p}^3 - 0.10104\hat{p}^4 + 0.02876\hat{p}^5. \tag{4.5}$$

This is depicted in Figure 4.2.

The density evolution depends on the available surface according to

$$\dot{\rho} = \dot{r} S_V \hat{\rho} \tag{4.6}$$

where $\dot{r}$, the velocity of the remodelling surface, depends on the remodelling error e, which is the difference between the actual stimulus and the daily tissue level stimulus:

$$e = \psi_t - \psi_t^* \tag{4.7}$$

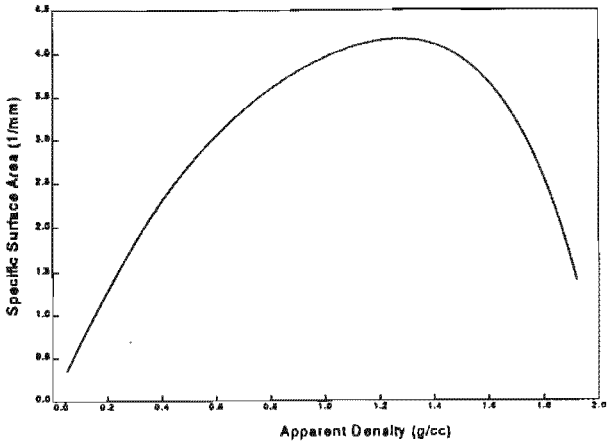

Figure 4.2: Plot of specific surface available vs porosity of cancellous bone material. Taken from Jacobs [47].

The remodelling error e will be discussed further in Section 4.4. The remodelling surface velocity $\dot{r}(e)$ can take several different forms, the simplest one being a linear function going through the origin, that is,

$$\dot{r} = ce. \tag{4.8}$$

This expression gives only one value of remodelling error (viz. zero) when the remodelling surface velocity is zero. Note that the parameter c can be set to give a specific remodelling surface velocity for a specific remodelling error, for example for the remodelling error due to complete unloading. Alternatively, c could be chosen in such a way as to represent the maximum possible remodelling surface velocity. This value has been measured experimentally [63] and is different for resorption and apposition of bone surface material. According to Beaupré et al. [6], this surface remodelling velocity is of the order of $3\,\mu m/day$. Experimental results, however, indicate that there exists a range of mechanical loading conditions that have no effect on remodelling [37]. Hence a form that is probably more realistic is one which includes a so-called *dead zone* [6], where there is a certain width w such that $-w \leq e \leq w \quad \Rightarrow \quad \dot{r} = 0$ while outside these limits, the remodelling surface velocity is a linear function of e (see Figure 4.3). The equation for the surface remodelling velocity for this reads

$$\dot{r} = \begin{cases} ce & e > w/2 \\ 0 & -w/2 \leq 0 \leq w/2 \\ ce & e < -w/2 \end{cases} \tag{4.9}$$

According to Carter [11], such a dead zone is different for different locations in the skeleton,

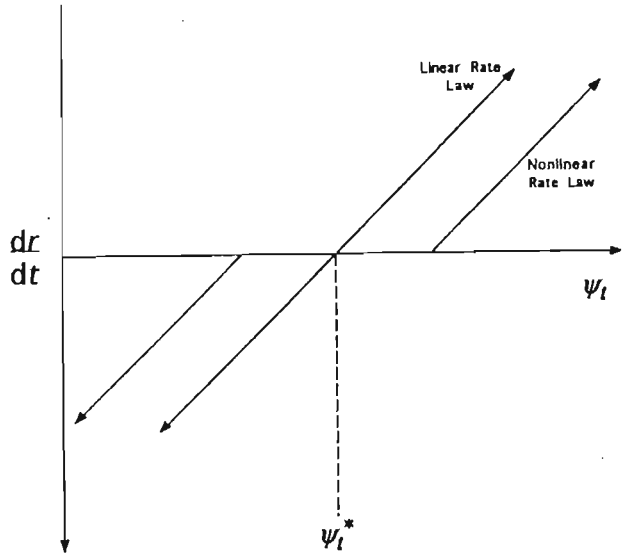

Figure 4.3: Different Surface Remodelling Rates: with and without a dead zone. Taken from Jacobs and Beaupré.

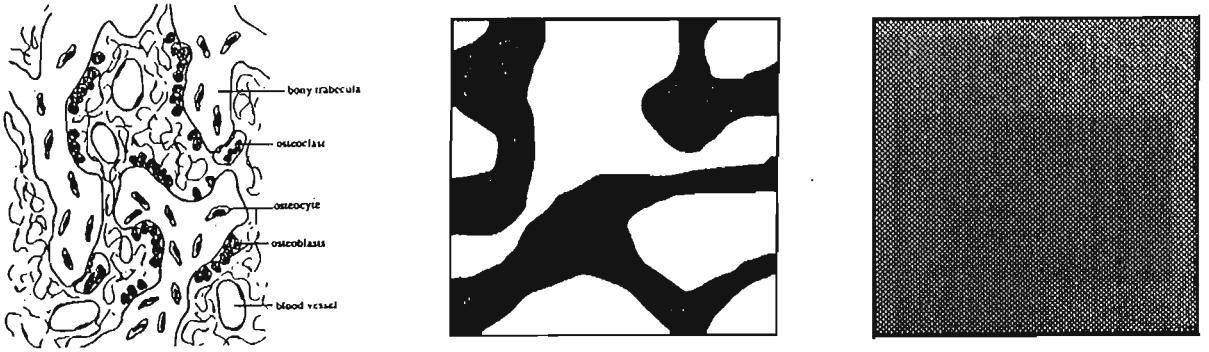

Figure 4.4: Cellular, Trabecular and Continuum Levels in Bone.

depending on whether the bone concerned serves as a structure loaded with cyclic loading (eg the lower limbs) or as an impact absorbing protective shield (eg the skull).

The results in the current study include a brief investigation of the effect that such a dead zone has on bone remodelling. An even more realistic representation would probably be to have a dead zone and then a function $\dot{r}(e)$ which tapers off as $e \to \pm\infty$. This will be included in the strain based remodelling algorithm presented in Chapter 5.

4.3 Tissue Level and Continuum Level

There are three different levels at which one can model cancellous bone: the cellular level, the coarser tissue level and the even coarser continuum level (see Figure 4.4). The cellular level goes down to a dimension of about 10Å, the tissue level has a smallest dimension of about $50\mu m$ (the size of a Haversian system), and the continuum level has dimensions

of the order of millimeters [26]. Discussions of attempts to model cancellous bone on a cellular level as well as on a trabecular level are described in Sections 5.2 and 2.4.3, respectively.

According to Jacobs [47] [12], the link between the tissue and the continuum levels is the equivalent stress :

$$\bar{\sigma} = \sqrt{2EU}, \tag{4.10}$$

with E the elastic modulus of the (isotropic) material and

$$U = \frac{\boldsymbol{\sigma} \cdot \boldsymbol{\epsilon}}{2} \tag{4.11}$$

the strain energy per unit volume stored in the material. Note that this is valid for a linear elastic material only. It is assumed in this model that all loading is everyday normal loading, and that the strain in the bone at no stage in the analysis exceeds the yield limit. The continuum stress $\bar{\sigma}$ and the tissue level stress $\bar{\sigma}_t$ are related by [77] [12]

$$\bar{\sigma}(\rho) = \left(\frac{\rho}{\hat{\rho}}\right)^2 \bar{\sigma}_t \tag{4.12}$$

This relationship can be derived using the theory of cellular solids [2], and has been verified experimentally for different cellular solids similar to bone and also for bone itself [34].

4.4 Equations and Parameters Used in the Continuum Model

Assume that during any day a variety of N different load cases are applied to a certain region of bone. If one defines the daily tissue stress stimulus by

$$\psi_t = \left(\sum_i^{\mathrm{N}} n_i \bar{\sigma}_{ti}^m\right)^{1/m} \tag{4.13}$$

where n_i represents the number of load cycles, $\bar{\sigma}_{ti}$ the equivalent stress for load case i, and m is a scalar such that $3 \leq m \leq 8$, then one can define a remodelling error

$$e = \psi_t - \psi_t^*, \tag{4.14}$$

where ψ_i^* represents a remodelling equilibrium value of stress. In terms of continuum level, scaling the equivalent stress from the tissue level to the continuum level yields

$$\psi_t = \left[\sum_i^{\mathrm{N}} n_i \left((\frac{\hat{\rho}}{\rho})^2 \bar{\sigma}_i \right)^m \right]^{1/m} = (\frac{\hat{\rho}}{\rho})^2 \psi \tag{4.15}$$

with

$$\psi = \left(\sum_i^{\mathrm{N}} n_i \bar{\sigma}_i^m \right)^{1/m} \tag{4.16}$$

and $\bar{\sigma}_i$ can be measured on the continuum level. The remodelling error then becomes

$$e = \psi \left(\frac{\hat{\rho}}{\rho} \right)^2 - \psi_t^* \tag{4.17}$$

4.5 Loading Application

The daily stress level stimulus is given by

$$\psi = \left(\sum_{i=1}^{\mathrm{N}} n_i \bar{\sigma}_i^m \right)^{1/m} \tag{4.18}$$

where N is the total number of load cases experienced in one day. Under normal loading conditions, there are numerous different load cases, as can be seen by considering all the different muscles attached to the femur in the hip region. Dostal et al. [32] have included 27 different hip muscles in their model of the hip musculature, and this is indicative of the variety of load cases which the proximal femur experiences during normal daily activity. To include all of these in a finite element model would be highly impractical, as each muscle is attached to a different area of the bone. It is also very difficult to quantify exactly where and in which direction each force is acting in a complicated action as, for example, climbing the stairs. In this work, the only loads simulated are those of the gait cycle which is sampled at several points in time: three points for the two-dimensional models and two points for the three-dimensional models. The two-dimensional load cases have been taken from Jacobs [47] and the three-dimensional load cases have been taken from Bergmann et al [8].

It is quite clear that during one day, various different load cases apply to the femur *in vivo*. The formula for the stress level stimulus is simplified, however, if one assumes that load cases of one specific kind are applied sequentially without any different load cases in

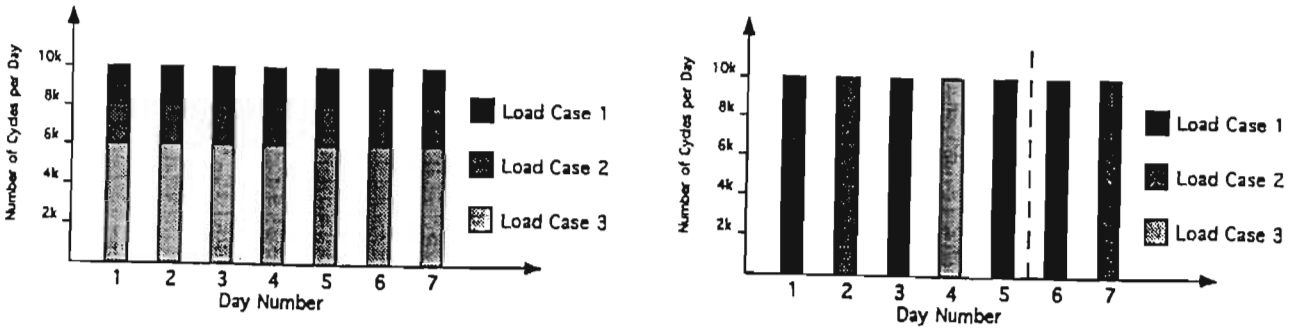

Figure 4.5: Reorganization of load cases to make calculations easier. Taken from Jacobs [47].

between. Assuming that only one particular load case is applied during a certain day, ie. N = 1 in the above equations, the stress level stimulus simplifies to

$$\psi = n^{1/m}\bar{\sigma} \tag{4.19}$$

where $\bar{\sigma}$ is the specific stress associated with this one load case. Thus by arranging the load cases in the model in such a way that only one applies during the shortest time-step in the model, the calculations can be simplified. Instead of going through a whole cycle of different load cases during one day, one goes through them sequentially on different days. More frequent loads are applied for more days than less frequent ones, e.g. in the two-dimensional model, there is one load case that has $n_1 = 6000$ cycles and two other load cases that have $n_i = 2000$ cycles each. Thus they are arranged in such a fashion that there is a day of loading case 1 (10000 load cycles) followed by a day of case 2 (10000 cycles) followed again by case 1 and then by case 3 and again by case 1, each applied for 10000 cycles respectively [47] (see Figure 4.5). The different load cases are thus spread over 5 iterations instead of all occuring during one iteration. The number of load cycles during one iteration, however, remains 10000. In this work, one iteration (ie. the application of one particular load case) will be referred to as one day. Since the elastic properties of the bone material change after each iteration, these two methods of loading will definitely give different results in the short term, but in the long term the effects of applying the load sequentially should average out [47].

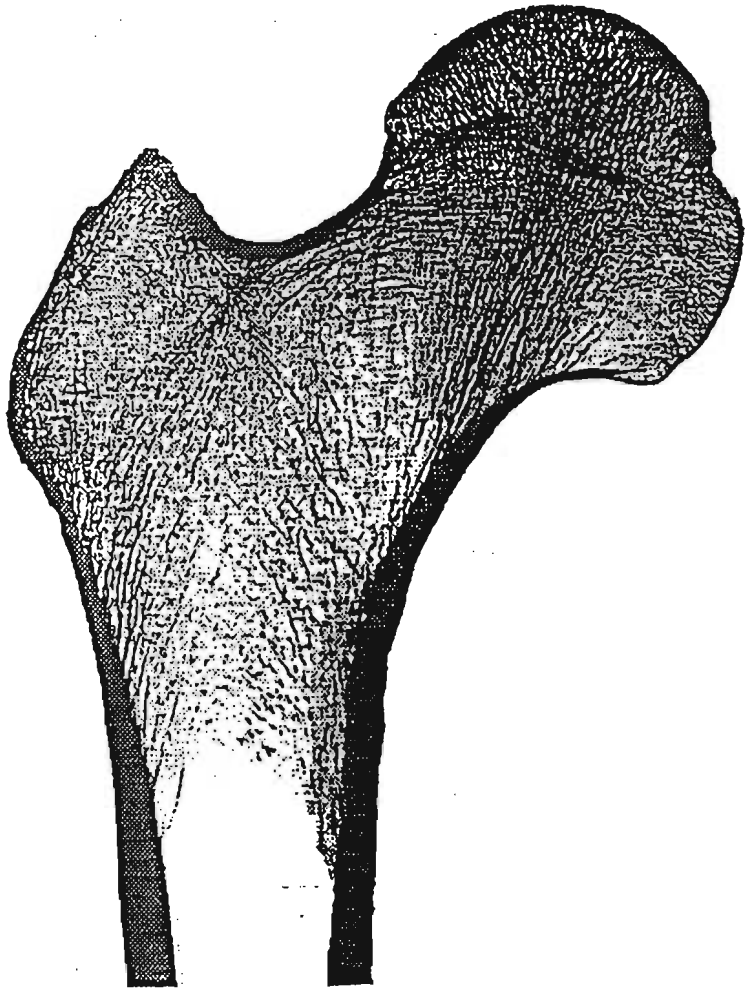

Figure 4.6: Radiograph of Human Femur in section.

4.6 Limitations of Using a 2D Model

Before applying the model described above to a two-dimensional problem for the human femoral head, one has to be quite clear about the advantages as well as the limitations of using this approximation. Clearly it is quite difficult to create a fully three-dimensional finite element mesh of a real bone as most bones have a very low degree of symmetry and a very complex geometry. This is much simplified in two dimensions, and as there are numerous radiographs of the human femur in section, one can compare results obtained from numerical analysis with these physiological trabecular distributions (see Figure 4.6). To obtain a feel for how different remodelling algorithms work and to test new algorithms, it is therefore instructive to model the stucture of the bone as two-dimensional. The main problem with this approach is that the hoop stresses set up in the cortex during loading are neglected. There are several ways in which one can at least partially overcome this problem; the most obvious is to assume conditions of plane strain so that the material is constrained to undergo deformations only in the plane of the finite element mesh. This simulates containment by a hard cortical shell and is effected by ascribing a constant

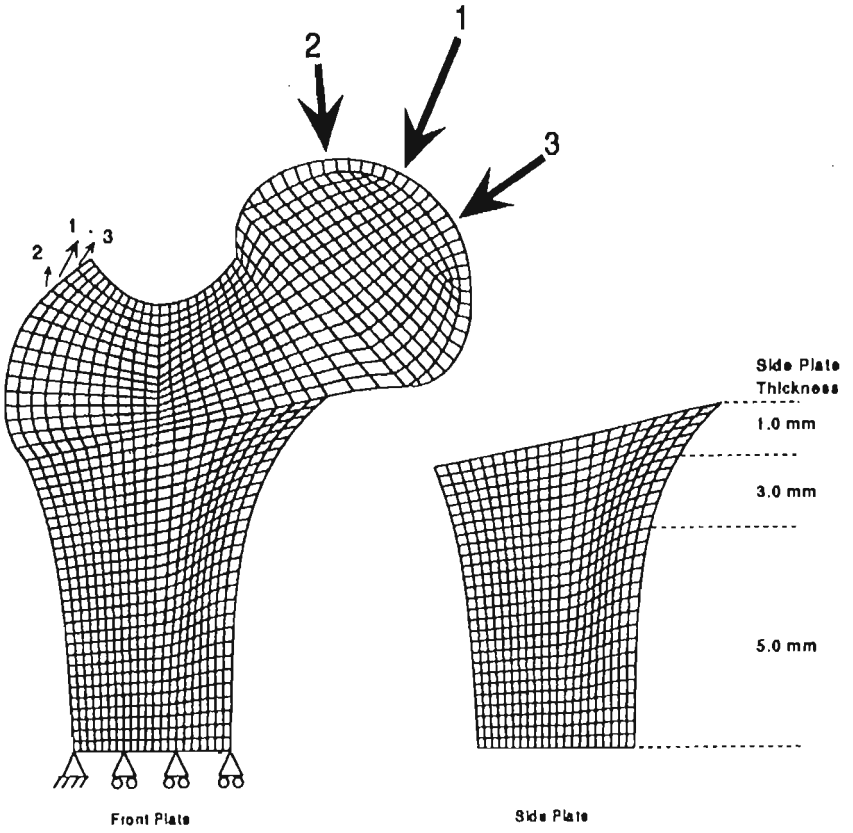

Figure 4.7: Mesh consisting of front plate with tapering side plate.

thickness to each element. In this work, the whole specimen is assumed to have a constant thickness of 40mm, which is obviously not a realistic assumption.

In order to reconstruct the tubular nature of the femoral shaft in a two-dimensional model, Jacobs et al. use a *side plate* consisting of cortical bone that is not allowed to remodel [47]. Thus a mesh identical to that used for the femoral shaft is superimposed on the original mesh, and this tapers down in thickness towards the femoral head. Its medial and lateral most nodes are constrained via a multi-point constraint to undergo the same displacements as the corresponding nodes in the original mesh (see Figure 4.7). This idea was first used by Huiskes et al. [41] to take the 3D integrity of a system, including an implant, into account. The sideplate is useful also for approximating the correct bending stiffness of the three-dimensional femoral shaft. As the bending stiffness depends on the product EI, where I is the second moment of area, the values of I for the cylindrical shaft and the rectangular 2D approximation including the side plate have to be the same. This can be done by varying the thickness of the original mesh and the side plate appropriately.

The problem with implementing a side plate in a study of bone remodelling is that the side plate was originally intended to simulate an already existing femoral shaft. In this work, however, the initial configuration is a bone of constant density with no pre-formed structural elements in place. Starting out with a block of uniform bone with a cortical

shell attached to it and arriving at a slab of bone that is half cortical and half remodelled cancellous bone is highly unphysiological. Also, the rigid side plate absorbs a large fraction of the applied load and hence the stress stimulus in the remodelling mesh is lowered, causing excessive resorption. This is shown in Figure 7.1 in Chapter 7. The side plate is definitely useful in adaptive bone remodelling, where an already existing bone structure adapts to a change in loading. Whether it is a valid model of reality in the development of the structural features of bone is a different matter. In this work, no side plate has been used in the two-dimensional simulations at all.

4.7 Algorithm Implemented on the Computer

The strain energy based algorithm described in this Chapter has been implemented using the ABAQUS finite element code with the user-defined UMAT subroutine which can be used to calculate constitutive parameters and stiffness matrices at each Gauss point in a bilinear quadrilateral element. The algorithm followed at each Gauss point is outlined in the Box 1. In order to implement this model, a number of parameters are required (see Box 4.2). These can be determined mostly from the literature. One interesting choice of parameter is that of the remodelling constant c, which was chosen in such a way that zero remodelling stimulus acting on solid bone $\hat{\rho}$ will result in a remodelling surface velocity of $1\mu m/day$ [47]. As will be shown in Section 5.4.3, this is not quite physiologically accurate, but it is within an order of magnitude of the actual physiological remodelling surface velocity. The density ρ_{crit} represents the bone density at which the dependence of elastic modulus E on density changes from $E = a\rho^{\alpha}$ $(\rho < \rho_{crit})$ to $E = b\rho^{\beta}$ $(\rho \geq \rho_{crit})$. Also, the value of Poisson's ratio changes at this density (see Box 4.1). The number m is an empirically determined constant that can take any value between 3 and 8. In this study, a value of $m = 4$ was adopted as in Carter et al. [13]. It is a weighting factor for the relative importance of the stress magnitude and the number of load cycles applied. An increasing value of m indicates an increasing dependence on activities causing high stress magnitudes [6] [12].

Box 4.1: Isotropic Bone Remodelling Algorithm

For each Gauss point, one state variable is needed: density ρ.

Given ϵ_n, $\Delta\epsilon_n$, σ_n, ρ_n:

Calculate $\Psi_n(\sigma_n, \epsilon_n) = n^{1/m}(\sqrt{E_n \sigma_n \cdot \epsilon_n})$

where $E_n = b\rho_n^\beta$

Calculate $\hat{p} = 1 - \frac{\rho_n}{\hat{\rho}}$

$S_V = 0.03226\hat{p} - 0.09394\hat{p}^2 + 0.13396\hat{p}^3 - 0.10104\hat{p}^4 + 0.02876\hat{p}^5$

Calculate $\dot{\rho}_n = c\hat{\rho}_n S_V \left(\left(\frac{\hat{\rho}}{\rho_n} \right)^2 \Psi_n - \Psi_t^* \right)$

Calculate $\rho_{n+1} = \rho_n + \Delta t \dot{\rho}_n$

Check whether $\rho_{min} \leq \rho_{n+1} \leq \hat{\rho}$

Update E, ν, λ, μ:

$$E = \begin{cases} a\rho_{n+1}^\alpha & \rho_{n+1} \leq \rho_{crit} \\ b\rho_{n+1}^\beta & \rho_{n+1} > \rho_{crit} \end{cases}$$

$$\nu = \begin{cases} \nu_1 & \rho_{n+1} \leq \rho_{crit} \\ \nu_2 & \rho_{n+1} > \rho_{crit} \end{cases}$$

$\lambda = \frac{E\nu}{(1+\nu)(1-2\nu)}$

$\mu = \frac{E}{2(1+\nu)}$

Update C_{n+1}:

$$C_{n+1} = \begin{pmatrix} \lambda + 2\mu & \lambda & 0 \\ \lambda & \lambda + 2\mu & 0 \\ 0 & 0 & \mu \end{pmatrix}$$

Update strain and stress:

$\epsilon_{n+1} = \epsilon_n + \Delta\epsilon$

$\sigma_{n+1} = C_{n+1}\epsilon_{n+1}$

Box 4.2: Parameters Required for Isotropic Bone Remodelling Algorithm

$\rho_{min} = 0.05\, g/cm^3$	$\alpha = 2.5$	$m = 4$
$\rho_{crit} = 1.2\, g/cm^3$	$\beta = 3.23$	$n = 10000$
$\rho_{cort} = 1.92\, g/cm^3$	$b = 1763$	$c = 0.02\, \mu m/MPa$
$\nu_1 = 0.25$	$a = 2014$	$\psi_t^* = 50 MPa$
$\nu_2 = 0.32$		

Chapter 5

Strain Based vs Strain Energy Based Modelling

As has been pointed out above (see Section 1.4), there are different views on which quantity to choose as a remodelling stimulus. Over the years, researchers have chosen different types of stimuli to quantify mechanical adaptation. Obviously for mechanical adaptation to occur one needs some sort of mechanical stimulus, and one has to decide between stress (σ) and strain (ϵ). That there is indeed a difference between models based on either of these two variables was shown by Simo et al [71], who highlighted the difference between a stress based and a strain based damage characterization. There is a bulk of evidence suggesting that strain or variables closely related to strain are the cause of remodelling, and some of this evidence will be presented in Section 5.1.2. As was pointed out in Section 4.1, continuum formulations of bone remodelling and damage mechanics are really quite similar. More will be said about strain and stress based models in the context of both bone and damage mechanics in Section 5.3. It will be argued that strain is really the physiologically correct variable on which to base a remodelling algorithm, and such an algorithm will be presented in Section 5.4. The structure of this algorithm follows that of the basic strain energy based SE algorithm formulated by the Stanford group, as described in Chapter 4.

5.1 Strain as a Remodelling Criterion

5.1.1 Strain and stress measurement

The main difference between the strain and the stress in a solid material is that the strain, being related to deformation, can be observed and measured directly; the stress, however, can only be quantified by virtue of measuring the strain it produces. It cannot be measured directly.

Strain was first measured *in vivo* by Lanyon et al. in 1969 [37], when they pioneered the technique of fastening strain gauges to bones in living animals. This technique has been refined and today not even postgraduate research students are spared. In one particular experiment a student had rosette strain gauges fastened to his skull [35] in order to determine the loading conditions under which the maximum strain is achieved in that part of the anatomy. Rosette strain gauges are three single strain gauges arranged in a plane at 45^o angles, so that strain magnitudes as well as the principal strain directions can be determined. An interesting result of this study was that more strain is measured during the act of chewing than when the skull is pounded with a rubber hammer [35]. One technical problem about attaching a strain gauge to a bone is that one has to remove part of the periosteum (the layer of osteogenic material that surrounds every free bone surface). Thus the mechanical environment of the bone is slightly altered when a strain gauge is mounted.

5.1.2 Some experimental results

Since the advent of *in vivo* measurement of strains caused by normal everyday activity or specific experimental loading, a variety of experiments have been carried out investigating the influence of various aspects of strain on remodelling. Some of these aspects and related results are outlined below.

Several experiments have been performed where a part of the ulna was removed, thus leaving the animal with a reduced bone cross-section under normal physiological or experimentally controlled loading [20] as discussed in Section 2.4.2. Cowin et al. [19] [20] have taken a number of these experimental data and used them to evaluate coefficients in their surface remodelling theory, which also had strain as a remodelling criterion. The results of these experiments were that the remaining bone is overstrained but compensates

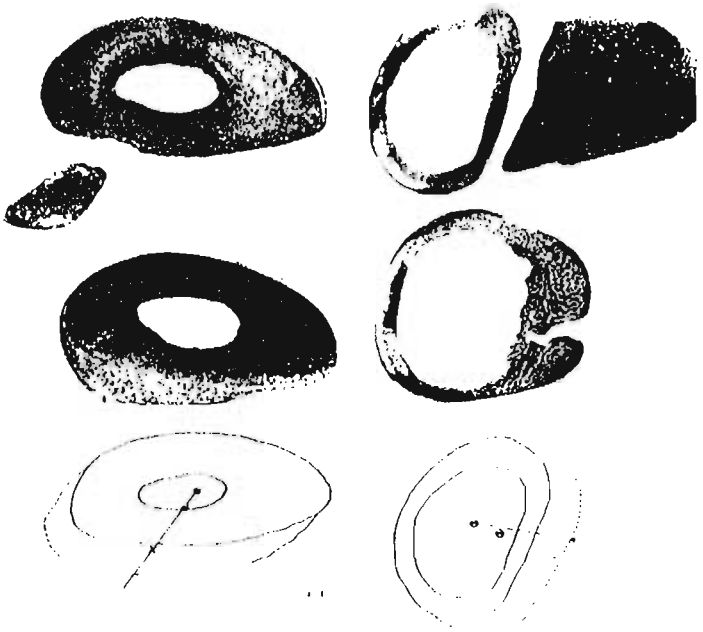

Figure 5.1: Results of the ulnar ostectomy experiment with mature sheep (from Lanyon 1982) (left) and young pigs (from Goodship 1979) (right). From top to bottom: control bone, experimental bone, theoretical prediction.

by Haversian bone apposition on the surface closest to the removed bone surface [51] (see Figure 5.1). The distribution of the remodelled bone matrix suggested that remodelling is not dependent on total strain levels, but rather on the strain distribution, as bending strains were reduced to below normal by the remodelled matrix.

Other experiments were designed to investigate other aspects of remodelling dependence on strain-related quantities, for instance strain rate, loading frequencey and strain distribution. Strain rate was first considered as a remodelling criterion when researchers realised that remodelling does not depend purely on the strain mode. Lanyon and Rubin [52] and Lanyon [53] have shown that remodelling is highly dependent on the rate at which straining takes place. To demonstrate this, Lanyon inserted two pins in a male turkey's ulna, thus preventing it from using its wing in a normal physiological fashion. The wing was put under *functional isolation* in this way [53]. Lanyon could then apply certain strains to the turkey's bone which were measured using the *in vivo* rosette strain gauge technique.

Strain magnitude. Several experiments conducted in the early and mid seventies have shown that typical physiological bone surface strains are of the same order of magnitude in a large variety of species including sheep, dogs, horses, turkeys and humans [37]. Physiological bone surface strains are of magnitudes between 2000 and 3000 microstrain. More demanding activities such as galloping, as opposed to trotting, increase the strain measured on locomotor apparatus bones [69]. This result is site-

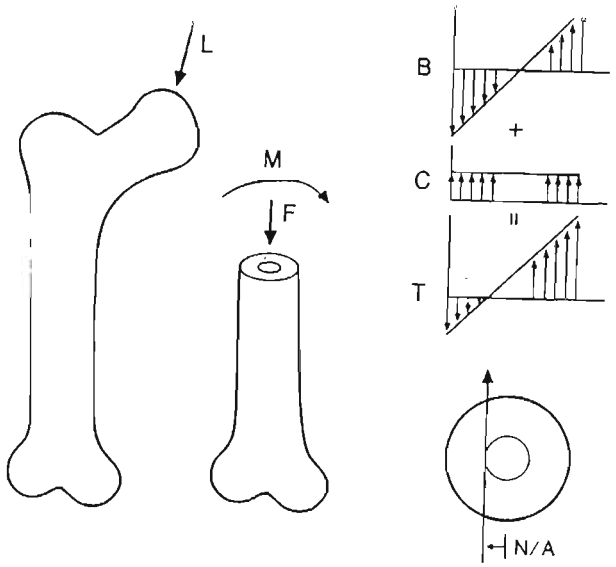

Figure 5.2: Superposition of bending and compressive loads in the human femur. Taken from Martin and Burr [37]. N/A indicates the bending neutral axis which undergoes no axial deformation at all.

independent in the sense that the physiological strains measured in various sites in the skeleton also fall into the same span of magnitudes: there is no difference in strain magnitude measured in a sheep femur and in a sheep humerus during trotting, for instance [37]. Turner [73] found that the yield strain in cancellous bone is almost the same in every direction , regardless of the loading orientation. He has argued that in an anisotropic material such as trabecular bone, trabeculae align such that the peak strains within the material are uniform and isotropic [77]. This suggests that strain is a very good criterion for remodelling: even if the yield stress is different according to the anisotropy of the material orientation, the yield strain is the same. One could assume the same to be true for some remodelling strain or a remodelling strain regime.

Strain modes. There is some argument about whether the mode of straining influences the remodelling response. Most bones in the locomotor apparatus experience more compression than tension: One can think about the loading on the femur, for instance, as being a bending load superimposed on a compressive load (see Figure 5.2). The fact that in most of the skeleton, compressive strains are larger and therefore contribute more to the remodelling action, could lead one to believe that tensile deformation does not cause any remodelling at all. Experimental results conflict and it is unclear whether remodelling depends on the strain mode. In all models in this work, there will be no distinction made between tensile and compressive modes as a stimulus for remodelling.

Strain rate and frequency. Lanyon [52] showed that application of a sufficiently high

load in a cyclic fashion stimulates remodelling. In this study, remodelling stimulation correlated most highly to peak strain rate. Also, a static strain applied to the turkey's ulna under functional isolation caused the same response as the functional isolation alone: net resorption [53]. Hence the strain has to change with time if it is to induce a remodelling reaction. It seems that a few strain cycles applied at a high strain rate are more efficient in stimulating a remodelling response than a large number of identical strain cycles applied at a slower rate.

There have been a number of studies indicating that impact loading causes a remodelling response [37], and it is possible that one only very few cycles of high-impact strain are required in order to elicit a substantial remodelling response. As far as the remodelling dependence on strain frequency is concerned, Rubin et al. [70] have been able to induce a remodelling response in the turkey ulna experiments by applying loads of 1000 microstrain for only four cycles per day. In the same experimental series, they have also shown that applying strains of this magnitudes for 36 cycles per day is just as effective as applying similar strains for 1800 cycles per day. Thus stimulus duration does not seem to play a large role in bone remodelling.

Strain distribution. The distribution of the applied strain does play a role, however, as was shown by the numerous ulna osteotomy experiments above, and also by an experiment carried out by Rubin and Lanyon [70] in which the turkey's ulna was bent around a neutral axes that was at 90° to the normal wing-flapping neutral bending axis. Large depositon of bone in some areas and resorption in others were the result.

All these experiments show that there is some strain dependence or dependence on the quantities associated with strain ("functional strain"), and therefore it is appropriate to investigate a remodelling criterion that depends intrinsically on strain.

5.2 The Osteocyte as a Strain-Sensor

As discussed in Section 1.3, osteocytes are cells that live in lacunae (tiny hollows) inside the calcified bone matrix and form the living part of solid cortical bone. Osteocytes are connected via long tendrils which run through the canaliculi in the solid bone matrix, and they are dependent on these connections for nutrients as they are surrounded by solid calcified matrix. Because of these connections, osteocytes can be viewed like neurons in

the brain which form a large neural network with millions of pathways carrying signals between the various cell bodies. Osteocytes communicate in a fashion similar to the neurons in the brain: if they receive a signal indicating strain on the bone matrix, they pass this signal down the array of osteocytes until it reaches osteoblasts on the bone matrix surface which then spring into action and create fresh bone matrix; thus one can model osteocytes as both the sensors and the activators of remodelling activity.

Recent theoretical developments have been designed to capture this strain-dependent behaviour by modelling the bone/bone-marrow matrix not as a continuum, but on a cellular level. To do this, the fluid contained in the canaliculae and Haversian canals in the bone matrix has to be taken into account: bone contains about 20% fluid by weight. Cowin et al. [26] have developed a model in which fluid flowing through the bone canaliculae that are filled with collagen fibres can act as a transmitter of strain signals. An analogy is a sponge filled with water. When it is pressed, the pore pressure changes and causes the water to move inside the spongy canals. The water-sponge composite material can thus sense strain. There has been some experimental evidence by Klein-Nulend et al. [49] that osteocytic tissue indeed senses fluid pressure changes (see Figure 5.3).

According to Cowin [26] and Pollack [66], fluid set in motion inside the canaliculae by strains in the bone matrix causes electric potentials to build up around the fibres embedded in the fluid. Pollack et al. [66] have put forward a theory of streaming potentials for osteons that is based on electrokinetic theory and continuum mechanics and is applied to the anatomical domain of an osteon. Values calculated using this theory were found to be largely in agreement with the experimental work of Starkebaum et al. [72], who measured electrical potentials set up in four-point osteonic bending specimens. Using a cable equation from electronics, one can also set up a cell-to-cell communication model. There is strong evidence that osteocytes communicate via electrical impulses, as the proteins that bridge gap junctions between adjacent osteocyte tendril fibres are the same that act as voltage actuators in the heart [26]. Hence a possible way of characterizing bone remodelling is to calculate fluid potentials set up by a certain strain field and to relate remodelling activity to the magnitudes of the pulses induced by such potentials along the osteocyte tendrils. This theory is still in the developing stages [26]. Similar to Cowin's theory of anisotropic fabric remodelling (see Section 2.4.3), this theory will have a variety of parameters governing remodelling activity, but these will correspond to physical dimensions of the bone tissue. Hence it will be easy to determine the parameters once the theory has been completed. As stated earlier, working on a cellular level is computationally expensive for any macroscopic bone model, and it will not be possible to

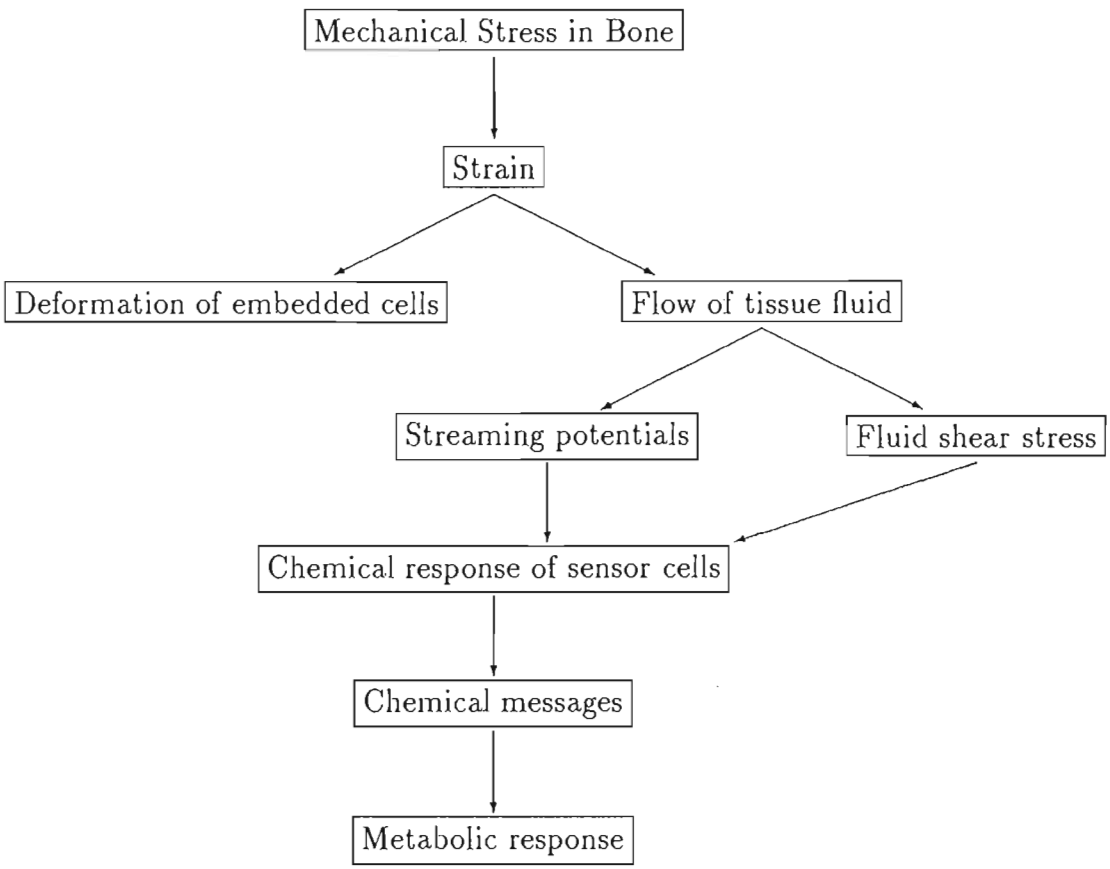

Figure 5.3: The mechanosensory system of bone according to Burger [9].

carry out remodelling calculations for whole bones unless there are significant advances in computing capacity, or unless a way can be found to scale these cellular processes onto a continuum level.

5.3 Stress Based and Strain Based Damage

Even though in a linear elastic material stress and strain are directly proportional, the tensor nature of this relationship prohibits one from viewing a stress- based algorithm as being equivalent to a strain based algorithm. As an example of how both algorithms could possibly give different solutions for a damaged material, consider the case of a uniaxial stress state $\boldsymbol{\sigma}$ acting on an isotropic material of elastic modulus E and Poisson's ratio ν. The stress tensor without the shear components (which are all zero) for this material is

$$\boldsymbol{\sigma} = \begin{pmatrix} \sigma_0 \\ 0 \\ 0 \end{pmatrix}$$

where $\sigma_0 < 0$ for compression, and the strain is given by

$$\epsilon = \begin{pmatrix} E\sigma_0 \\ -\nu E\sigma_0 \\ -\nu E\sigma_0 \end{pmatrix}$$

(see Figure 5.4). If it is now assumed that this material contains spherical microvoids which are susceptible to enlargement (ie. the material follows the laws of damage mechanics), then it is quite clear that the damage cannot be represented accurately by the stress field: while the stress field is compressive everywhere and hence cannot cause an increase in damage [71], splitting perpendicular to the stress field will cause an increase in damage (see Figure 5.5). This splitting damage can only be characterised accurately if one uses a strain based damage formulation because it is caused by the positive transverse strains. As bone remodelling can be caused both by compressive and tensile stresses, it is not quite as critical that any model for it be based on strain, but if one wants to capture the contribution of the transverse Poisson effect on bone remodelling, it is necessary to implement a strain based algorithm. Such a model is described in the next Section.

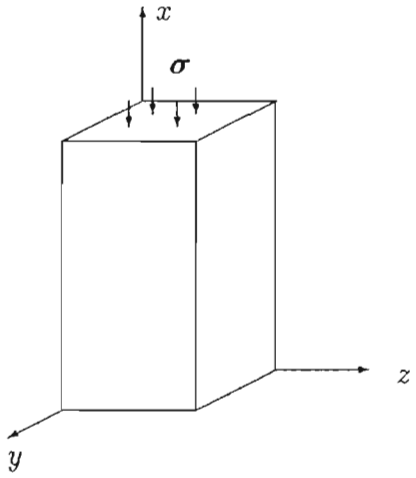

Figure 5.4: Uniaxial stress acting on an isotropic block of material.

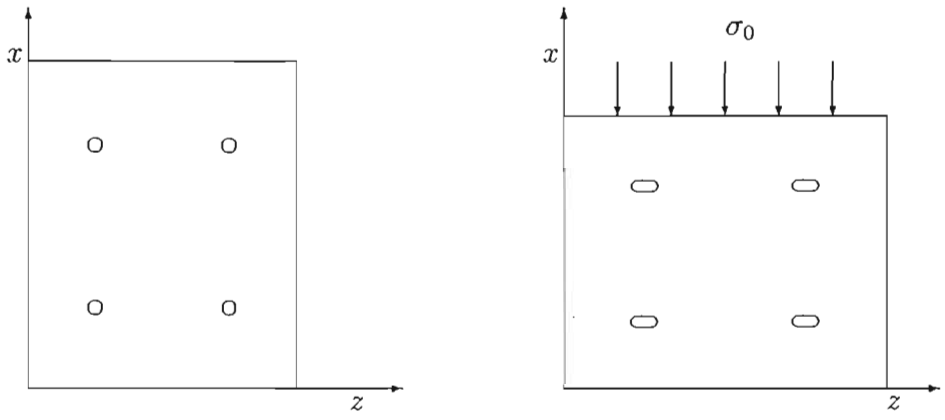

Figure 5.5: Splitting caused by Poisson strains in a damaged material under uniaxial stress.

5.4 A Strain Based Remodelling Algorithm

In the algorithm presented by Jacobs [47] which is used to solve the bone remodelling problem on the proximal femur (see Chapter 7 for results) and which is the starting point for this work, the remodelling stimulus was determined by the equivalent stress as given in equation (4.10) (see Section 4.2). This may be rewritten as

$$\bar{\sigma} = \sqrt{EC\epsilon \cdot \epsilon} \tag{5.1}$$

since $U = \frac{1}{2}\sigma \cdot \epsilon$ and for a linear elastic material $\sigma = C\epsilon$. The constant E is the elastic modulus of the isotropic bone continuum and C is the rank 4 elasticity tensor, which for an isotropic material is a function of E and Poisson's ratio ν. Hence this formulation also uses the strain as a remodelling criterion, but what prevents it from being a purely strain based approach is the dependence on E and C, which also depends on E. In this model, E is a function of density, and as the density varies throughout the model, equivalent strains in different parts of the domain can lead to a different value of the remodelling stimulus. A difficulty in applying this strain energy based algorithm is finding a reference value for the daily strain energy absorbed by bone during normal loading. Beaupré et al. [7] have used a homeostatic equilibrium stress stimulus of ψ_i^* of 50 MPa/day . Whether this corresponds to a physiological value is debatable.

5.4.1 Physiological determination of parameters

In a purely strain based model there is no problem in finding the parameters necessary to simulate a physiological situation. Martin and Burr [37] have summarised experimental findings of remodelling constants neatly (see Figure 5.6). From this diagram, it is easy to determine the remodelling equilibrium strain as the strain central to the physiological loading zone, i.e. at about $\epsilon_{rem} = 0.0015$. If the strain falls into the physiological zone then it is sufficient to sustain bone mass via the normal physiological functions of remodelling and bone turnover. In the trivial loading zone, the strain is not enough to maintain bone mass, and resorption occurs. In the overload zone, the remodeling stimulus is sufficient for bone apposition to occur. These ideas have been implemented in a manner similar to that employed by Beaupré [6] and Jacobs [47] for the strain energy based case; however, because this algorithm is strain based, the implementation is somewhat simpler.

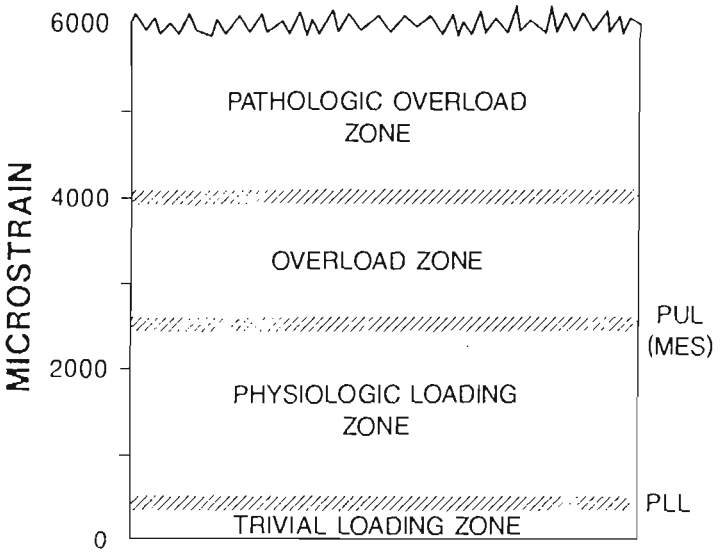

Figure 5.6: Regions of physiological and unphysiological strain values as taken from Martin and Burr [37].

5.4.2 Continuum and tissue level

The first simplification occurs when converting from the tissue level to the continuum level. Even though the stress is different on these two levels, the strain remains the same (see Figure 5.7): Let F be the force applied to a surface of area A of a cube of trabecular bone material. Assume that the total area of actual bone matrix is given by $a < A$. Then the compressive stress σ_c is given by

$$\sigma_c = \frac{F}{A}.$$

The tissue level stress σ_t is larger as F acts on a smaller area, and

$$\sigma_t = \frac{F}{a}.$$

The tissue surface area is a function of the relative density $\rho/\hat{\rho}$ and the cube surface area A (see Martin [59]), in particular

$$a = f\left(\frac{\rho}{\hat{\rho}}\right) A.$$

Hence the tissue level stress and the continuum level stress are linked as

$$\sigma_t = f\left(\frac{\rho}{\hat{\rho}}\right) \sigma.$$

Hence the stress is different on a continuum level than it is in the actual tissue. However, in this study it is assumed that

$$\begin{aligned} \boldsymbol{\sigma} &= E\epsilon \\ \boldsymbol{\sigma}_t &= E_t\epsilon; \end{aligned} \tag{5.2}$$

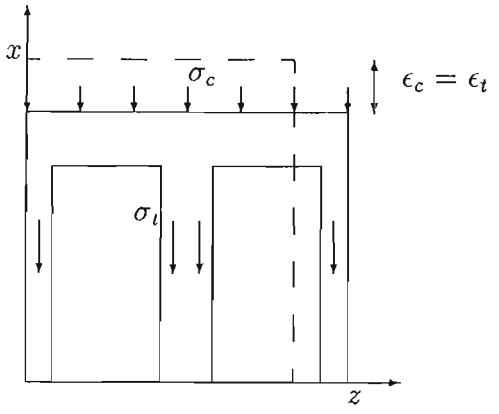

Figure 5.7: Stress and strain at the tissue and continuum levels.

the strain measured on a continuum level is the same that is measured on a tissue level. The density dependence lies in the elastic modulus E, which is different on the continuum and tissue levels:

$$E_t = \left(\frac{\rho}{\hat{\rho}}\right)^2 E,$$

as discussed by Gibson [34]. This is consistent with the continuum-tissue scaling adopted by Jacobs [47] which is

$$f\left(\frac{\rho}{\hat{\rho}}\right) = \left(\frac{\rho}{\hat{\rho}}\right)^2$$

(see equation (4.12)). Thus the remodelling error can be determined by using

$$e = n^{1/m}(\bar{\epsilon} - \epsilon_{rem}). \tag{5.3}$$

This is true only to a first approximation, however, since Gibson et al. [2] have shown that for a cellular material like bone, compressive strain on a structural level is converted into a combination of bending strain and axial strain on a tissue level. Van Rietbergen et al. [75] have confirmed this in their numerical simulations of single trabecular structures. To quantify this conversion is beyond the scope of the current work, hence the strain here will be regarded as equal on a continuum and on a tissue level. The strain stimulus $\bar{\epsilon}$ in this work is defined by

$$\bar{\epsilon} = \sqrt{\epsilon_1^2 + \epsilon_2^2 + \epsilon_3^2}, \tag{5.4}$$

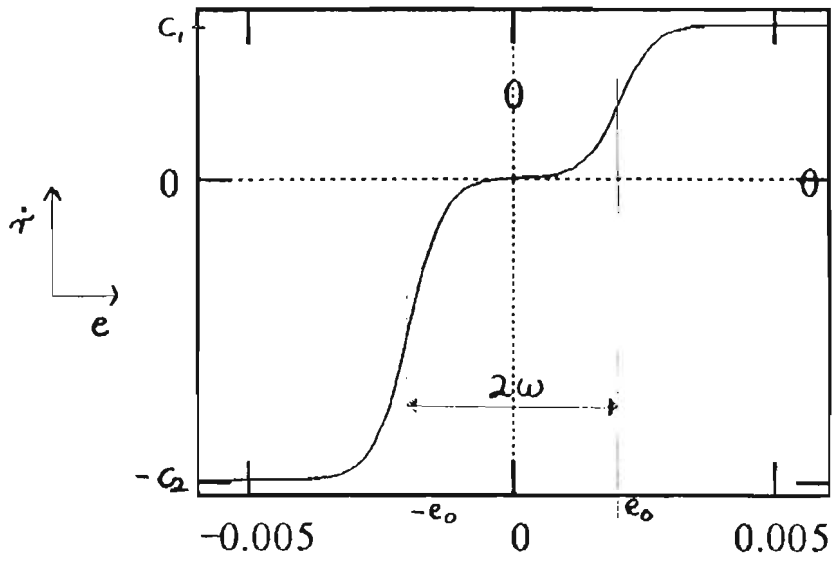

Figure 5.8: Relationship between the remodelling surface velocity $\dot{r}$ and the remodelling error e: a double sigmoid function. In this case, $e_0 = w$ and $\gamma = 6/\omega$.

where ϵ_i $(i = 1, 2, 3)$ are the eigenvalues of the strain tensor; thus both the maximal principal strain as well as the Poisson strains in the other directions are taken into account. The constants n and m are particular to each load case and are the same as in box 4.2. The load cases are applied sequentially, one per iteration, as for the strain energy based model (see Section 4.5

5.4.3 Remodelling surface velocity

In the SE algorithm, the remodelling surface velocity was given as a linear function of the remodelling error with or without a dead zone. What this means is that the larger the remodelling error, the larger the rate of surface deposition or surface resorption. However, physiological remodelling surface velocities are given as $2 - 40\,\mu m/day$ for resorption [37] and $1 - 2\,\mu m/day$ for formation [63]. Thus it is highly unphysiological to model the surface remodelling velocity as increasing indefinitely with the error e. It is acceptable to assume a linear $\dot{r} - e$ relation as long as the remodelling error is small, but there is no reason to assume that this is the case in the simulation of the proximal femur.

A more physiologically reasonable relation between $\dot{r}$ and e is a double sigmoid as shown in Figure 5.8. This approach caters both for a physiologically homeostatic region in case the remodelling error is small, and a stable surface apposition or resorption rate in case the remodelling error is very large. Also, if e falls in the region of trivial loading or the overload region (see Figure 5.6) then $\dot{r}$ increases or decreases almost linearly with e. This

curve is described mathematically by

$$\dot{r}(e) = \begin{cases} c_1/(1+\exp[-\gamma(e-e_0)]) & e > 0 \\ 0 & e = 0 \\ -c_2/(1+\exp[-\gamma(-e-e_0)]) & e < 0 \end{cases} .$$

The slope at $e = e_0$ is given by $d\dot{r}/de|_{e_0} = \gamma/4$. For a physiological zone width of w and a remodelling zone width of the same size (see Figure 5.6), parameters $e_0 = w$ and $\gamma = 6/w$ can be used, and then the parameters c_1 and c_2 are the respective maximum apposition and resorption velocities, in $\mu m/day$. These three parameters describe the double sigmoid curve completely. The linear form with the dead zone employed by Jacobs [47] required five parameters for a full description. The strain based remodelling algorithm is summarised in Box 5.1.

The parameters used are similar to those used in the SE algorithm except for those related to the strain based remodelling features of the algorithm. As before, ρ_{crit} represents the bone density at which the dependence of elastic modulus E on density changes from $E = a\rho^\gamma$ ($\rho < \rho_{crit}$) to $E = b\rho^\beta$ ($\rho \geq \rho_{crit}$). Also, the value of Poisson's ratio changes at this density (see Box 5.1.). As before, m is an empirically determined constant that can take any value between 3 and 8 and is assigned a value of $m = 4$ as in Carter et al. [13]. The values assigned to all the parameters are given in Box 5.2.

The parameters c_1, c_2 and n were varied in the different analyses carried out. Details are provided in Chapter 7. This algorithm was constructed with a view to removing some of the shortcomings of the SE algorithm, and in the hope of improving on the results gained using the SE algorithm. It will be seen that these results do represent an improvement, but they also have a few shortcomings. Further improvement can be achieved by applying the model to the physiologically more realistic three-dimensional domain. finite element mesh. This is the subject of Chapter 6.

Box 5.1: Isotropic Strain Based Bone Remodelling Algorithm

For each Gauss point, one state variable is needed: density ρ.

Given $\boldsymbol{\epsilon}_n$, $\Delta\boldsymbol{\epsilon}_n$, $\boldsymbol{\sigma}_n$, ρ_n:

Calculate $\bar{\epsilon} = \sqrt{\epsilon_1^2 + \epsilon_2^2 + \epsilon_3^2}$

Calculate $e = n^{1/m}(\bar{\epsilon} - \epsilon_{rem})$

Calculate $\dot{r} = \begin{cases} c_1/\left(1 + \exp\left[-\gamma(e - e_0)\right]\right) & e > 0 \\ 0 & e = 0 \\ -c_2/\left(1 + \exp\left[-\gamma(-e - e_0)\right]\right) & e < 0 \end{cases}$

This is how the double sigmoid is utilized;

Calculate $\hat{p} = 1 - \frac{\rho_n}{\hat{\rho}}$

$S_V = 0.03226\hat{p} - 0.09394\hat{p}^2 + 0.13396\hat{p}^3 - 0.10104\hat{p}^4 + 0.02876\hat{p}^5$

Calculate $\dot{\rho}_n = \hat{\rho}_n S_V \dot{r}$

Calculate $\rho_{n+1} = \rho_n + \Delta t \dot{\rho}_n$

Check whether $\rho_{min} \leq \rho_{n+1} \leq \hat{\rho}$

Update E, ν, λ, μ:

$E = \begin{cases} a\rho_{n+1}^{\alpha} & \rho_{n+1} \leq \rho_{crit} \\ b\rho_{n+1}^{\beta} & \rho_{n+1} > \rho_{crit} \end{cases}$

$\nu = \begin{cases} \nu_1 & \rho_{n+1} \leq \rho_{crit} \\ \nu_2 & \rho_{n+1} > \rho_{crit} \end{cases}$

$\lambda = \frac{E\nu}{(1+\nu)(1-2\nu)}$

$\mu = \frac{E}{2(1+\nu)}$

Update $\boldsymbol{C}_{n+1}$:

$$\boldsymbol{C}_{n+1} = \begin{pmatrix} \lambda + 2\mu & \lambda & 0 \\ \lambda & \lambda + 2\mu & 0 \\ 0 & 0 & \mu \end{pmatrix}$$

Update strain and stress:

$\boldsymbol{\epsilon}_{n+1} = \boldsymbol{\epsilon}_n + \Delta\boldsymbol{\epsilon}$

$\boldsymbol{\sigma}_{n+1} = \boldsymbol{C}_{n+1}\boldsymbol{\epsilon}_{n+1}$

Box 5.2.: Parameters Required for Isotropic Strain Based Bone Remodelling Algorithm

$\rho_{min} = 0.05 g/cm^3$	$e_0 = w = 0.002$	$\alpha = 2.5$
$\rho_{crit} = 1.2 g/cm^3$	$\gamma = 6/w = 3000$	$\beta = 3.23$
$\rho_{cort} = 1.92 g/cm^3$	$\nu_1 = 0.25$	$a = 2014$
$m = 4$	$\nu_2 = 0.32$	$b = 1763$

Chapter 6

Extending the Analysis to 3D

The complex and fully three-dimensional geometry of the human femur is complemented by non-symmetric loading that is also three-dimensional. Problems experienced with the two-dimensional mesh include the fact that an equilibrium solution is never reached (see Chapter 7). The lack of equilibrium may be due to the fact that essential features of the behaviour of the femur are lost in the restriction to two dimensions. This Chapter is concerned with setting up a three-dimensional finite element model of the human femur.

6.1 3D Meshing of the Femoral Head

The idea of meshing the intact femur in three dimensions is not new, and examples of such meshes in the literature include Huiskes [42] and Poss et al. [67]. However, no bone remodelling analyses were carried out on these meshes. Huiskes et al. have simulated bone remodelling around implants, but not on intact whole bones [40] [42] [44]. Meshing a three-dimensional model of the femur and subjecting this to a full remodelling analysis will carry further the work already done on two-dimensional bone models [13] [47]. As the remodelling algorithms described in Chapters 4 and 5 are written in such a way as to be applicable also to a three-dimensional isotropic material, the only difficulty in carrying out a fully three-dimensional analysis lies in generating the finite element mesh.

The first step towards creating such a mesh is the analysis of a set of cross-sectional scans of an actual human femur that were produced using a CT-scan methodology. These were taken at intervals of 4mm along the femoral head and 8mm along the femoral shaft where the cross-sectional profile is almost constant as z varies (see Figure 6.1).

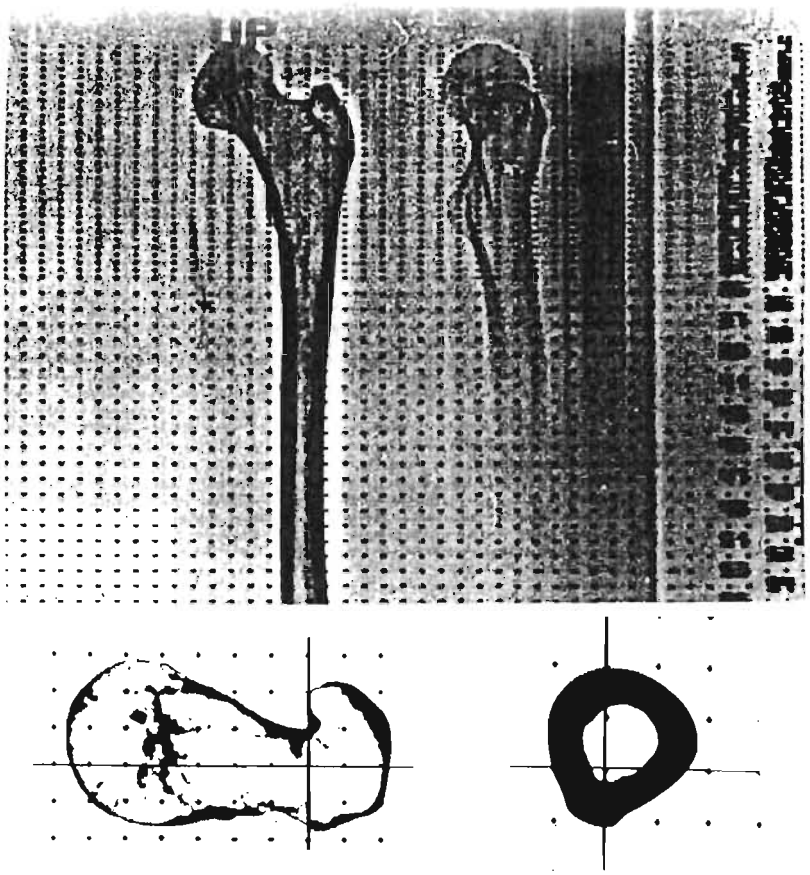

Figure 6.1: CT-scan of an intact femur with cross-sections.

What is needed to generate the mesh are contours of the inner and the outer cortex so that one can draw a clear distinction between cortical bone and cancellous bone and obtain a boundary for the model. These contour maps were created using the CORELDRAW software. Each cross-section was assigned its correct z-position and then imported into the ABAQUS-PRE processing package as a set of points. Each cross-section also contained some reference points which were used to line up all the cross-sections correctly, thus compensating for any translations or rotations that might have occurred when the sections were originally scanned into CORELDRAW using a small hand-held scanner. Once all the sections were imported and lined up, the points were joined by curves, the curves by surfaces and the surfaces by solids. The solids could then be used as a framework to generate finite elements.

The mesh consists of two different kinds of finite elements, namely eight-noded trilinear brick elements and six-noded linear wedge elements (see Figure 6.2). The use of higher order elements was impossible as this would have meant prohibitive computational effort on the machines available (IBM RISC-390). A full analysis with this mesh of just over 6000 elements took about eight hours of CPU time, but as the machine was used simultaneously for other purposes as well, the job took almost a week to complete.

As the cross-sections of the femur change shape along the z-axis, various methods of

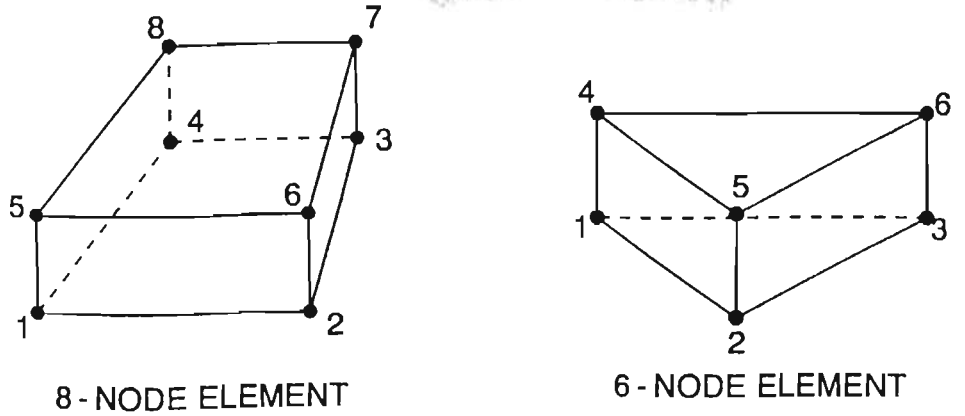

Figure 6.2: Finite elements used in the 3D mesh: 8-noded brick and 6-noded wedge.

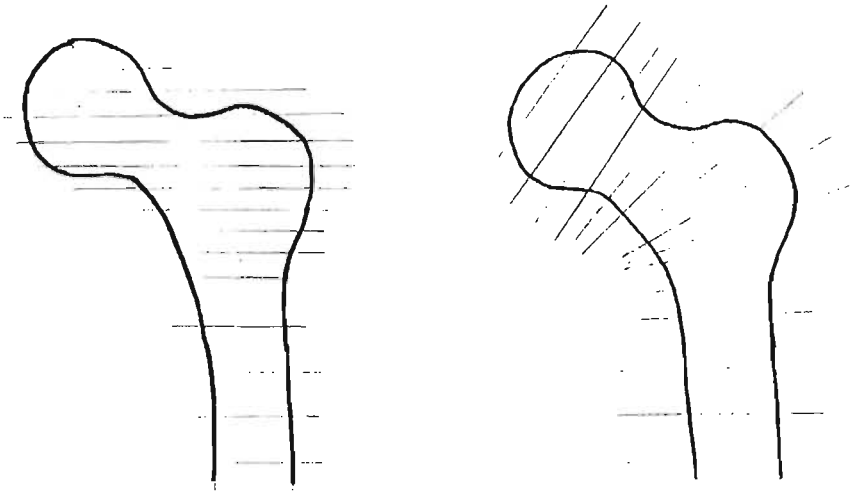

Figure 6.3: An alternative method of taking cross-section where the plane sections in the femoral head have different orientations.

meshing have to be employed in different regions of the model. The most important criterion when meshing is that no nodes lie in contact with the surface of another element, ie. all nodes of adjacent elements are matched up. Also, as few wedge elements as possible were used.

Two major problems with the overall shape of the mesh were the fact that the cortex thins considerably in the femoral head, and also at the base of the femoral head there is a sudden widening of the stem which is difficult to mesh. The mesh was constructed in such a way as to avoid angles of more than 135^o and less than 45^o in 8-noded elements, and also to avoid the ratios of adjacent side lengths much larger than 5, i.e. the distortion of individual elements was kept to a minimum. Inevitably there are some elements that are badly distorted, and also the volume of some elements (eg at the base of the femoral head) is much larger than the volume of others. One way to remedy this would be to change the orientation along which the cross-sections are taken (see Figure 6.3), but in this work this was not feasible as all sections in the original CT-scan were taken along the z-axis.

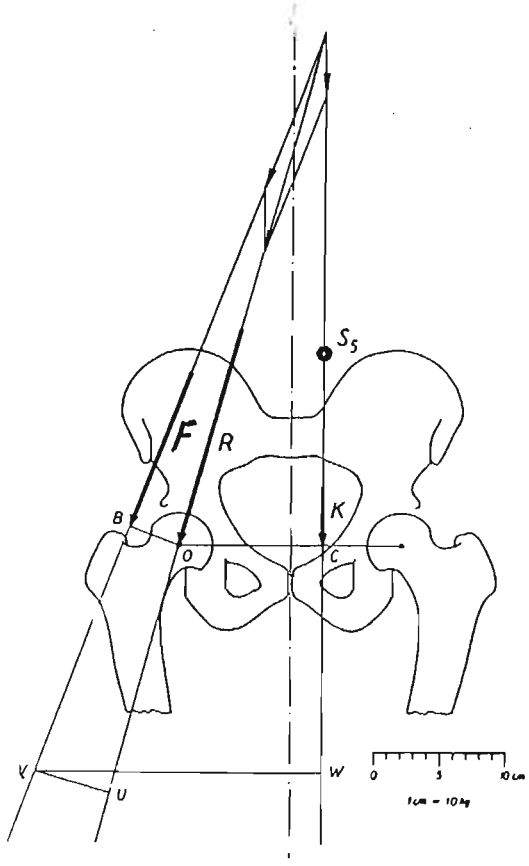

Figure 6.4: Balance of the Pelvis during Single-Legged Stance.

6.2 Loading Conditions: Pelvic Balance

Once the finite element mesh is completed, the next step is to prescribe the loading and boundary conditions suitable to the problem. As observed earlier, the geometry of the system is very complex and the loading conditions are highly nonuniform: there are more than twenty muscles attached in different places to the proximal femur [32]. The simplest sort of loading that one finds in the literature is that applied during single-legged stance [64] or during the single-legged stance phase of gait [13] [47]. In this case, the only muscle that exerts any force on the femur is the hip abductor muscle which is attached to the greater trochanter. The body weight, the reaction force by the femoral head, and the force exerted by the hip abductor on the pelvis have to act in such a way that the pelvis remains in static equilibrium (see Figure 6.4).

According to Pauwels [64], the weight W_L of the swinging leg in single-legged stance is given by

$$W_L = 0.186 W_B, \tag{6.1}$$

where W_B is the bodyweight of the individual; thus, if W_B and the reaction force $\boldsymbol{R}$ exerted by the femoral head are given, one can calculate the balancing force $\boldsymbol{F}$ that the

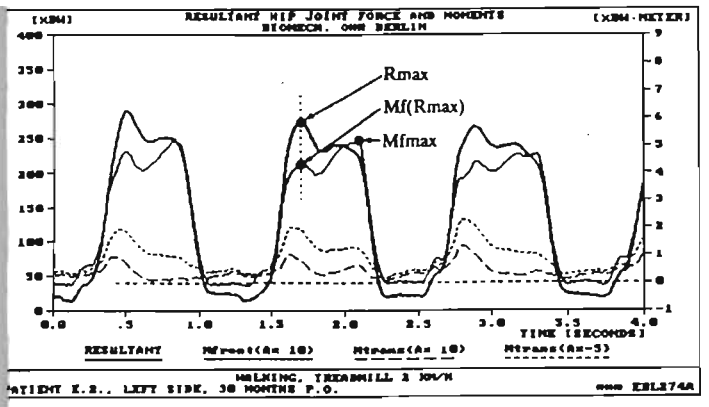

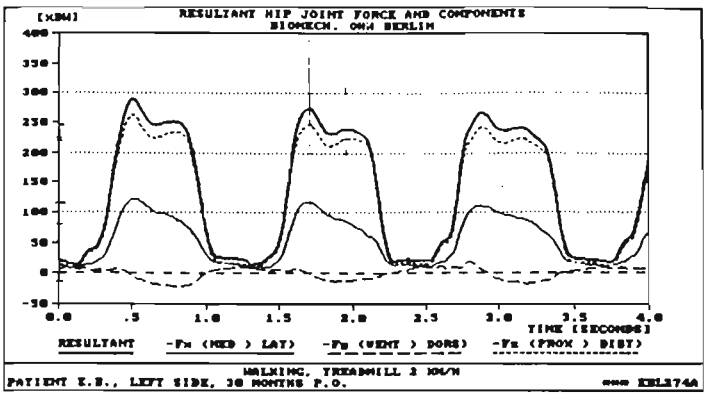

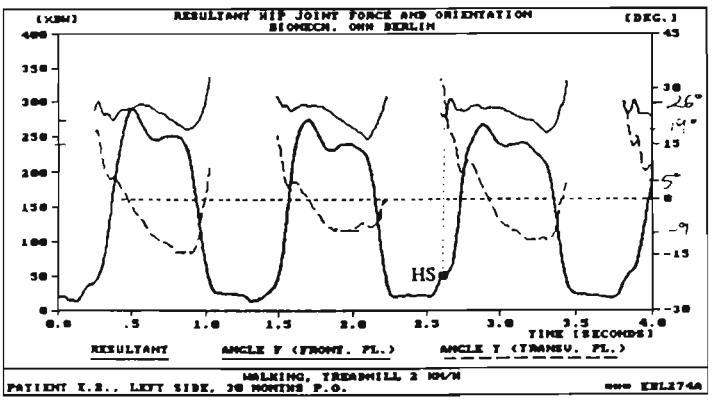

Figure 6.5: Gait cycle data by Bergmann et al.

hip abductor needs to exert in order to maintain equilibrium of the pelvis:

$$\sum \boldsymbol{F} = 0 \Rightarrow \begin{pmatrix} F_1 \\ F_2 \\ F_3 \end{pmatrix} + \begin{pmatrix} R_1 \\ R_2 \\ R_3 \end{pmatrix} + \begin{pmatrix} 0 \\ 0 \\ W_B - W_L \end{pmatrix} = 0 \tag{6.2}$$

Of course the pelvis is not strictly in static equilibrium during one-legged gait stance, but this is a first approximation. Making this assumption does not introduce as much uncertainty into the results as omitting all the other muscle groups does for instance, so in this case it is valid to assume equilibrium.

Bergmann et al. [8] have produced experimental data of the femoral head reaction force and the angle at which this acts during the whole gait cycle, and for all the three-dimensional simulations described in Chapter 7, two specific load cases were taken at two specific times in the gait cycle (see Figure 6.5). The measurements which Bergmann et al. produced had to be translated into the coordinate frame in which the 3D mesh was generated, and several coordinate transformations had to be made (see Figure 6.6). Details of the load cases and directions are given below. Note that the reaction force on the femoral head during single-legged stance is almost three times the bodyweight of the particular patient in which it was measured, i.e. six times the force exerted during normal two-legged standing. This proportion can increase to up to 5.84 times the body weight

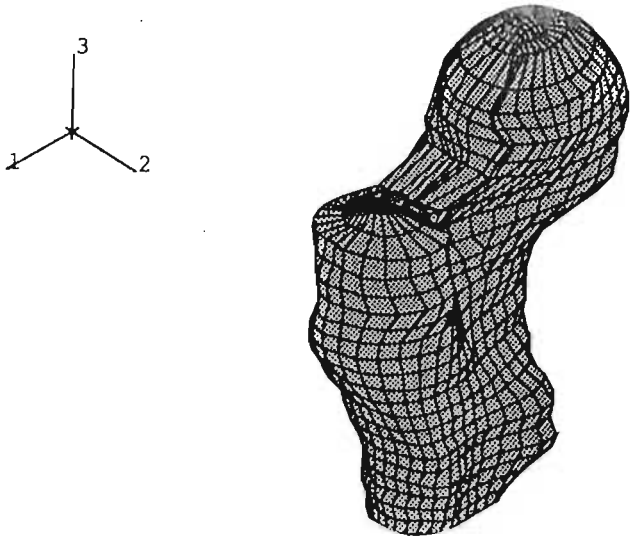

Figure 6.6: Coordinate System for the femoral head in which the loads are applied.

Table 1: Applied Load Cases

	LC_1	LC_2
R_x	-753	-586
R_y	-223	-117
R_z	1582	1435
$\|R\|$	1768	1554

when the patient jogs or runs, so it is evident that the proximal femur has to be able to withstand a substantial range of loads [8].

6.3 Application of the Loads: Concentrated vs Pressure Load

ABAQUS offers two forms of load application: pressure loads on an element surface, and nodal point loads. Both were used in simulating the three-dimensional bone remodelling situation. The drawback of the pressure load facility is that only constant pressures can be exerted on a given element face. More complicated pressure loads such as not linearly varying ones, for instance, require additional FORTRAN coding by the user. Applying concentrated nodal loads on any linear element, on the other hand, is quite straightforward. Any constant force that is applied to a particular element surface of an element with linear shape functions can be divided by four and then applied to each corner node as shown by Cook et al. [16]. If the constant force applied to the element of

area A_e with bilinear element shape functions $\hat{\phi}_i$ as given in equation (3.46) is $\boldsymbol{F}$, then the equivalent nodal load on node i can be calculated according to

$$\begin{aligned} \boldsymbol{F}_i &= \int_{A_e} \frac{\boldsymbol{F}}{A_e} \psi_i^{(e)} \, dA_e \\ &= \int_{\hat{A}} \frac{\boldsymbol{F}}{A_e} \hat{\phi}_i J \, d\xi d\eta. \end{aligned}$$

Here, $\hat{A}$ represents one surface of the three-dimensional master element $\hat{\Omega}$, and J is the determinant of the Jacobian used to transform the real element surface A_e onto the master element surface $\hat{A}$ (see equation (3.49)). In the simplest case, where the element surface concerned is a rectangle of area A_R, J is a constant of value $A_R/4$, and the integral reduces to

$$\boldsymbol{F}_i = \frac{\boldsymbol{F}}{A_e} \int_{\hat{A}} \tfrac{1}{4}(1 \pm \xi)(1 \pm \eta) J \, d\xi d\eta$$

for any particular shape function. This can be evaluated as

$$\boldsymbol{F}_i = \frac{\boldsymbol{F}}{4} \int_{-1}^{1} \int_{-1}^{1} \tfrac{1}{4} \, d\xi d\eta$$

when one considers that the integral of any odd function such as $\int_{-1}^{1} \xi \, d\xi$ vanishes.

This is only true when the element surface concerned is rectangular. As none of the element surfaces on the femoral head deviate significantly from a rectangular shape, the Jacobian is approximated as being constant and having a value of $A_e/4$ on all element surfaces; thus the equivalent nodal load at any of the nodes is given by

$$\boldsymbol{F}_{eq} = \frac{\boldsymbol{F}}{4}. \tag{6.3}$$

Note that contributions from neighbouring elements at a common node have to be added together. The equivalent nodal loads on a patch of four element surfaces that have a force $\boldsymbol{F}$ applied respectively would then look as in Figure 6.7. For applying a concentrated force $\boldsymbol{F}$ to a patch of element surfaces of total surface area A_{tot}, one uses the following formula to calculate the force $\boldsymbol{F}_e$ applied to element surface e with area A_e:

$$\boldsymbol{F}_e = \frac{\boldsymbol{F}}{A_{tot}} \cdot A_e \tag{6.4}$$

This methodology is used in applying the force applied by the hip abductor muscle to the greater trochanter.

In applying the force that the acetabulum (the pelvic socket for the femoral head) exerts on the femoral head, this procedure can also be followed. The results of this approach are

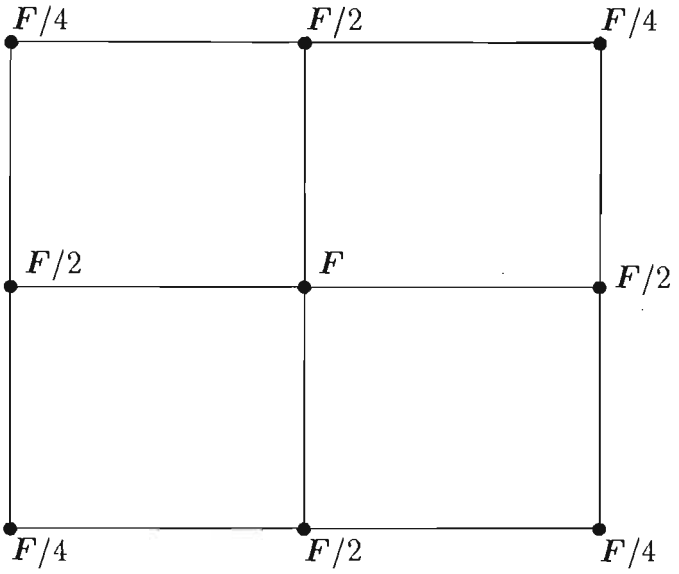

Figure 6.7: Equivalent Nodal Loads applied to a patch of element surfaces each having a force F applied to them.

shown in Section 7.2 One complication is that the loading which the acetabulum exerts on the femoral head spans almost 180^o in all directions. Thus the assumption that it can be represented by a constant force on all element surfaces is incorrect: the elements experience a decreasing force/unit area as $\theta \rightarrow 90^o$ (see Figure 1.4).

Also, there are quite a large number of element surfaces that fall within the acetabulum. To set up a spreadsheet to calculate all the equivalent nodal loads, including compensations for decreasing loads towards the edges, would be quite time-consuming. Another method of applying loading on the femoral head would be to model the acetabulum as a rigid surface in contact with the proximal femur, and then to apply the forces measured by Bergmann et al. [8] on this rigid surface. The computational effort that would be expended on a contact algorithm needed to simulate this accurately, however, is prohibitive. Hence the pressure load option as outlined above was utilised. According to Li et al. [55], the articular joint contact pressure as a function of angle is a curve that can be approximated by a parabola (see Figure 6.8). Using this approximation, the pressure on each relevant element surface can be computed as follows: given

$$P(\phi) = -P_0 \left(\frac{2}{\pi}\right)^2 \left(\phi^2 - \left(\frac{\pi}{2}\right)^2\right) \tag{6.5}$$

in a polar coordinate system as shown in Figure 6.9,

$$dF = P(\phi)dA$$

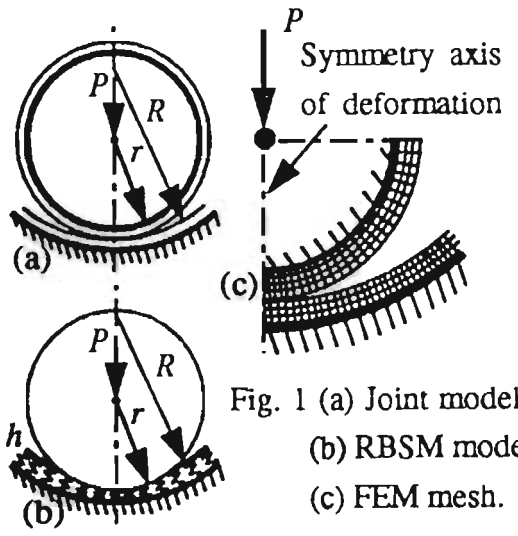

Fig. 1 (a) Joint model;
(b) RBSM model;
(c) FEM mesh.

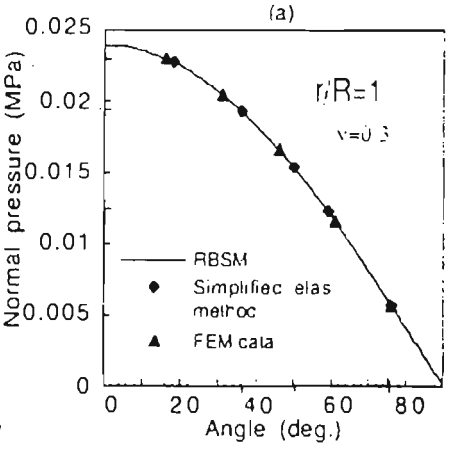

Figure 6.8: Pressure Distribution as a Function of Angle for the Hip Joint, Taken from Li et al.

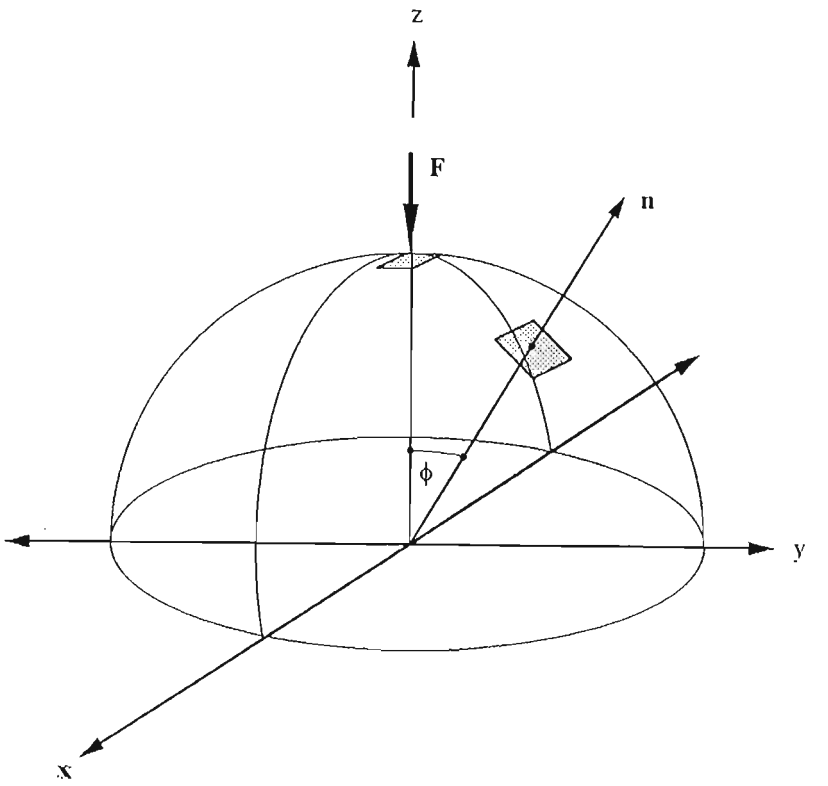

Figure 6.9: 3D coordinate system for femoral head hemisphere.

$$
\begin{aligned}
&= P(\phi)\boldsymbol{n}dA \\
&= P(\phi)\begin{pmatrix} \sin\phi\cos\theta \\ \sin\phi\sin\theta \\ \cos\phi \end{pmatrix} dA \qquad (6.6)
\end{aligned}
$$

with $dA = r^2 \sin\phi d\phi d\theta$ the element of surface area. Integrating over the femoral head hemisphere, one obtains

$$
\begin{aligned}
\mathbf{F} &= \begin{pmatrix} 0 \\ 0 \\ F_0 \end{pmatrix} \\
&= \int_0^{2\pi}\int_0^{\frac{\pi}{2}} -P_0\left(\frac{2}{\pi}\right)^2\left(\phi^2 - (\frac{\pi}{2})^2\right)\begin{pmatrix} \sin\phi\cos\theta \\ \sin\phi\sin\theta \\ \cos\phi \end{pmatrix} r^2\sin\phi d\phi d\theta \\
&= \begin{pmatrix} 0 \\ 0 \\ P_0\frac{r^2}{\pi}\left(\frac{\pi^2}{2}+2\right) \end{pmatrix},
\end{aligned}
$$

which gives

$$
P_0 = \frac{\pi F_0}{r^2(2+\frac{\pi^2}{2})}. \qquad (6.7)
$$

So a spreadsheet to calculate the pressure on each element surface can be set up quite easily once one has found the element surface that has a unit normal vector $\boldsymbol{n}_s$ closest to the unit normal $\boldsymbol{n}_F$ defining the applied force direction. The procedure used was as follows:

1. Find the central element using $min_{\text{all elements}}\{||\boldsymbol{n}_F - \boldsymbol{n}_s||\}$. For this element, $\phi = 0$.

2. For each adjoining element, calculate ϕ using the cosine rule

$$
\cos\theta = \frac{r_1^2 + r_2^2 - d^2}{2r_1r_2} \qquad (6.8)
$$

, where r_i is the distance from each element midpoint to the center of the femoral head, and d is the distance from the midpoint of element 1 to that of element 2 (see Figure 6.10).

3. Calculate $P(\phi)$ for each element and apply this using the ABAQUS pressure load option.

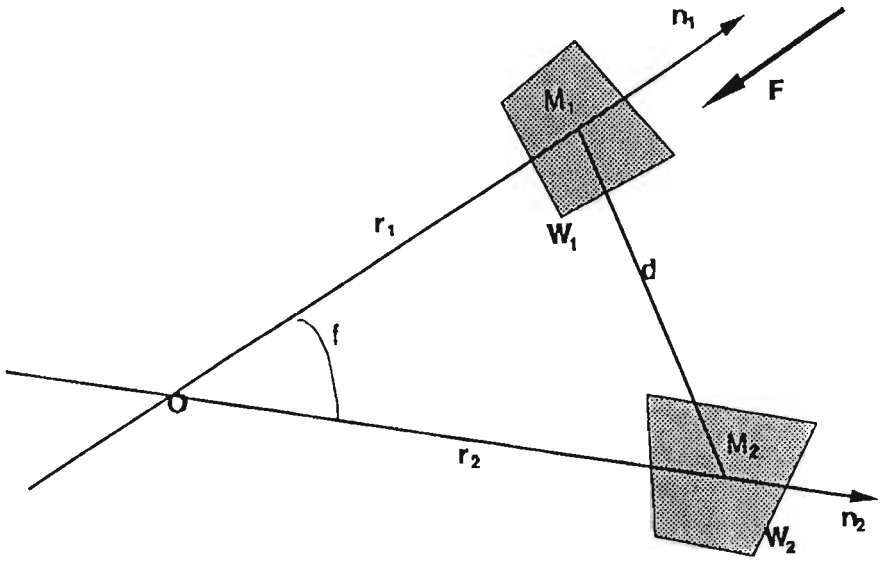

Figure 6.10: Determining the angle ϕ between the element with normal vector closest to the load direction and any other element.

For each different load case the origin and orientation of the coordinate system depicted above changes: it is centered around whatever element surface has a normal closest to the load direction. The area of each element surface was found using the vector product as shown in Figure 6.11 (see equation (2.7)), and the normal vector in each case was found in a similar fashion. Hence the parabolic pressure distribution in equation (6.5) is approximated by a piecewise constant pressure distribution with constant pressure over each element surface. This approximation is not accurate for large ϕ as the slope of the parabola shown in Figure 6.8 becomes very steep as $\phi \rightarrow 90°$. Also, the element surfaces are larger for large ϕ than for small ϕ because of the way the mesh is designed. These two inaccuracies add up to produce resultant forces which deviate slightly from the reaction force $\boldsymbol{R}$ (see equation (6.2)). To compensate and restore equilibrium, small concentrated nodal loads are applied to the topmost nodes of the femoral head in addition to the pressure loads applied to each surface. These were mostly in the x- and y- directions and quite small ($O(10N)$) and should not have a significant effect on the characterization of the parabolic pressure load that is applied *in vivo* by the acetabular socket on the femoral head.

6.4 Boundary Conditions

Boundary conditions are applied to the bottom layer of nodes of the femoral shaft. These consist of pinning some nodes in all three directions and constraining the rest to move in the x and y directions only (rolling boundary condition) (see Figure 6.12). Note that the femoral shaft has been designed to be long enough for significant bending to take place

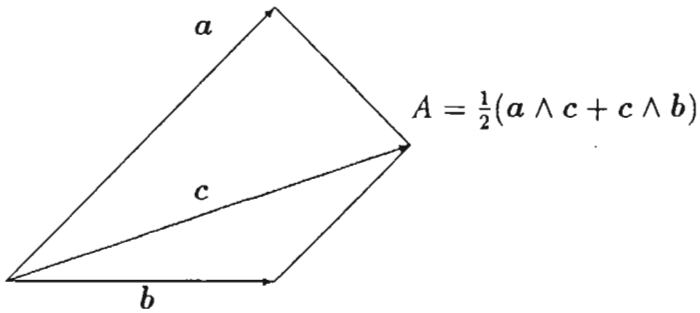

Figure 6.11: Surface area of a quadrilateral element surface.

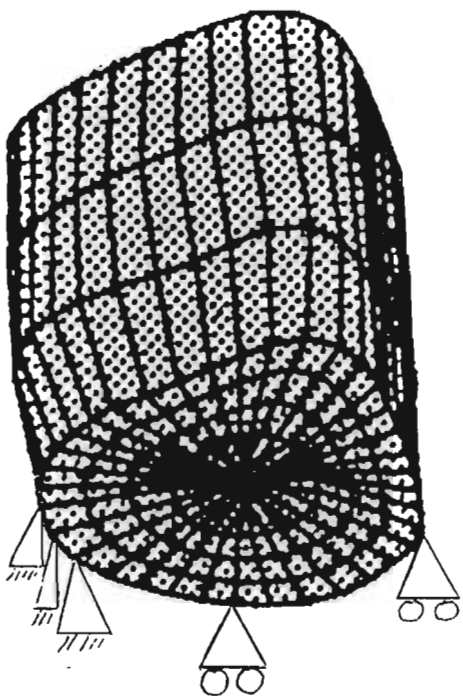

Figure 6.12: Boundary conditions on the bottom layer of nodes.

in the simulation (see Section 4.6). Hence the boundary is far away from the region of maximum bending stress.

Chapter 7

Results

This chapter contains results from all the analyses performed. Results are presented here and discussed in Chapter 8.

The results obtained from implementing the various algorithms can be put into two distinct categories: results obtained from a two-dimensional plane strain analysis and results obtained from a fully three-dimensional analysis. Since the two-dimensional plane strain problem has far fewer degrees of freedom than the fully three-dimensional one, computational effort for the two-dimensional problem is less and most of the analysis was carried out in two dimensions. Hence the UMAT algorithms were coded and tested in two dimensions, and various parametric studies were undertaken in two dimensions. All the experiments described in this chapter were carried out using the ABAQUS 5.3 finite element code on an IBM RISC-370 workstation or the ABAQUS 5.4 code on an IBM RISC-390. A typical two-dimensional run of 500 loading increments took about two hours to complete on the IBM RISC-370, whereas a three-dimensional analysis of 300 increments took about about eight hours of CPU time on the IBM RISC-390 platform. Some of the numerical analyses carried out include experiments on how the stress and strain distributions differ in a femur with a short stem (as used by Jacobs [47]) and a long stem, whether the same solution is reached in the long term with a different initial density distribution, how including a side plate to model the cylindrical cortex shell influences results, and whether the algorithm produced a stable solution in the long term. The effect of different surface remodelling velocities on density remodelling was also investigated in the strain based model. For this model, physiological values for remodelling surface velocities are known.

Results of these experiments are presented in the form of density contour plots on the

actual mesh as well as history plots of the density at Gauss points of strategically selected elements. Since one can see the physiological density distribution on radiographs of the femur (see Figure 4.6), density plots are an appropriate way of visualising results and comparing them with reality. The shape of the history curves indicate whether a solution is an equilibrium solution or whether the density is still evolving even after a long time of remodelling: if the slope of the density-time curve is flat, one can assume that the element undergoes no more density remodelling.

The results of the fully three-dimensional experiments also take the form of density contour plots and history plots of the density in strategically selected elements. An investigation of whether a distributed pressure load induces a remodelling pattern different from that caused by a concentrated load is included, and various physiological features that are reproduced by the finite element model are discussed.

7.1 Results of Two-Dimensional Implementations

This section consists of two subsections, both of which contain results from several finite element simulations. The first subsection summarises various remodelling analyses using the strain energy based algorithm developed by the Stanford group [47] (see Section 4.7). The second subsection contains results obtained by implementing the strain based algorithm described in Section 5.4.

7.1.1 Stanford model

Effect of a side plate. The first experiment conducted investigates the influence that a sideplate (described in Section 4.6) has on density remodelling. Results of this investigation are shown in Figure 7.1. The initial density of the whole front plate is $\rho_i = 0.5\, g/cm^3$ This run was carried out for 500 loading increments, and density distribution contours were generated after 20, 160, 300 and 500 iterations respectively. The density distribution shows that no cortical bone is formed in the region where the sideplate is attached. It was decided to perform all subsequent experiments without the use of a sideplate.

Effect of initial density. The following study was set up to investigate the dependence of density evolution on initial conditions. To do this, various runs with different initial density were set up and the density evolution of some strategically placed

elements was monitored using the *history option in ABAQUS Post (see Figure 7.2). The graphs in Figure 7.3 illustrate how the final density is affected by the initial density assigned to the elements that were monitored.

Density distribution after a large number of iterations. The final numerical experiment carried out using Jacobs's [47] material model was designed to quantify the long-term behaviour of the strain energy based algorithm. To do this, a run of 3000 iterations was conducted using an initial density of $\rho_i = 0.5\, g/cm^3$, and the results are captured in density contour plots (Figure 7.4) as well as history curves (Figure 7.5). The density distribution is given after 100, 1000, 2000 and 3000 iterations respectively in Figure 7.4.

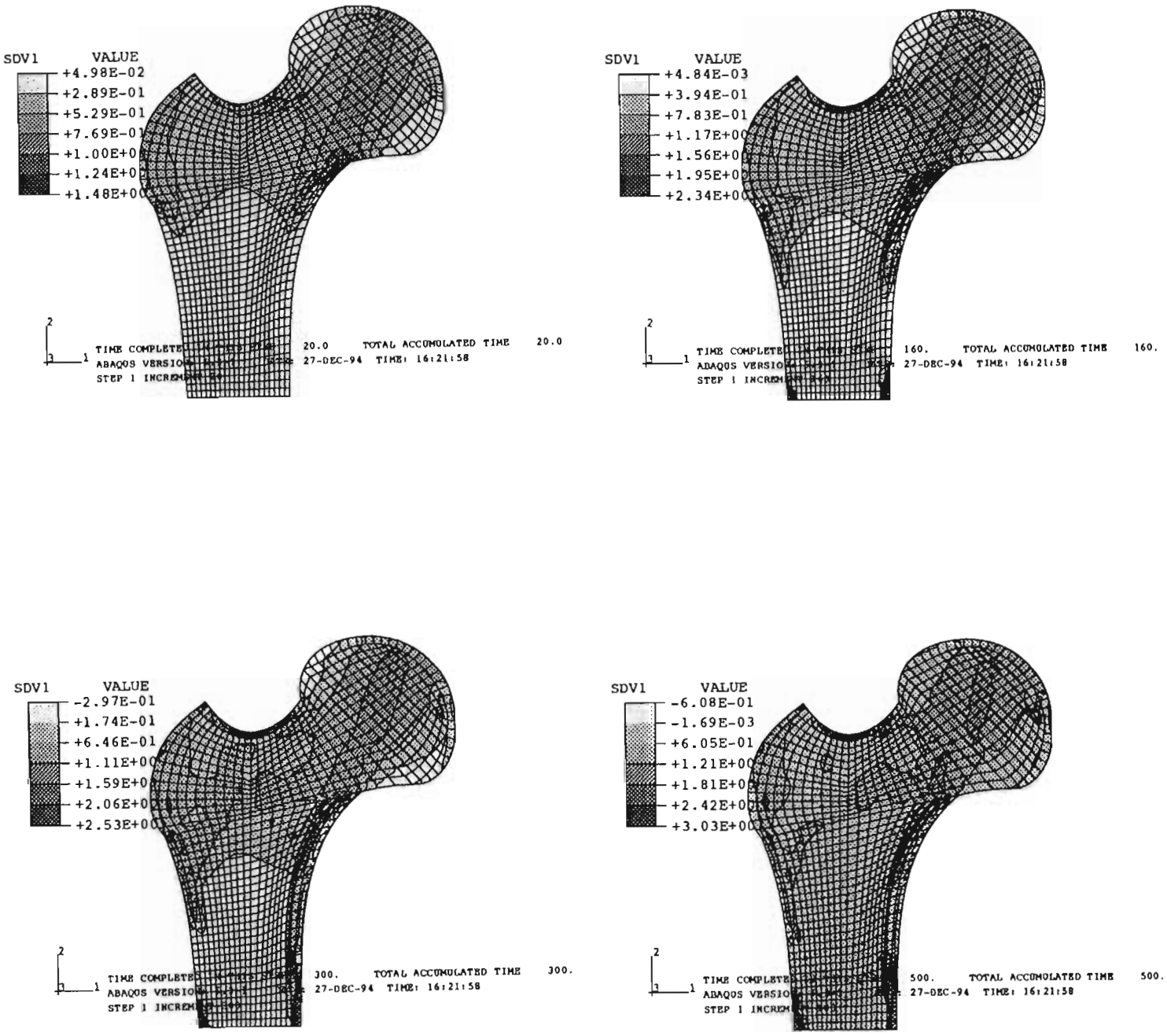

Figure 7.1: Experiment 1: Two-dimensional plane strain run with $\rho_i = 0.5\, g/cm^3$, including a side plate of cortical density which does not remodel.

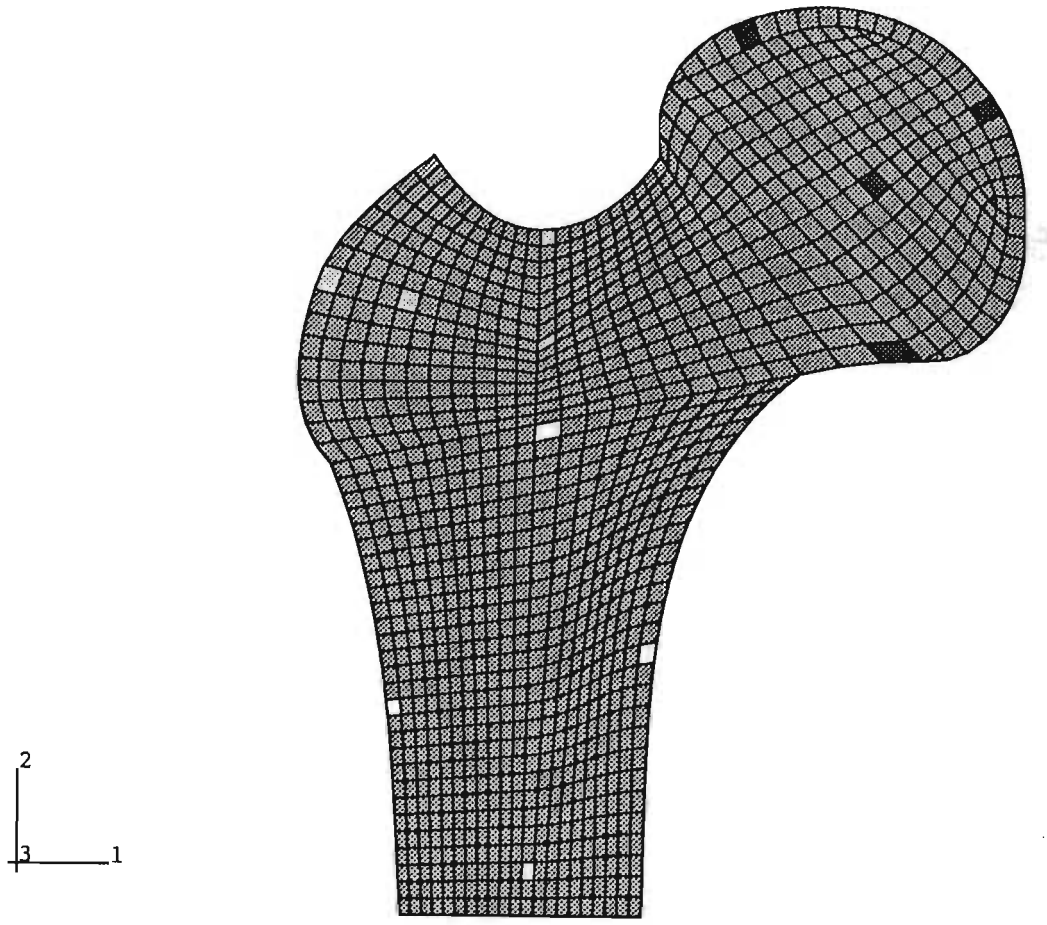

Figure 7.2: Mesh of the proximal femur showing which elements were monitored in the initial conditions experiments. The four black elements in the femoral head are numbered 1 to 4, the grey elements in the lateral part of the femur are numbered 5 to 8, and the white elements in the shaft are numbered 9 to 12.

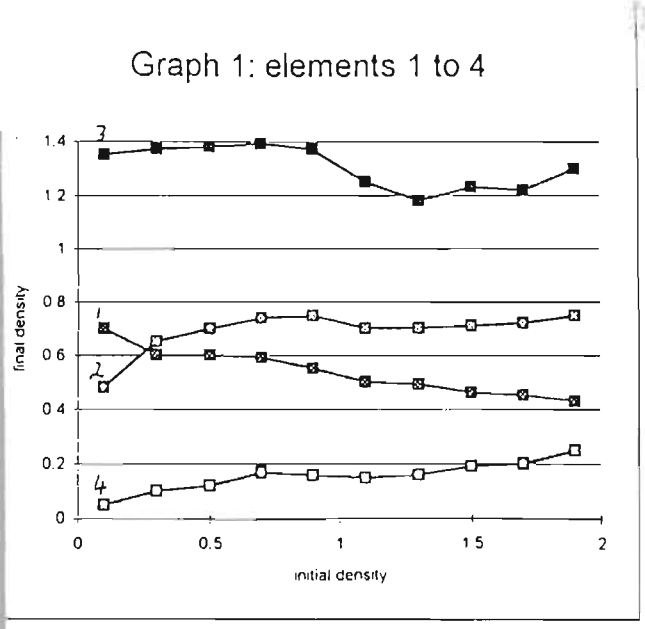

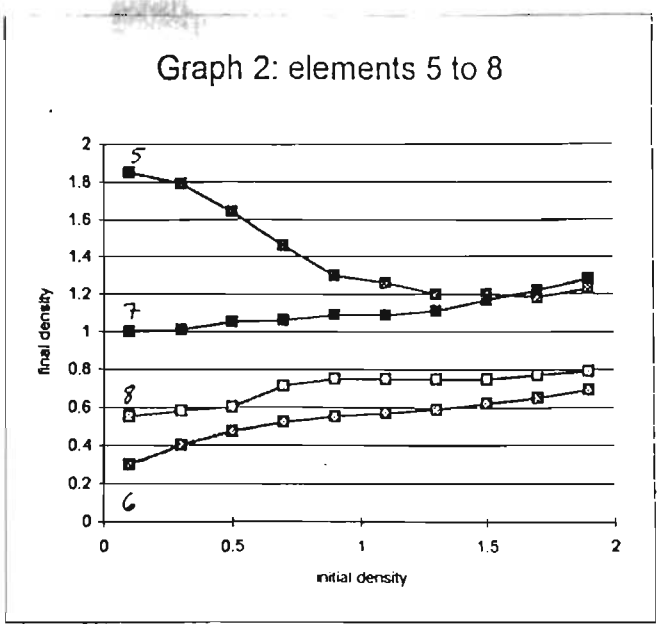

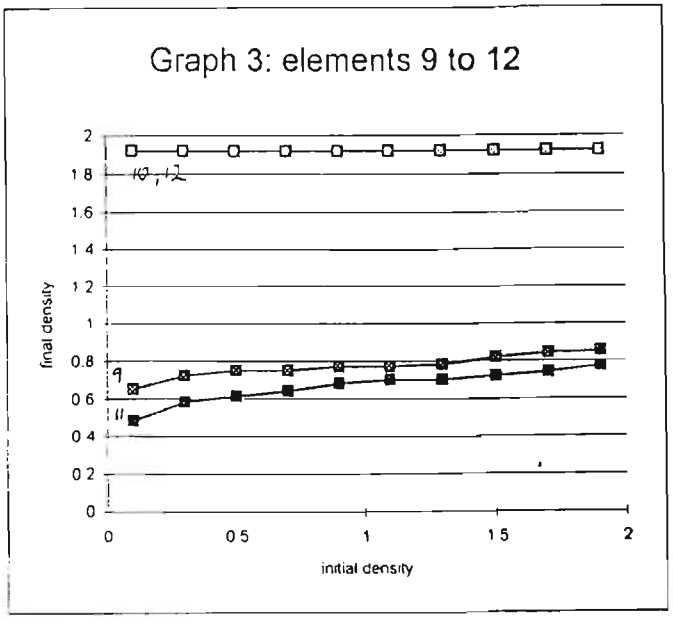

Figure 7.3: Graphs showing the final density as a function of initial density for twelve different elements.

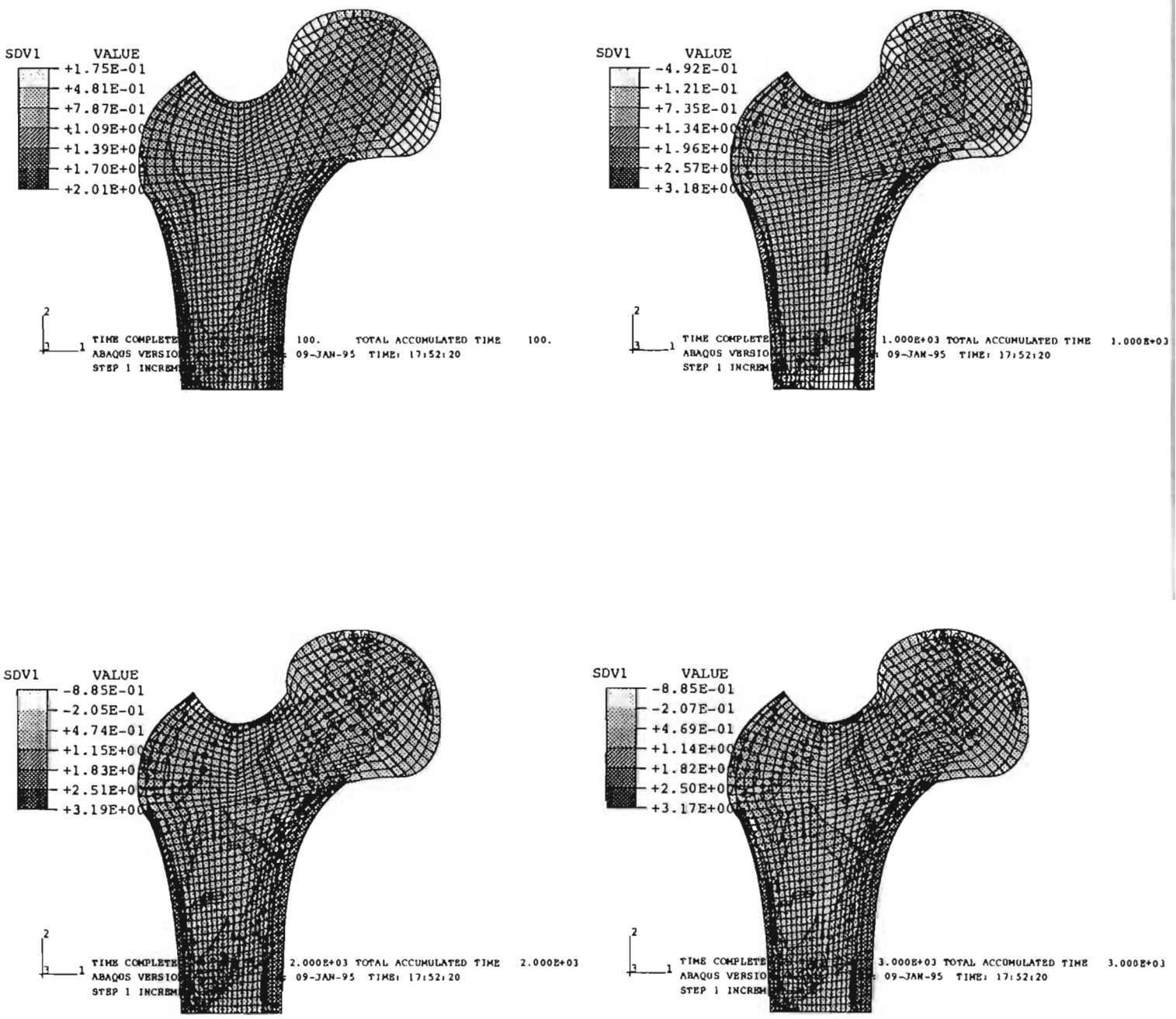

Figure 7.4: Density contour plot of long-term run; density contours are shown at 100, 1000, 2000 and 3000 increments respectively.

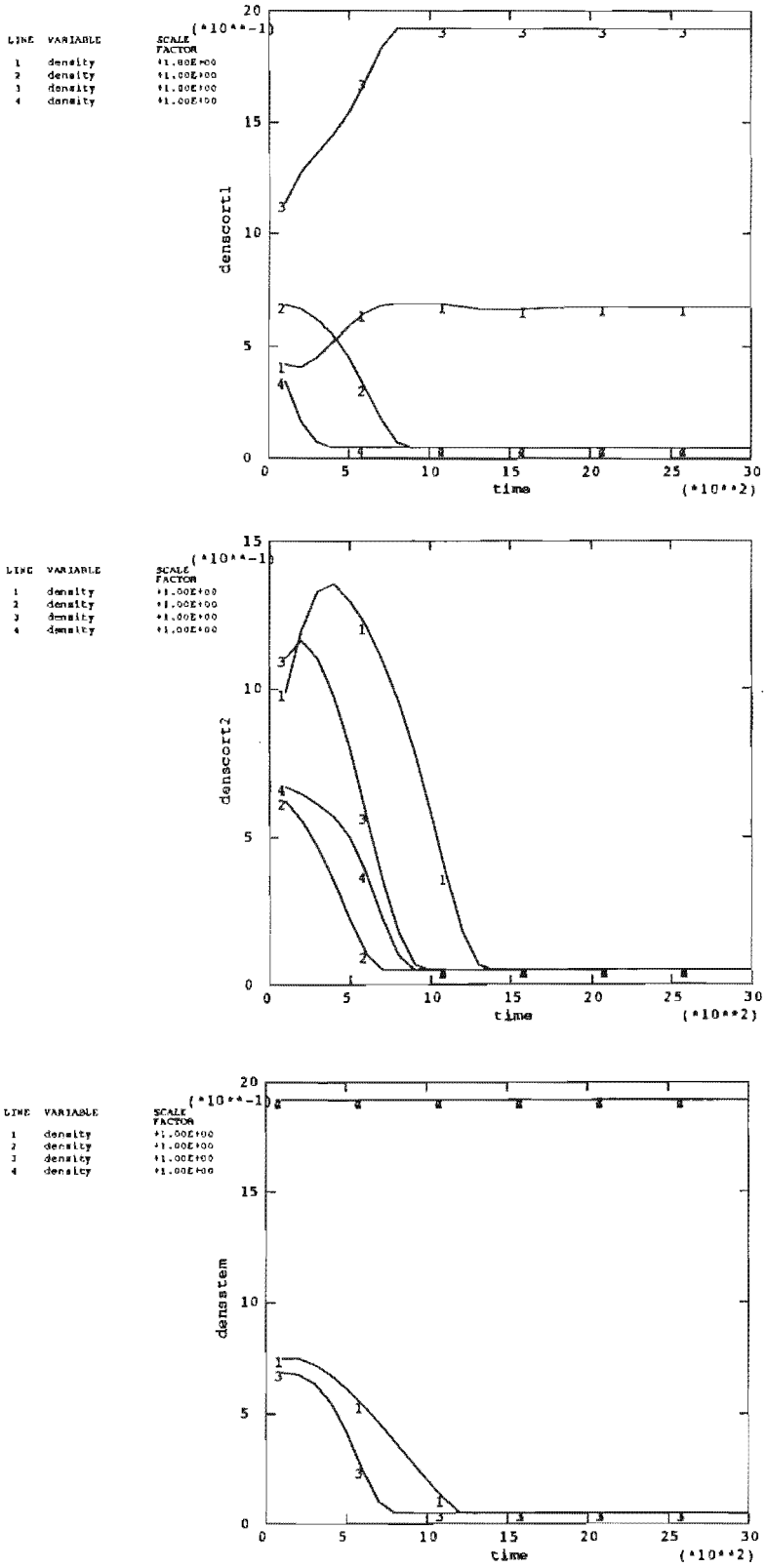

Figure 7.5: History plots of twelve different elements in a long-term simulation. Elements 9 to 12 are at the top, elements 5 to 8 in the middle, and elements 1 to 4 at the bottom.

7.1.2 Results of the strain based algorithm used in conjunction with a sigmoidal remodelling surface velocity applied in two dimensions

This subsection contains results obtained when the constitutive model presented by Jacobs [47] is altered as described in Chapter 5. This includes implementing the strain based algorithm outlined in Section 5.4, and also changing the remodelling surface velocity to be a double sigmoidal function of remodelling error as shown in Section 5.4.3.

Lengthened femoral shaft. The first modification made to Jacob's model, however, is the lengthening of the femoral stem so that the bending stress is not a maximum at the boundary. The stress distribution in both a short and a long stem for a bending load are shown in Figure 7.6. All subsequent two-dimensional plane strain runs are performed using a finite element mesh with a lengthened femoral shaft as shown in Figure 7.6.

Strain based algorithm with physiologically realistic parameters. One of the aims of using a strain based remodelling formulation is that one can use parameters that have been measured physiologically. These include the width of the physiological strain region (see Figure 5.6) as well as the remodelling surface velocity on either side of this region. According to the literature [63] [37], the maximal surface remodelling velocity for apposition is of the order of $2\,\mu m/day$, whereas the maximal resorption surface remodelling velocity is about $20\,\mu m/day$. These two surface remodelling velocities correspond to the parameters c_1 and c_2 in the algorithm presented in Section 5.4, and the influence these parameters have on the remodelling response will become clear when looking at the results presented in Figures 7.7 to 7.10. Taking one iteration to be the amount of loading undergone during normal activity in one day, it becomes clear that it is unreasonable to take the number of cycles n as 10000 for a gait activity: that would require a step taken every 8.64 seconds, 24 hours a day. In all subsequent runs the number of load cycles was thus reduced to $n = 5000$, which seems more physiologically reasonable. The first run with the strain based model is one implementing these physiological parameters. The initial density in this run was set to be $\rho_i = 0.7\,g/cm^3$.

Effect of equal remodelling velocities. As can be seen from these density contour plots, the density distribution after 150 steps of remodelling with physiological remodelling velocity parameters does not look physiological. Hence the parameters c_1

and c_2 were altered so as to achieve a more physiological distribution. In the study whose results are shown in Figures 7.11 to 7.14, $c_1 = c_2 = 2\,\mu m/day$

Dependence on initial conditions. The effect of initial conditions was also investigated by starting two identical runs with $\rho_i = 0.7\,g/cm^3$, given earlier in figures 7.11 to 7.14, and $\rho_i = 1.92\,g/cm^3$, given in Figures 7.15 to 7.16, respectively. This run $\rho_i = 1.92\,g/cm^3$ has been documented with only two density contour plots. A history plot of density in the twelve elements described in Figure 7.2 is also included.

Development of physiological structures. This experimental run is included to demonstrate the development of physiological features in the model. The parameters for this run are $c_1 = 5\,\mu m/day$, $c_2 = 2\,\mu m/day$, $\rho_i = 1.1\,g/cm^3$. The density evolution is at intervals 20, 40, 60 and 80 increments is traced in Figures 7.18 to 7.21. History plots are given in Figure 7.22.

Density distribution after a large number of increments. The last of the two-dimensional numerical experiments was a long-term run investigating the trend towards a steady state for the strain based algorithm applied to the plane strain problem. Here, only two density contour plots are included: one at time 100 days and one at 3000 days. The parameters for this run were $c_1 = 10\,\mu m/day$, $c_2 = 2\,\mu m/day$, $\rho_i = 1.1\,g/cm^3$. The results are shown in Figures 7.23 and 7.24, and history plots are provided in Figure 7.25.

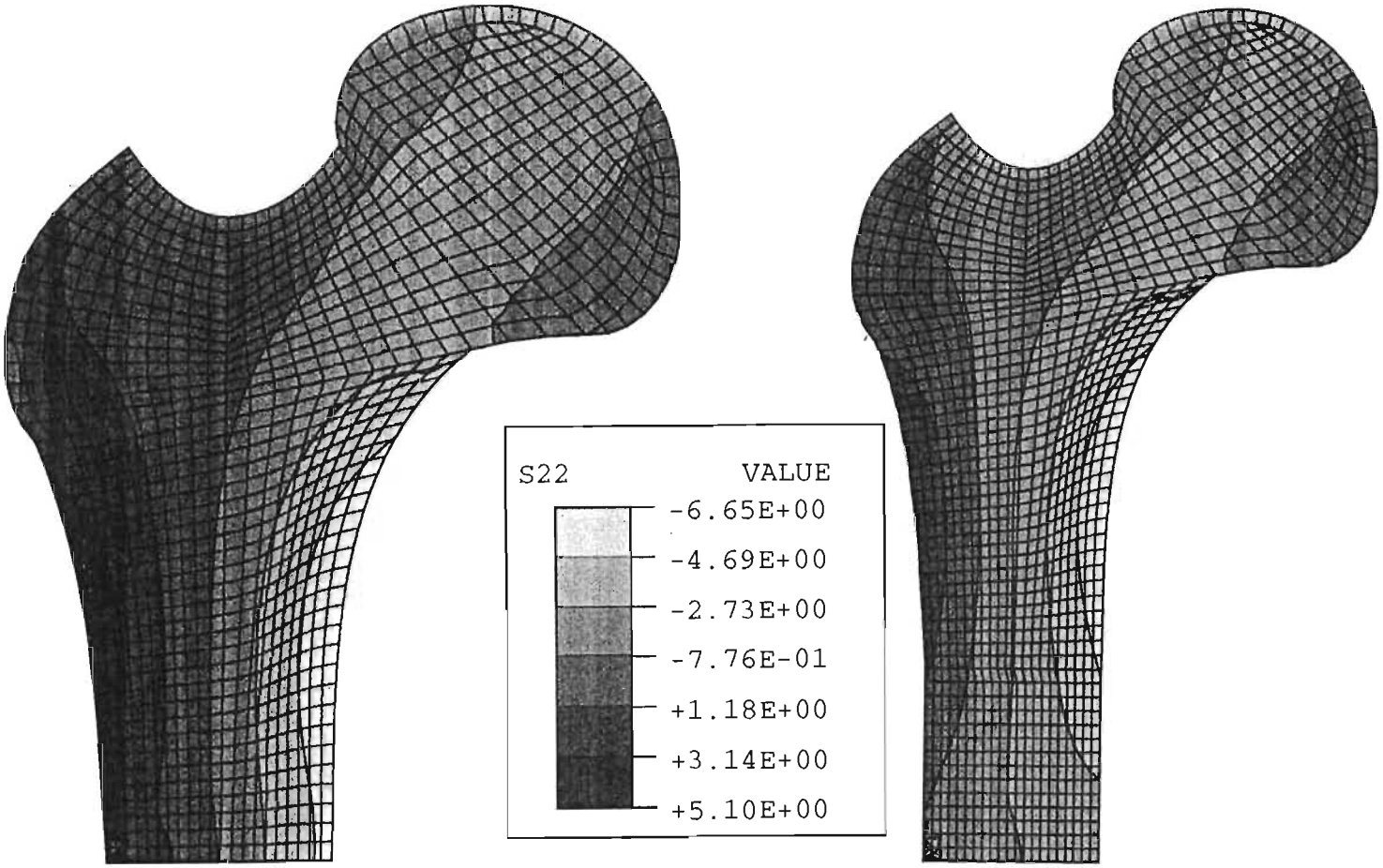

Figure 7.6: Stress distributions in a proximal femur model as used by Jacobs (mesh on the left), as well as in a model with a lengthened stem, induced by a bending load.

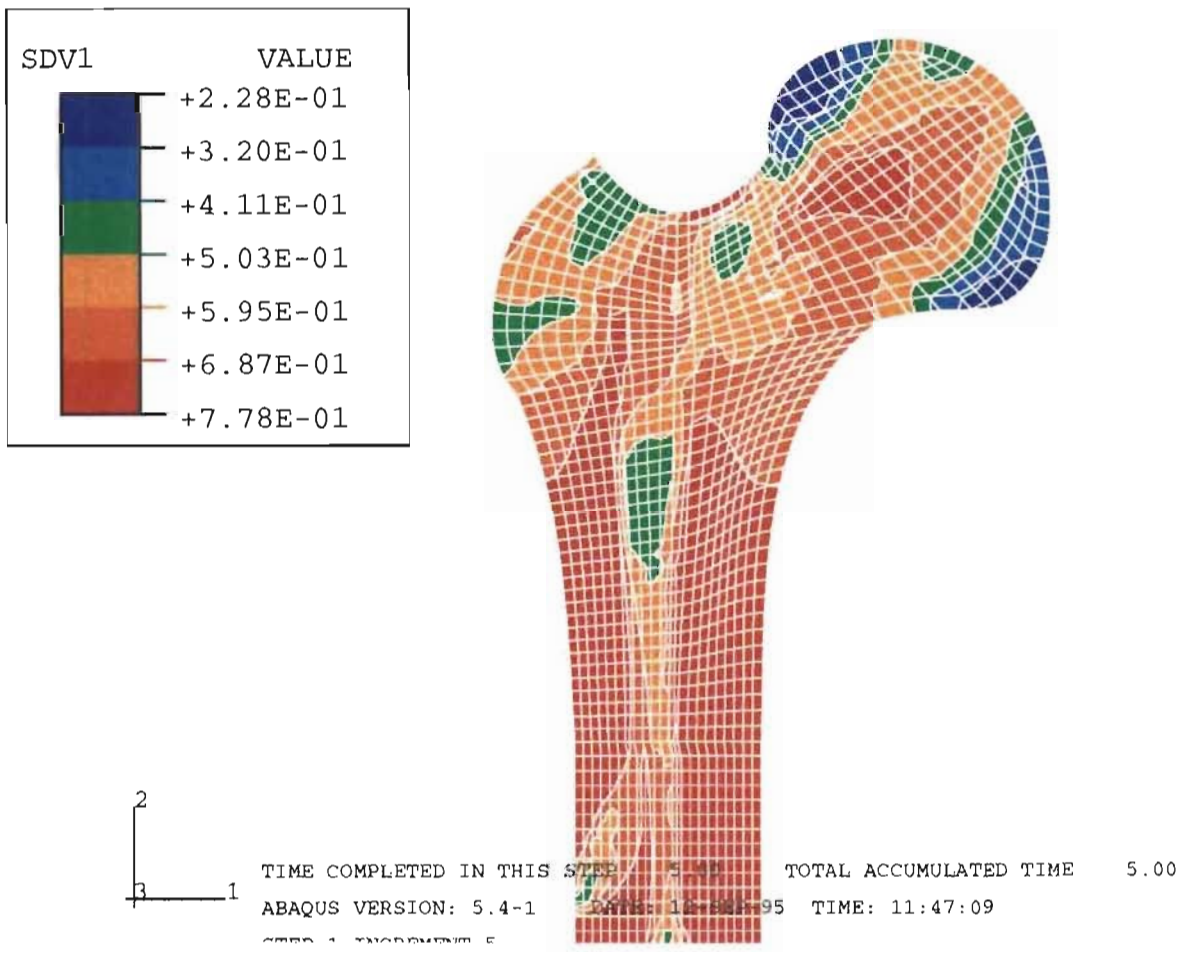

Figure 7.7: Physiological parameters run: density contours at time = 5 days (one permutation of all the different loads). The parameters are $c_1 = 2\,\mu m/day$, $c_2 = 20\,\mu m/day$, $\rho_i = 0.7\,g/cm^3$.

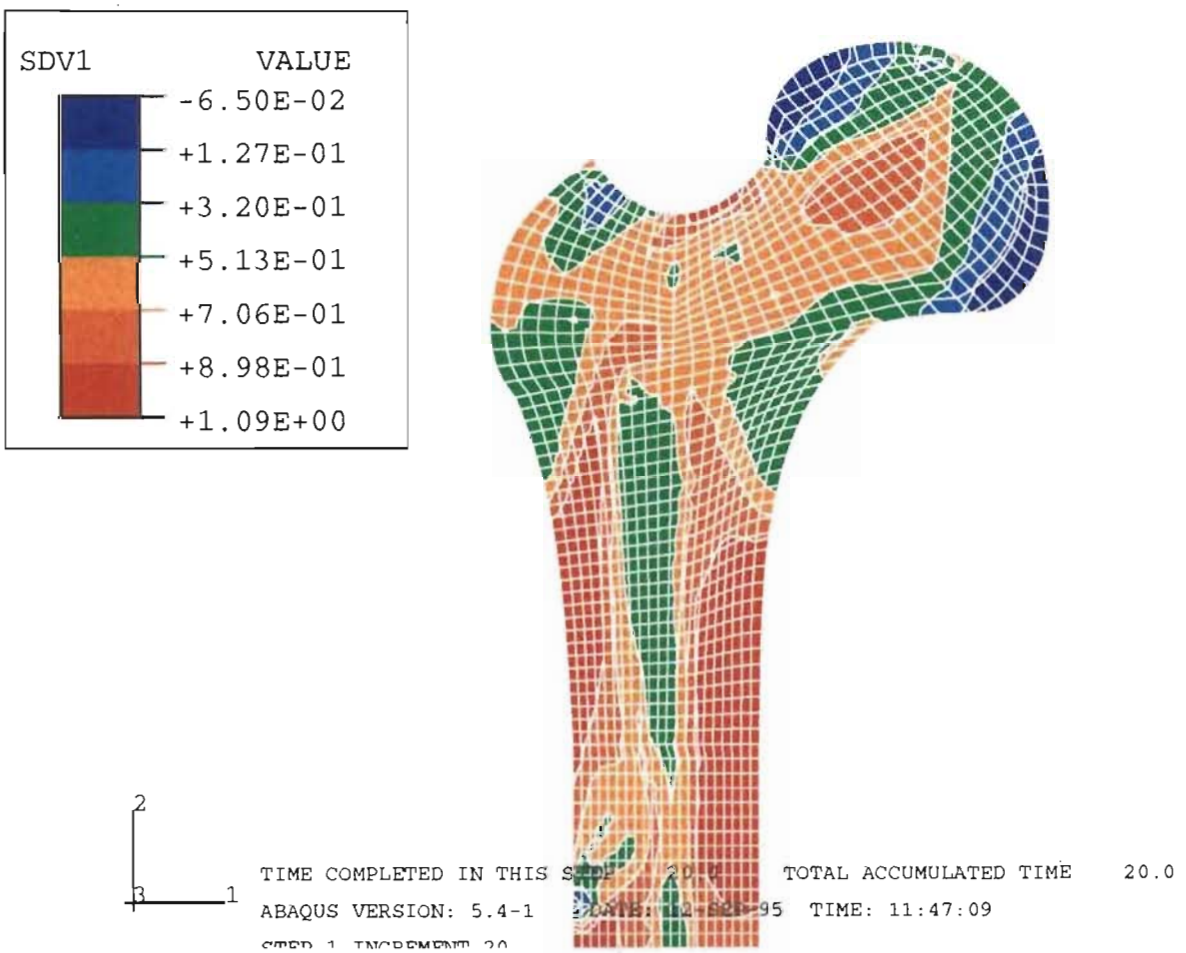

Figure 7.8: Physiological parameters run: density contours at time = 20 days. The parameters are $c_1 = 2\,\mu m/day$, $c_2 = 20\,\mu m/day$, $\rho_i = 0.7\,g/cm^3$.

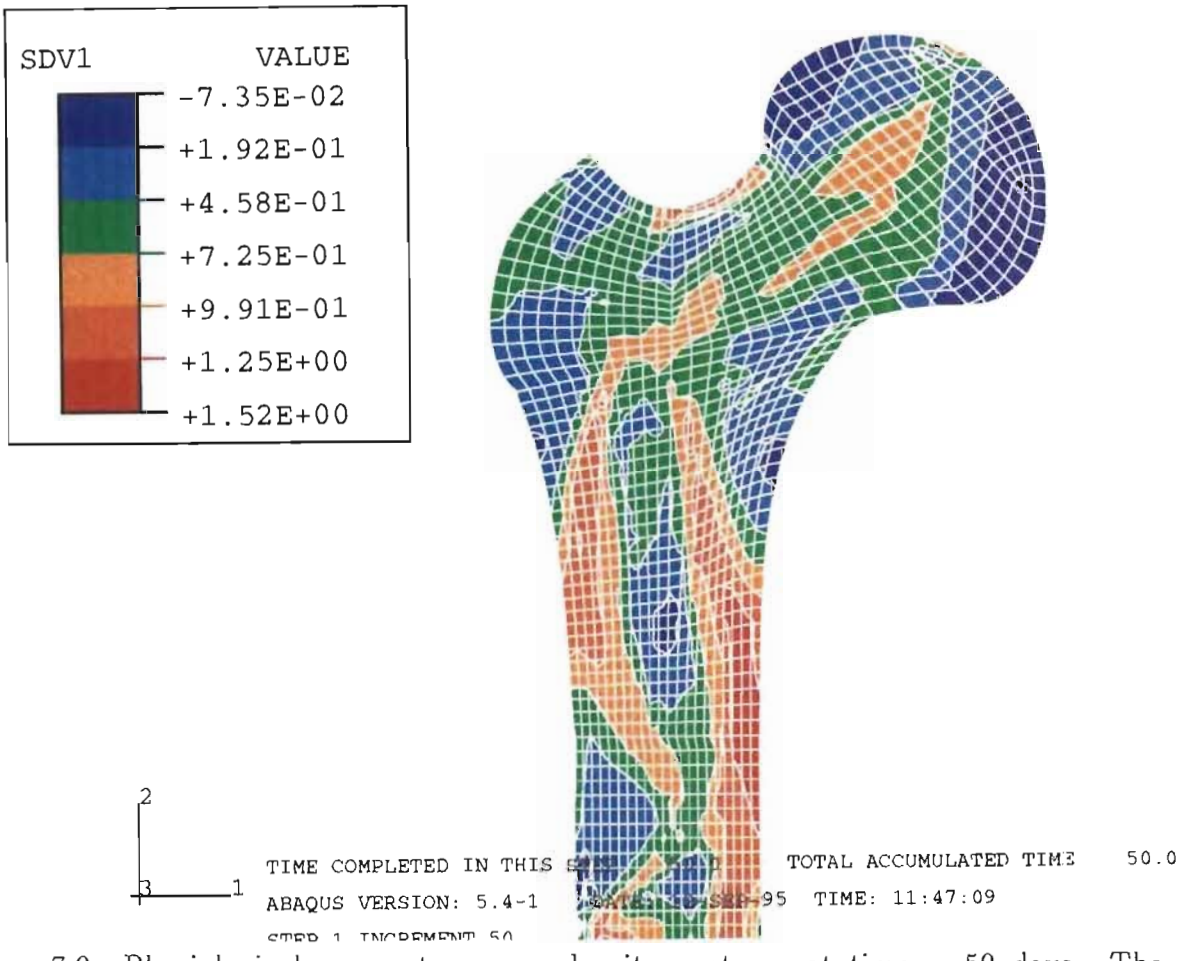

Figure 7.9: Physiological parameters run: density contours at time = 50 days. The parameters are $c_1 = 2\,\mu m/day$, $c_2 = 20\,\mu m/day$, $\rho_i = 0.7\,g/cm^3$.

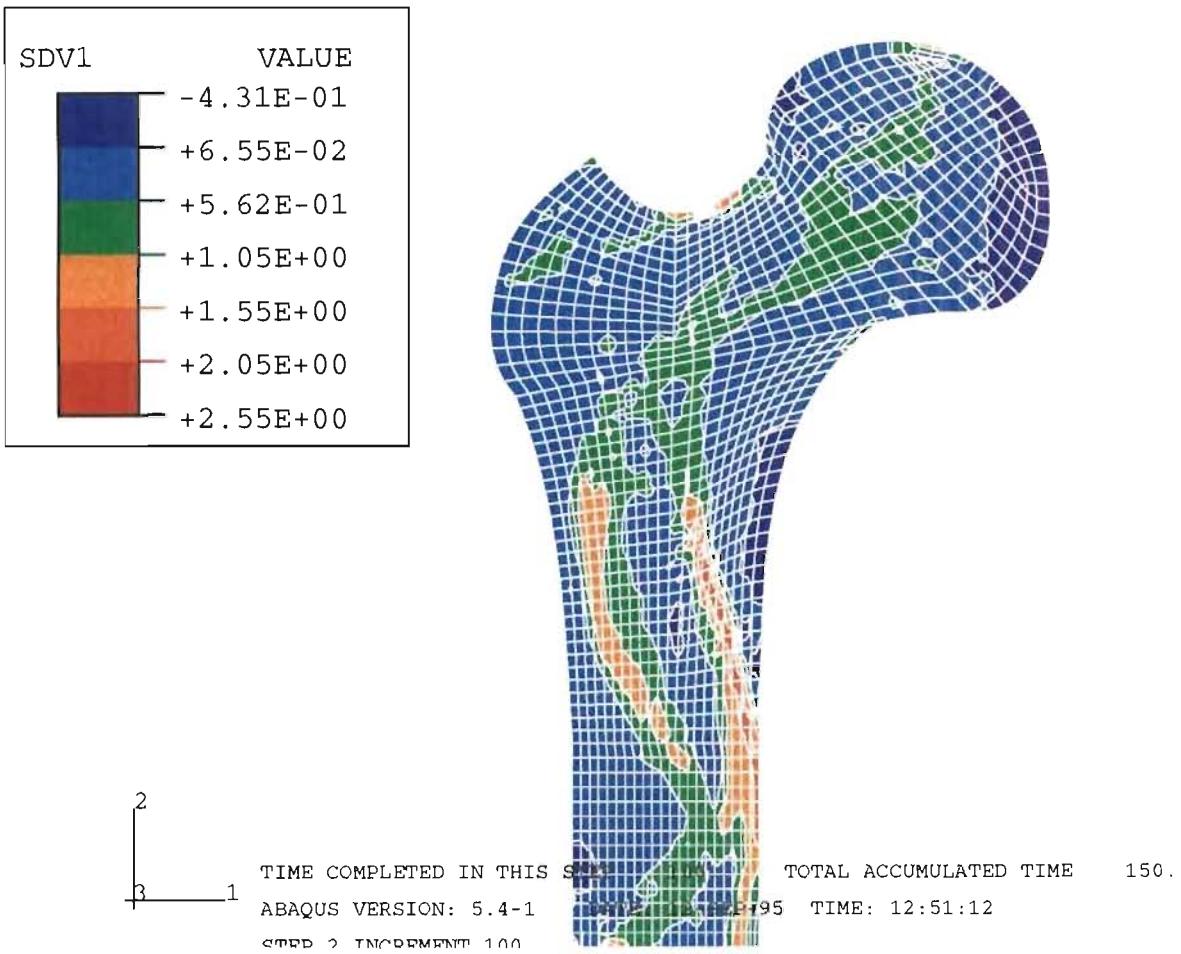

Figure 7.10: Physiological parameters run: density contours at time = 150 days. The parameters are $c_1 = 2\,\mu m/day$, $c_2 = 20\,\mu m/day$, $\rho_i = 0.7\,g/cm^3$.

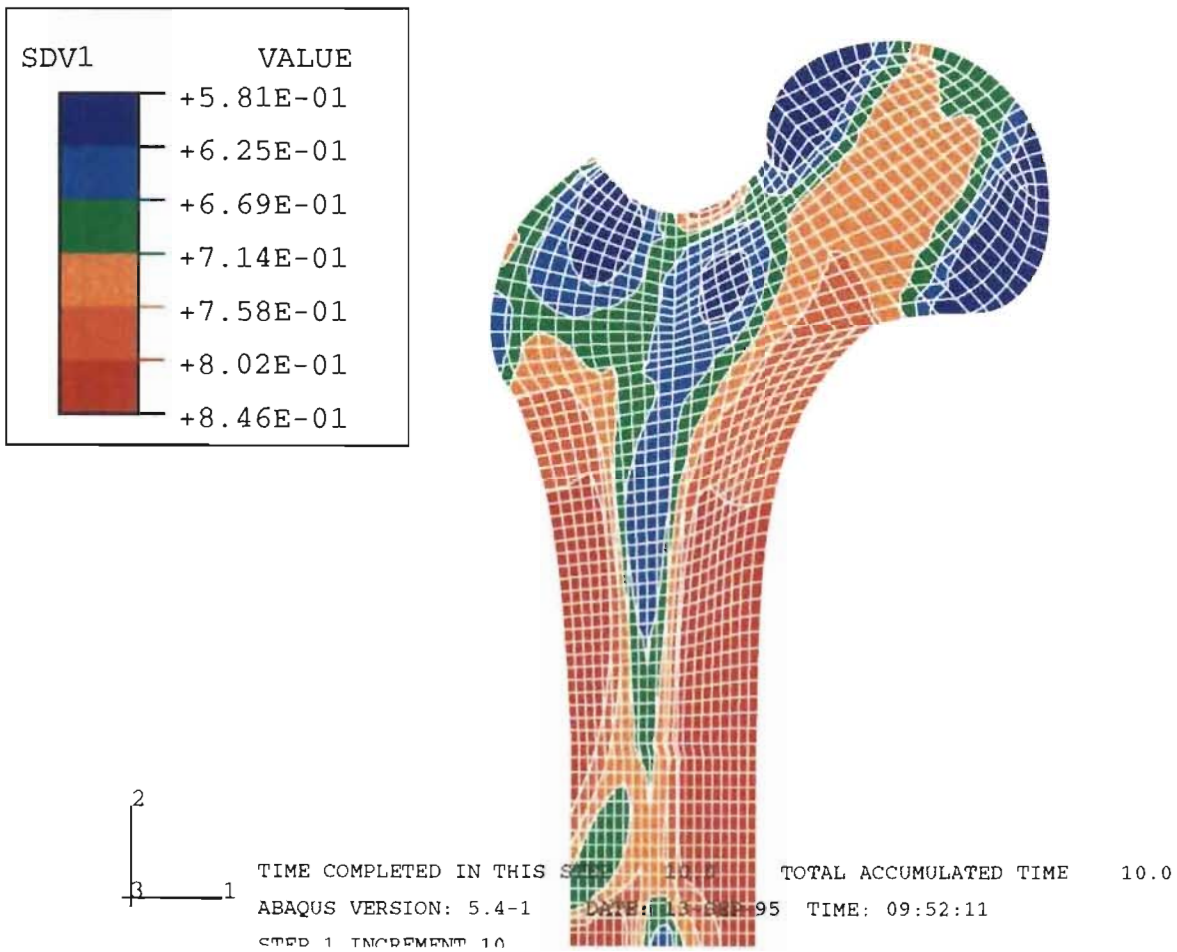

Figure 7.11: Run with $c_1 = c_2 = 2\,\mu m/day$, $\rho_i = 0.7\,g/cm^3$; density contours at time = 10 days.

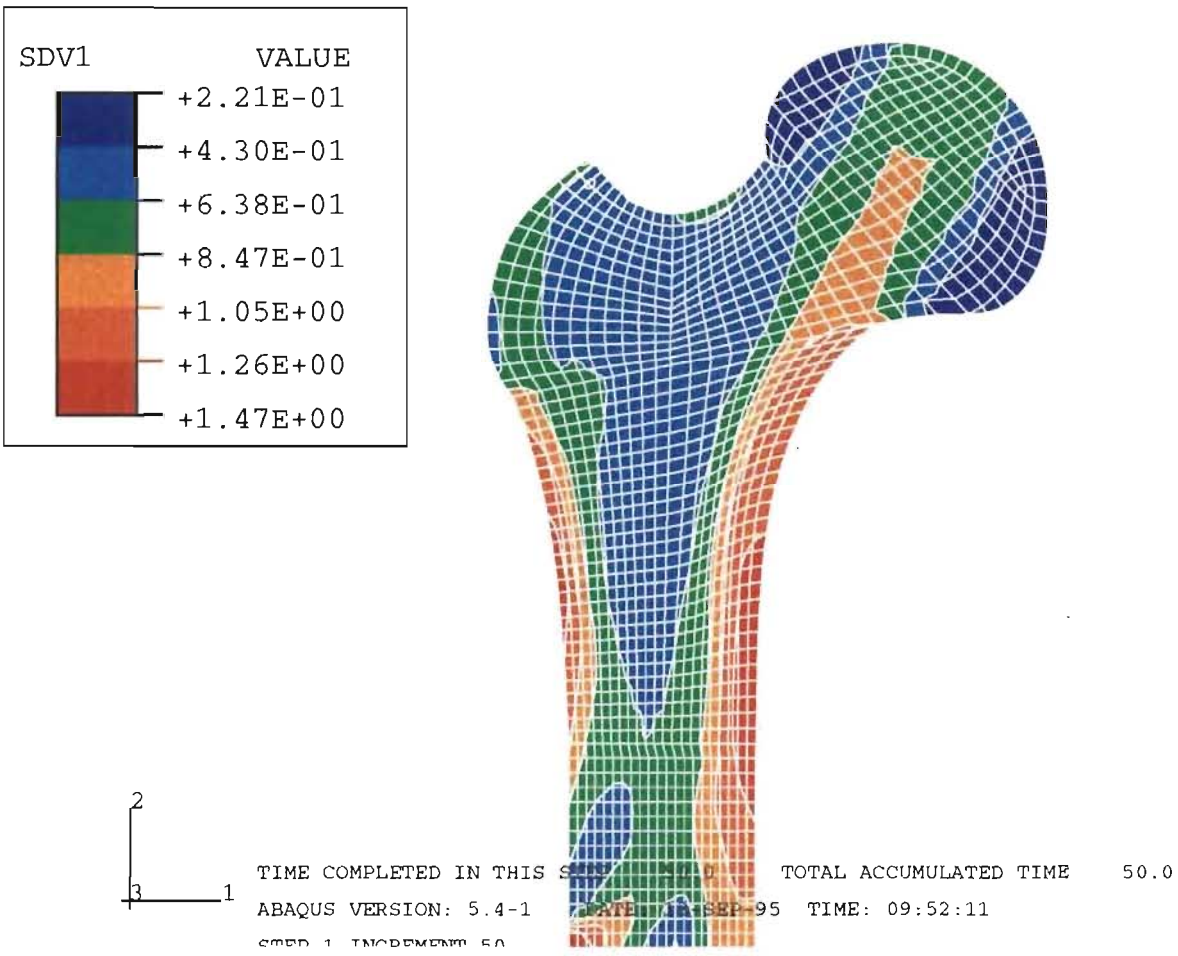

Figure 7.12: Run with $c_1 = c_2 = 2\,\mu m/day$, $\rho_i = 0.7\,g/cm^3$; density contours at time = 50 days.

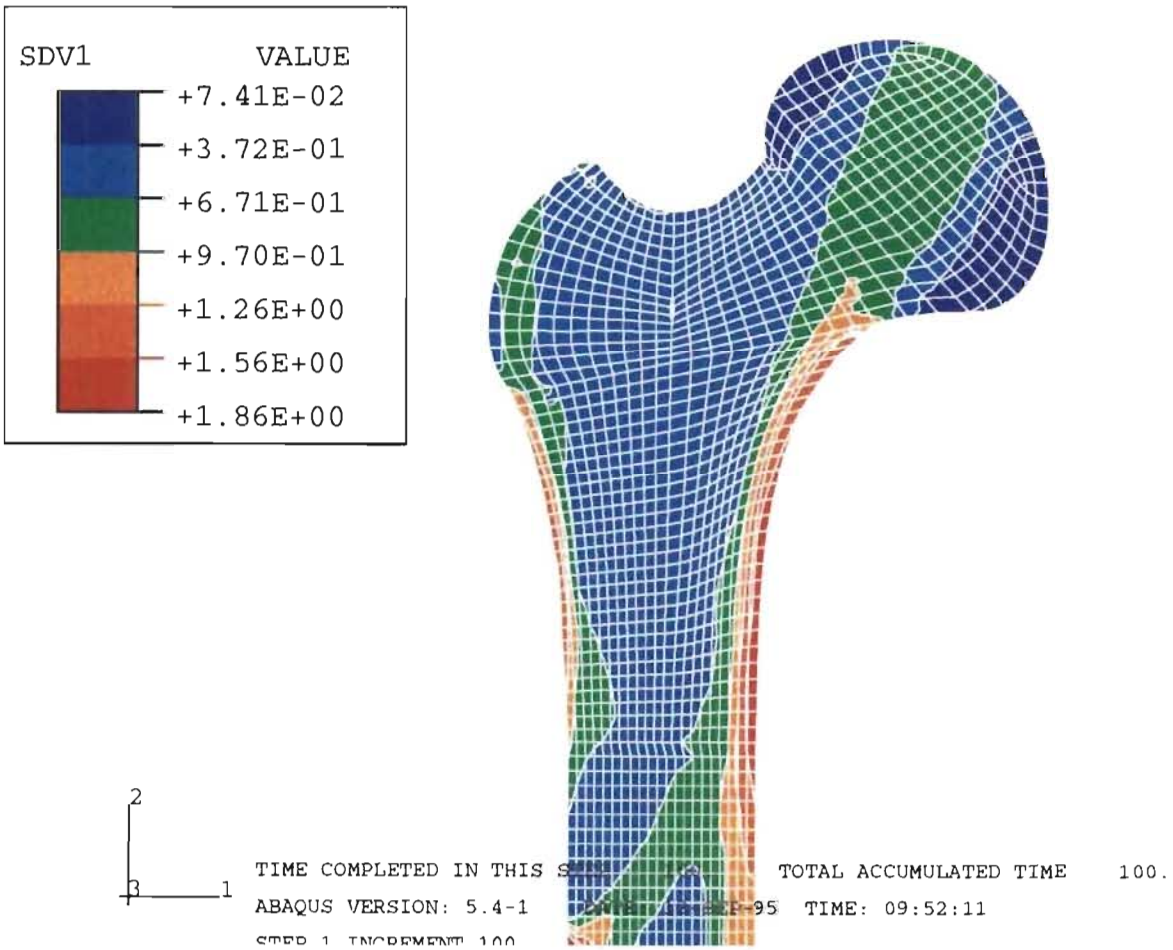

Figure 7.13: Run with $c_1 = c_2 = 2\,\mu m/day$, $\rho_i = 0.7\,g/cm^3$; density contours at time = 100 days.

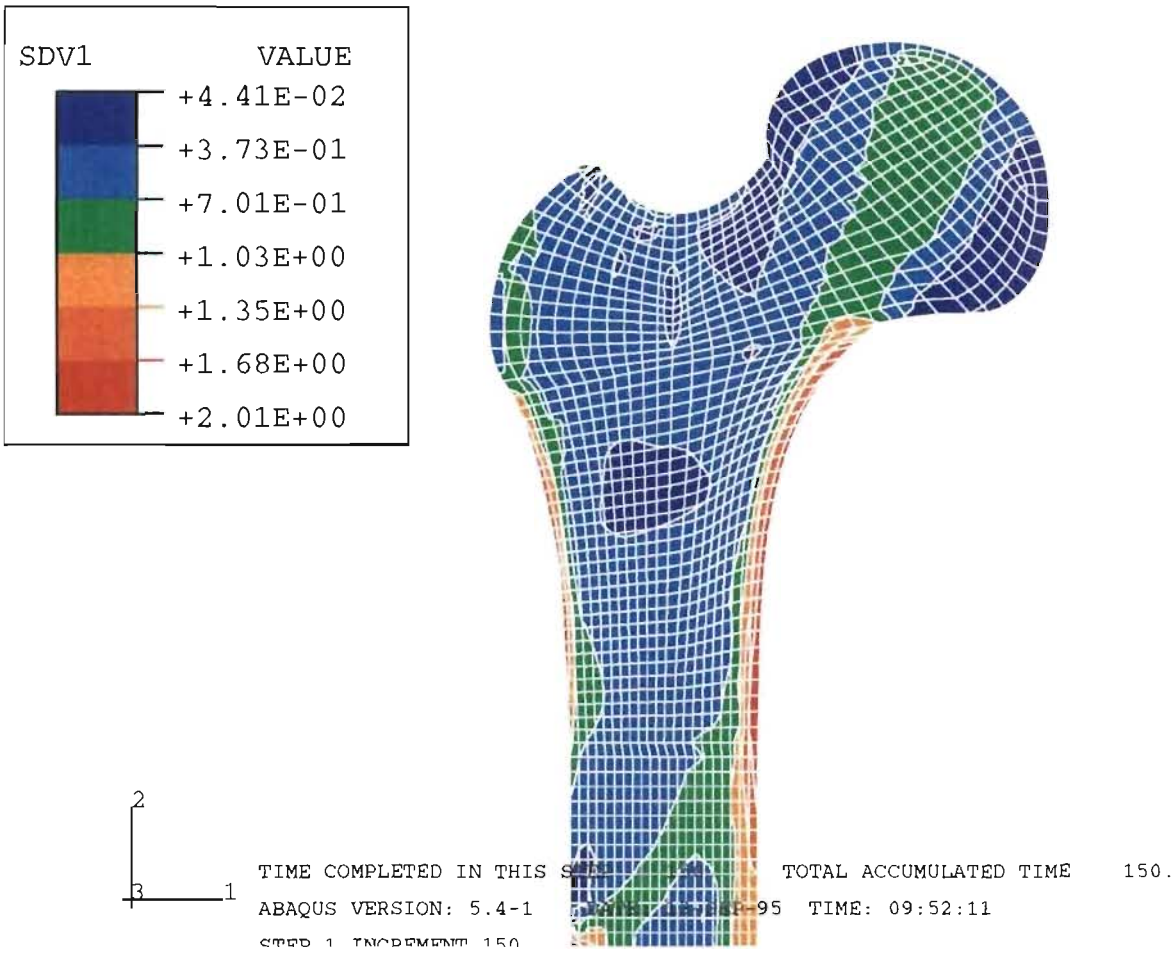

Figure 7.14: Run with $c_1 = c_2 = 2\,\mu m/day$, $\rho_i = 0.7\,g/cm^3$; density contours at time = 150 days.

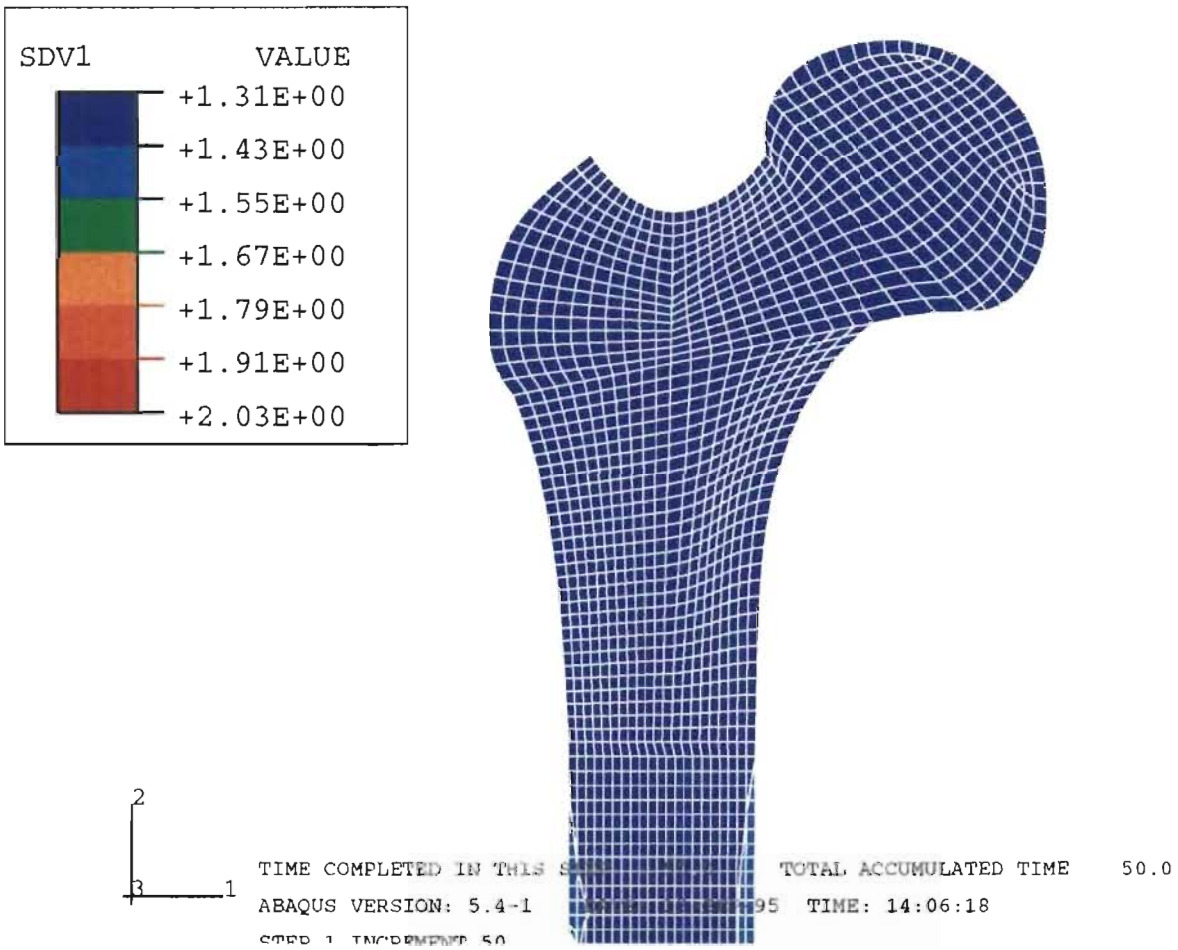

Figure 7.15: Run with $c_1 = c_2 = 2\,\mu m/day$ and $\rho_i = 1.92\,g/cm^3$: density contours at time = 50 days.

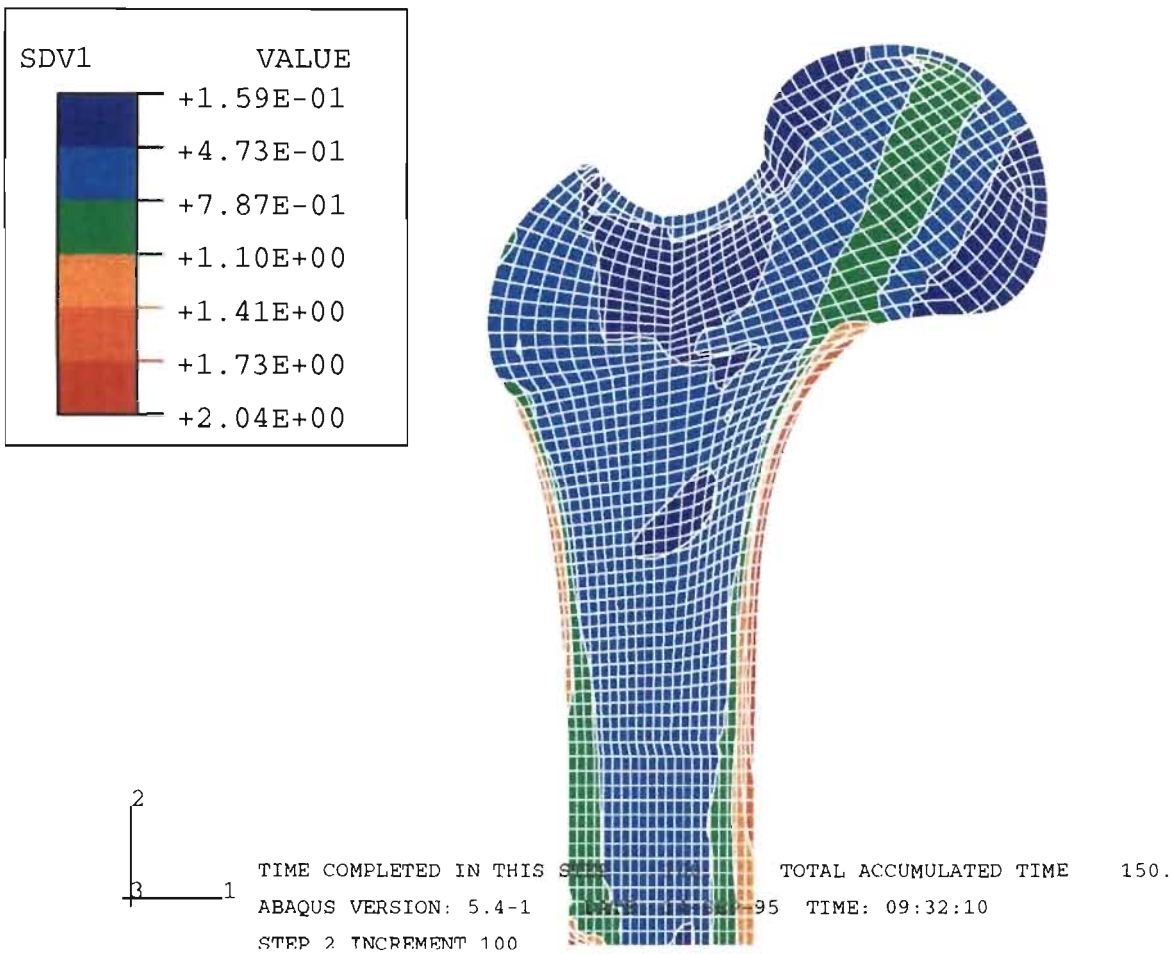

Figure 7.16: Run with $c_1 = c_2 = 2\,\mu m/day$ and $\rho_i = 1.92\,g/cm^3$: density contours at time = 150 days.

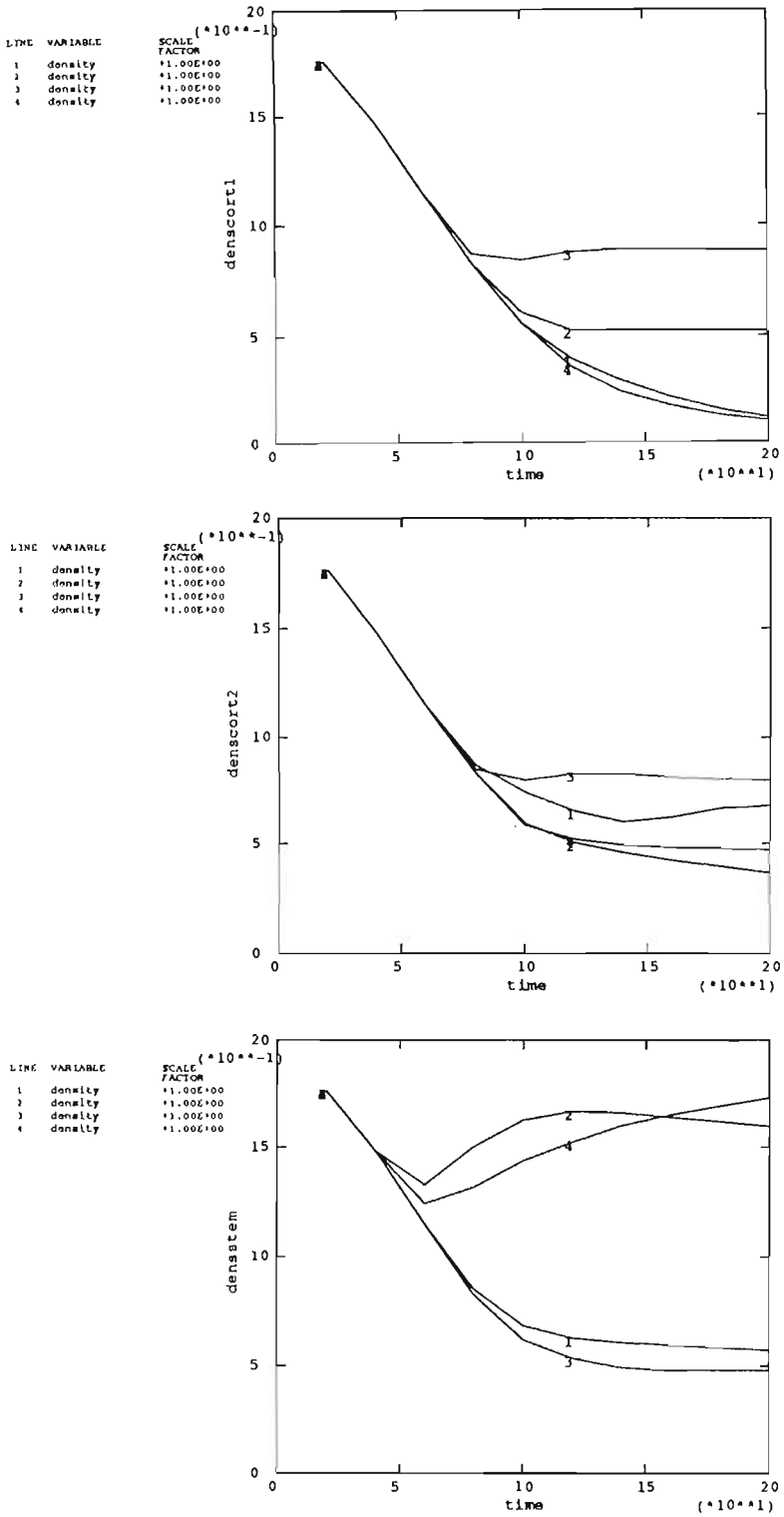

Figure 7.17: History plots of twelve different elements in the run described above with initial density $\rho_i = 1.92\, g/cm^3$ and $c_1 = c_2 = 2\, \mu m/day$.

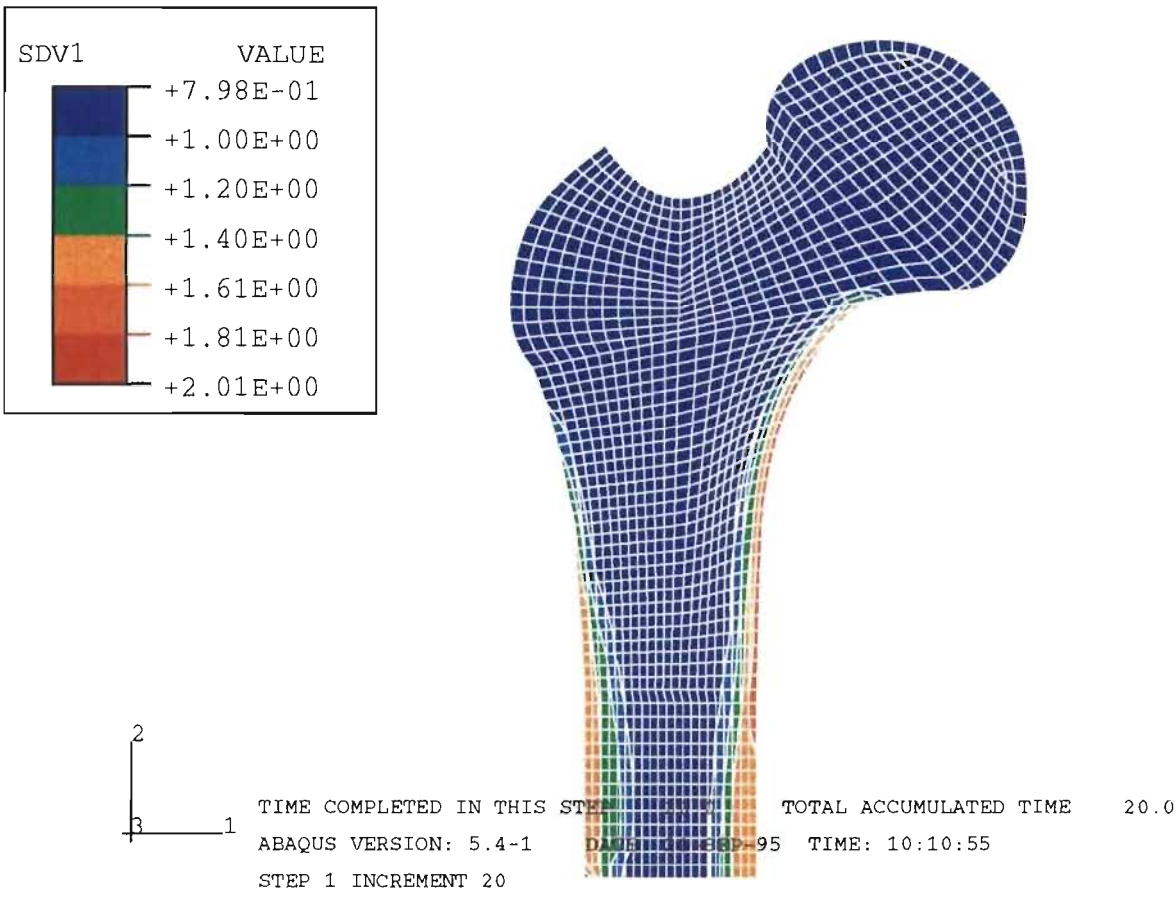

Figure 7.18: Run with $c_1 = 10\,\mu m/day$, $c_2 = 2\,\mu m/day$, $\rho_i = 1.1\,g/cm^3$: density contours at time = 20 days.

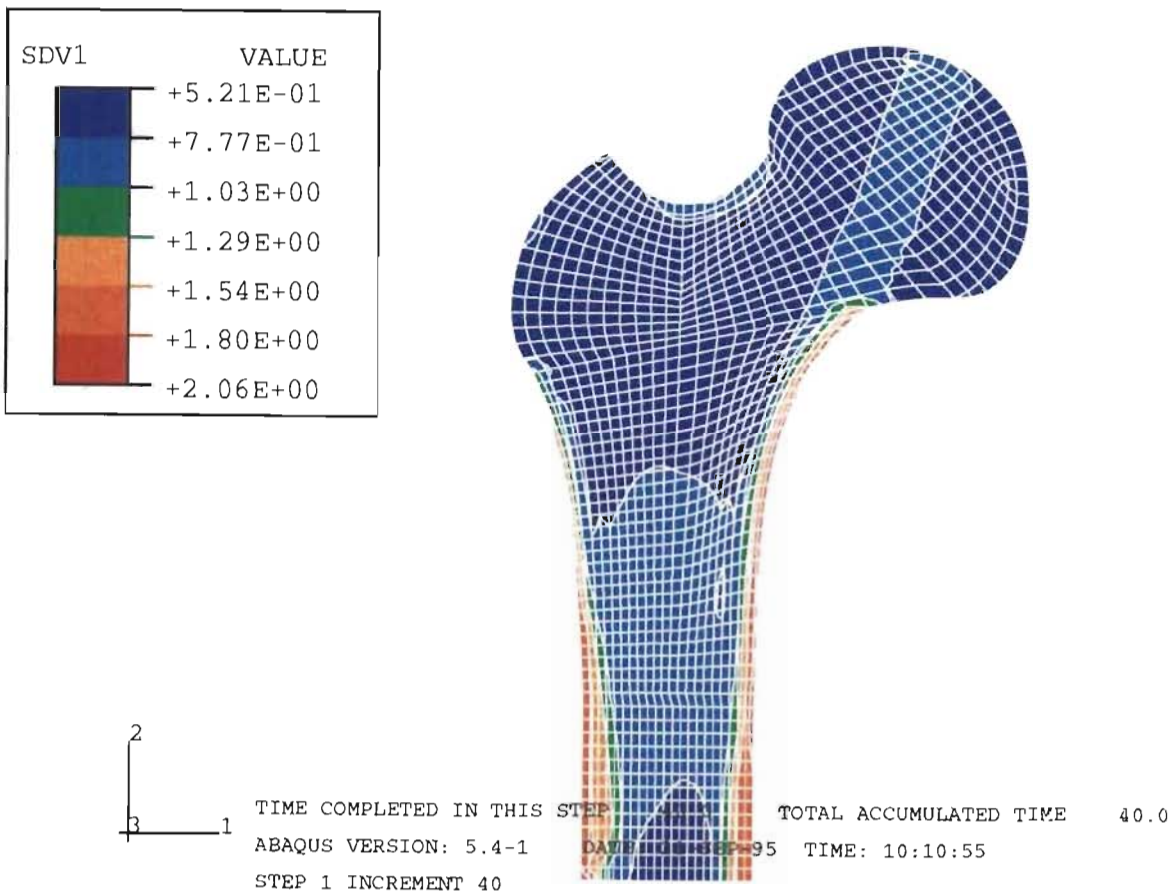

Figure 7.19: Run with $c_1 = 10\,\mu m/day$, $c_2 = 2\,\mu m/day$, $\rho_i = 1.1\,g/cm^3$: density contours at time = 40 days.

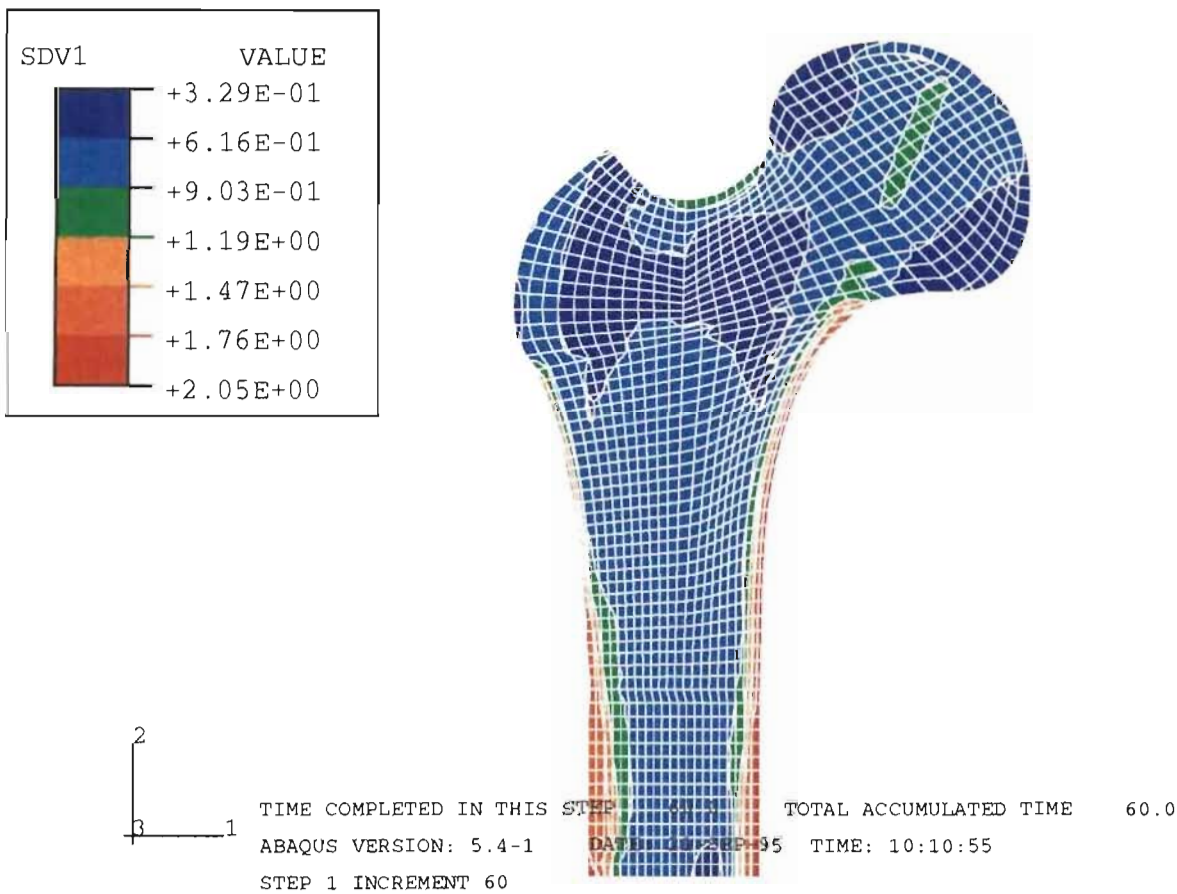

Figure 7.20: Run with $c_1 = 10\,\mu m/day$, $c_2 = 2\,\mu m/day$, $\rho_i = 1.1\,g/cm^3$: density contours at time = 60 days.

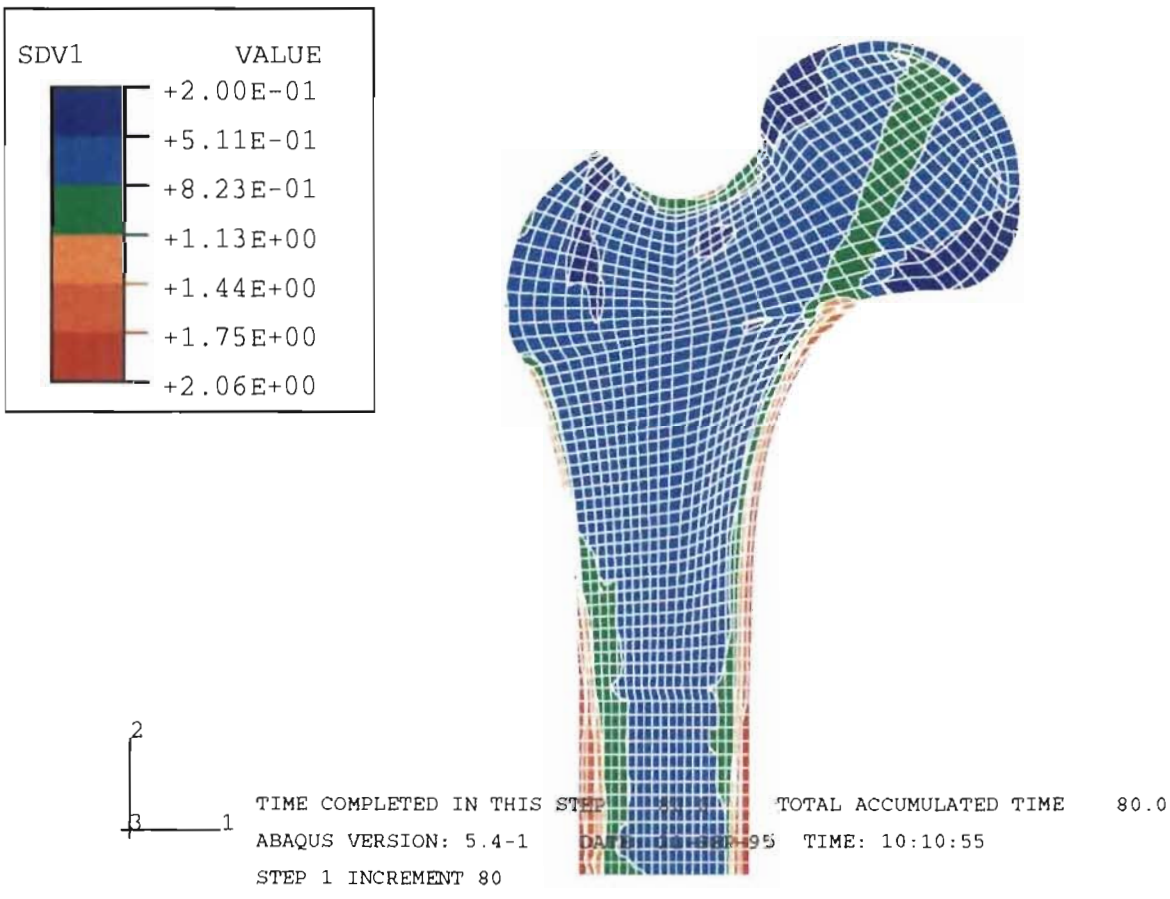

Figure 7.21: Run with $c_1 = 10\,\mu m/day$, $c_2 = 2\,\mu m/day$, $\rho_i = 1.1\,g/cm^3$: density contours at time = 80 days.

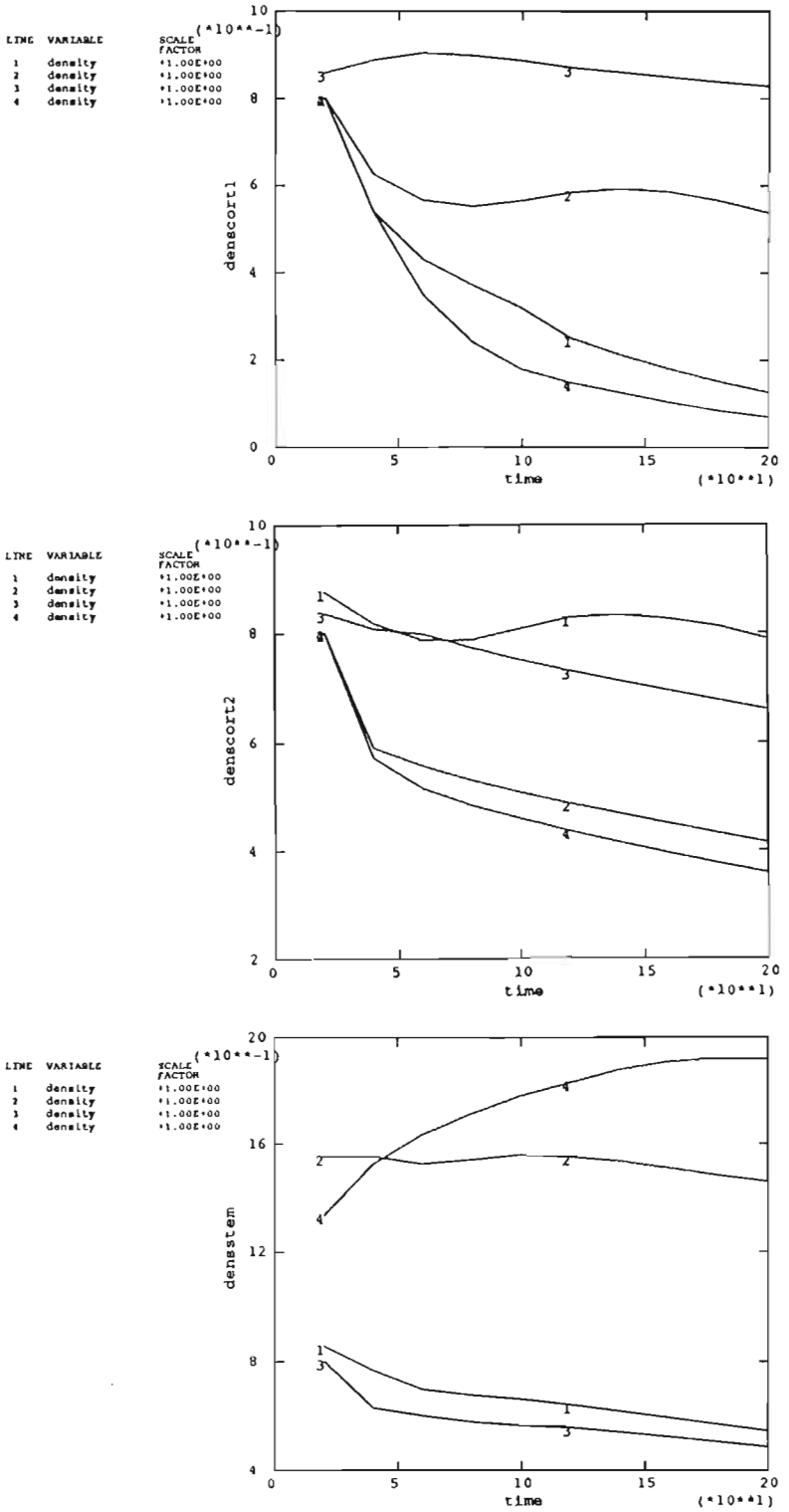

Figure 7.22: History plots of twelve different elements in the run described above with parameters $c_1 = 10\,\mu m/day$, $c_2 = 2\,\mu m/day$, $\rho_i = 1.1\,g/cm^3$.

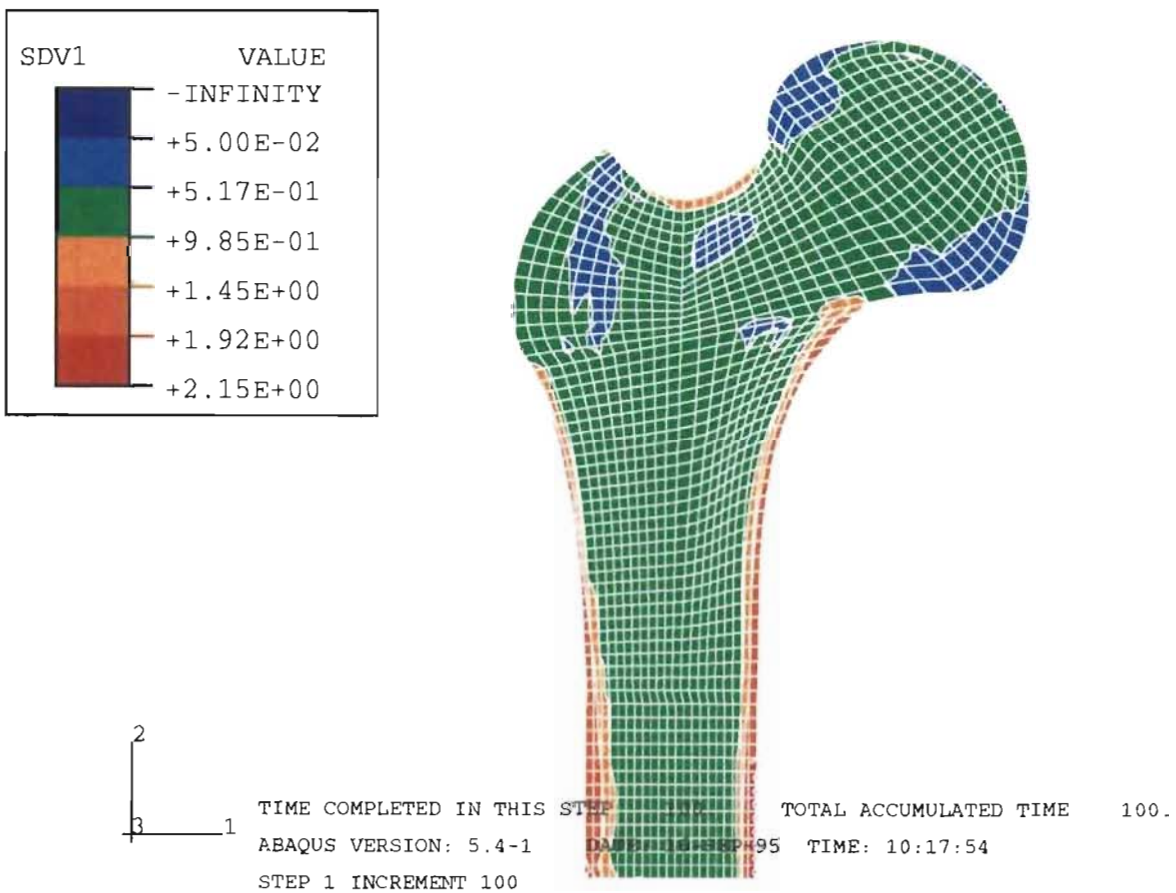

Figure 7.23: Run with $c_1 = 10\,\mu m/day$, $c_2 = 2\,\mu m/day$, $\rho_i = 1.1\,g/cm^3$: density contours at time = 100 days.

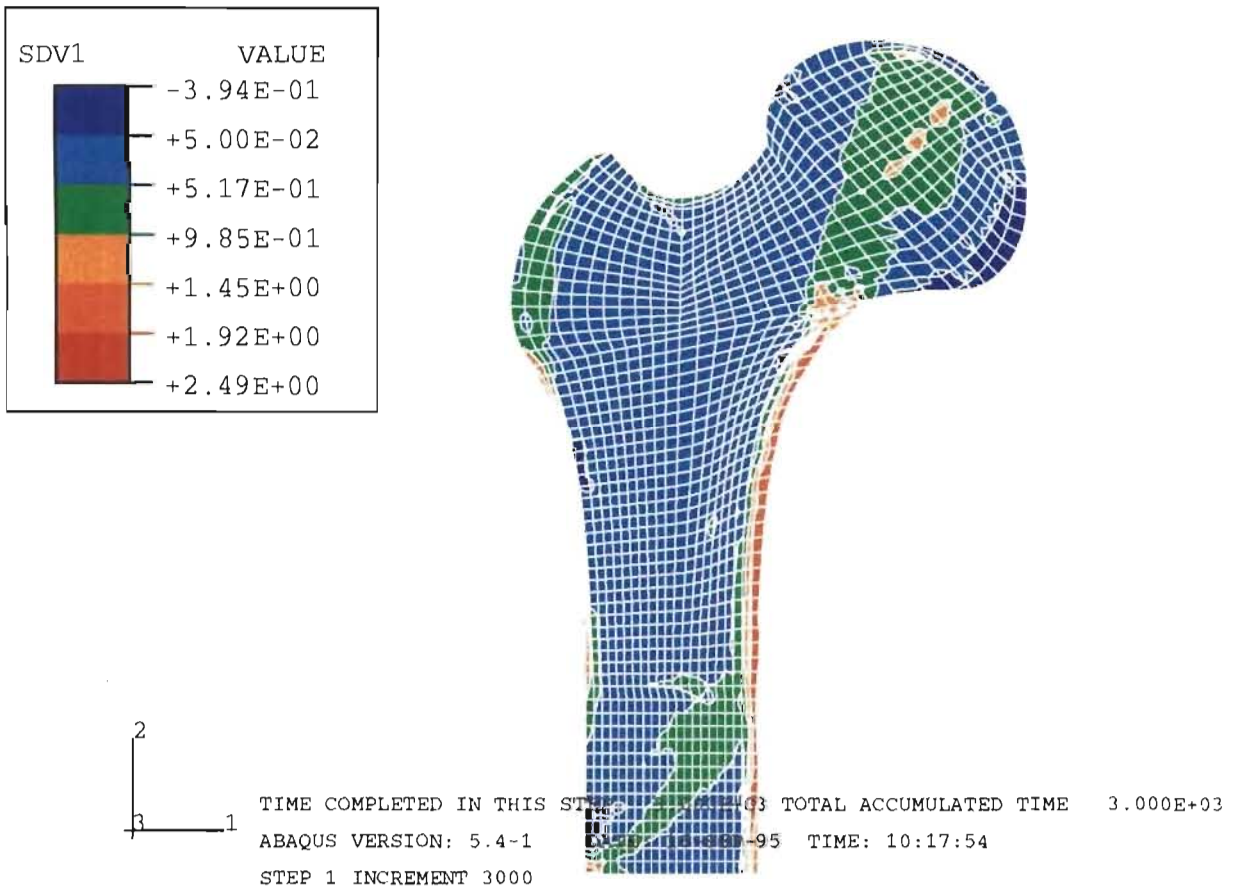

Figure 7.24: Run with $c_1 = 10\,\mu m/day$, $c_2 = 2\,\mu m/day$, $\rho_i = 1.1\,g/cm^3$: density contours at time = 3000 days.

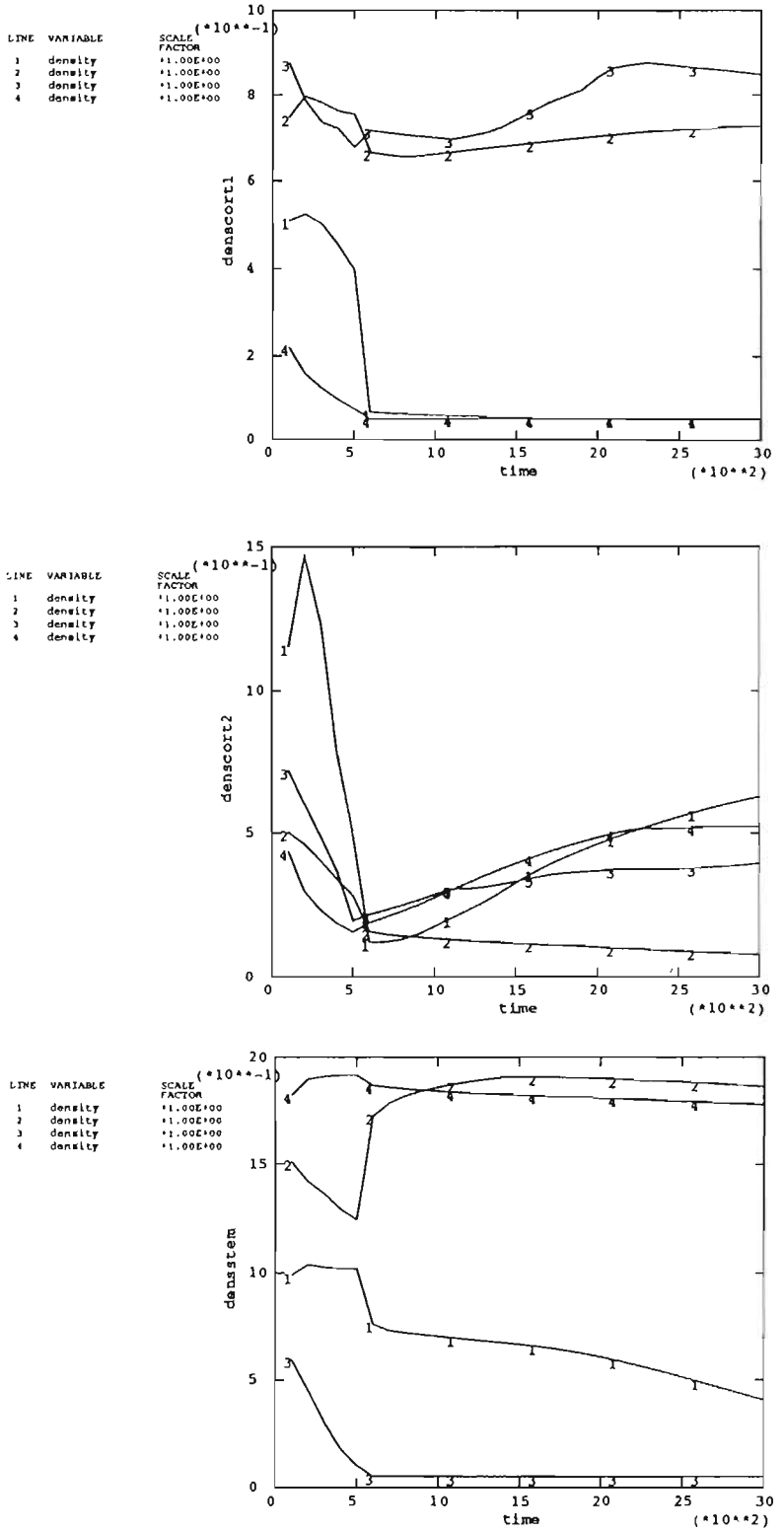

Figure 7.25: History plots of twelve different elements in the run described above with parameters $c_1 = 10\,\mu m/day$, $c_2 = 2\,\mu m/day$, $\rho_i = 1.1\,g/cm^3$.

7.2 Results of Three-Dimensional Implementation

As discussed in chapter 6, the extension of the problem solved in Section 7.1 to three dimensions is very labour-intensive because of the complicated geometry of the proximal femur. Nevertheless a three-dimensional mesh as depicted in Figure 7.26 was designed using the ABAQUS Pre-processor.

Load application. The first three-dimensional numerical experiment was designed to see how different application of the load on the femoral head influences remodelling. As discussed in Section 6.3, one can either apply this force as a pressure load distributed over the femoral head element surfaces, or concentrated over a small area as an equivalent nodal load. Figure 7.27 shows density contours in the cross-section of the mesh after 100 iterations with a concentrated load on the femoral head. The parameters for this analysis are $c_1 = 10\,\mu m/day$, $c_2 = 2\,\mu m/day$, $\rho_i = 1.1\,g/cm^3$. Figure 7.28 shows a similar run using the same parameters, but the load on the femoral head is a distributed pressure load. The two different load cases, applied using the distributed load option described in Section 6.2, and the deflections that they cause along in a proximal femur model of constant density are shown in Figures 7.29 and 7.30.

Three-dimensional remodelling simulation. This numerical experiment was designed to investigate bone remodelling using the strain based remodelling algorithm with the double sigmoid remodelling surface velocity curve. The algorithm was implemented over a timespan of 300 increments, and density contour plots were produced after 20, 40, 60, 80 and 300 increments respectively. These are shown in Figures 7.31 to 7.35. The parameters used in this remodelling simulation are $c_1 = 10\,\mu m/day$, $c_2 = 2\,\mu m/day$, $\rho_i = 1.1\,g/cm^3$. History plots giving the time history of the density in 16 strategically selected elements are also shown (see Figure 7.36). Figure 7.37 shows the density distribution on the surface of the bone after 100 increments.

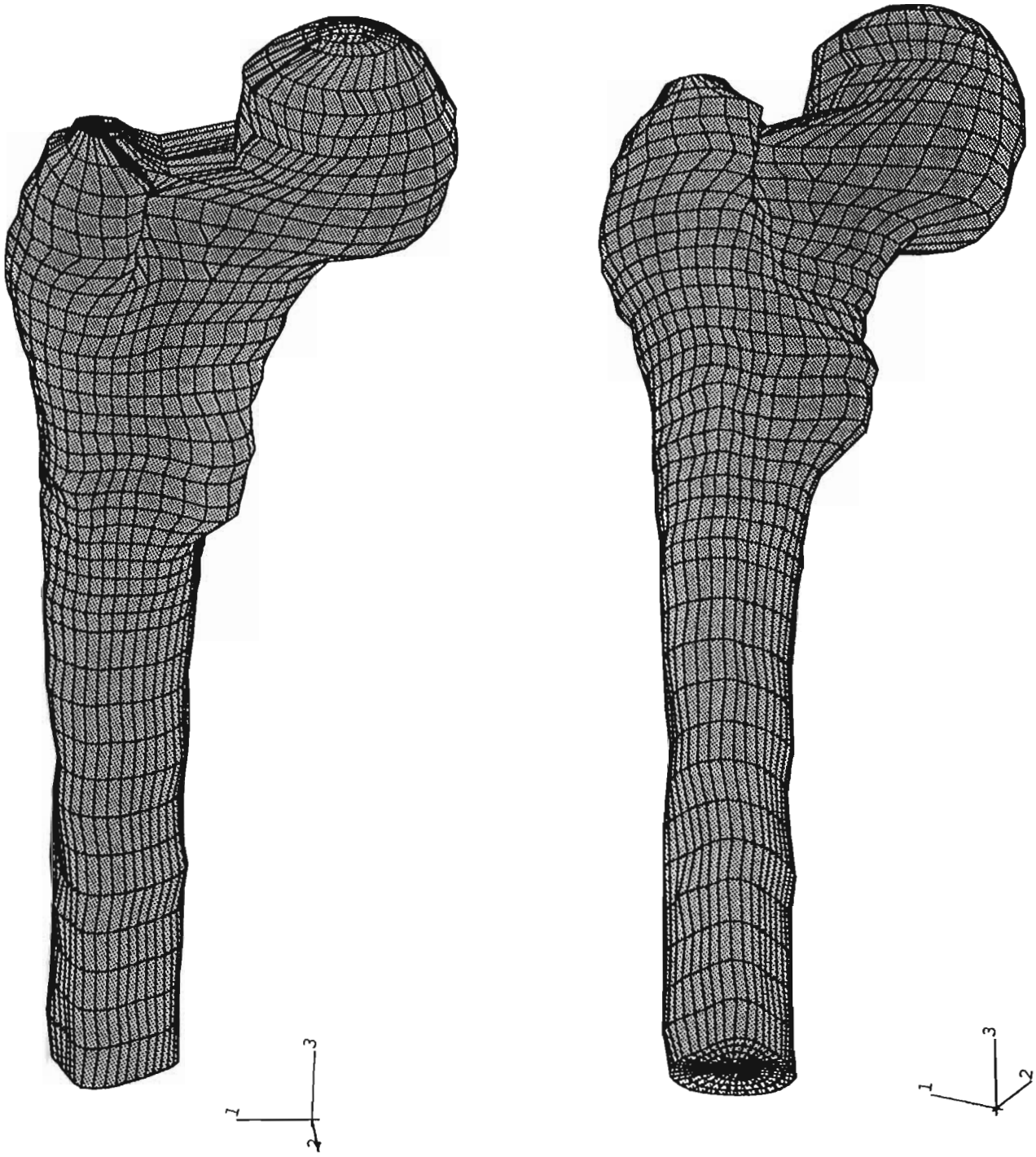

Figure 7.26: Three-dimensional mesh of the proximal femur.

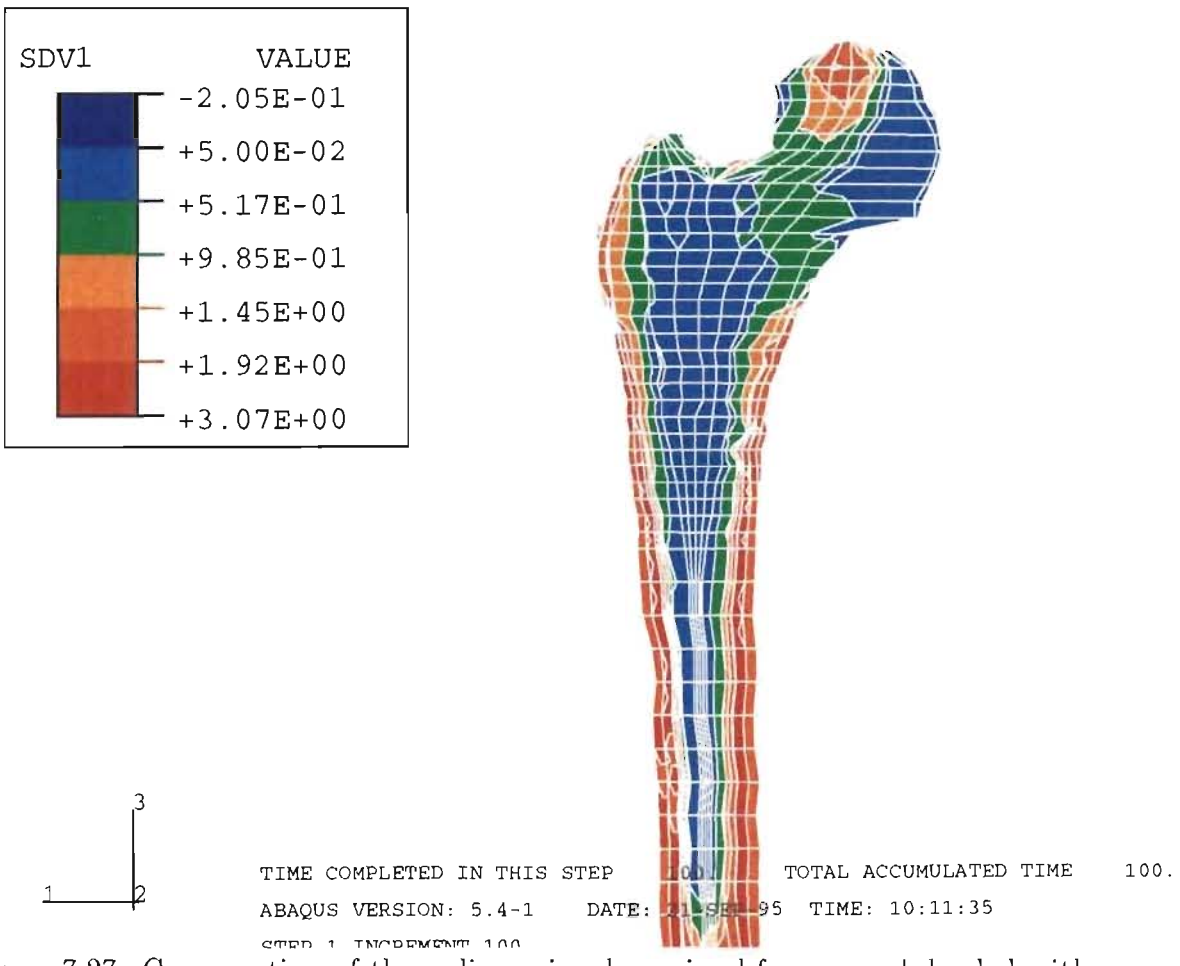

Figure 7.27: Cross-section of three-dimensional proximal femur mesh loaded with a concentrated load on the femoral head, remodelling time = 100 increments. Parameters used are $c_1 = 10\,\mu m/day$, $c_2 = 2\,\mu m/day$, $\rho_i = 1.1\,g/cm^3$.

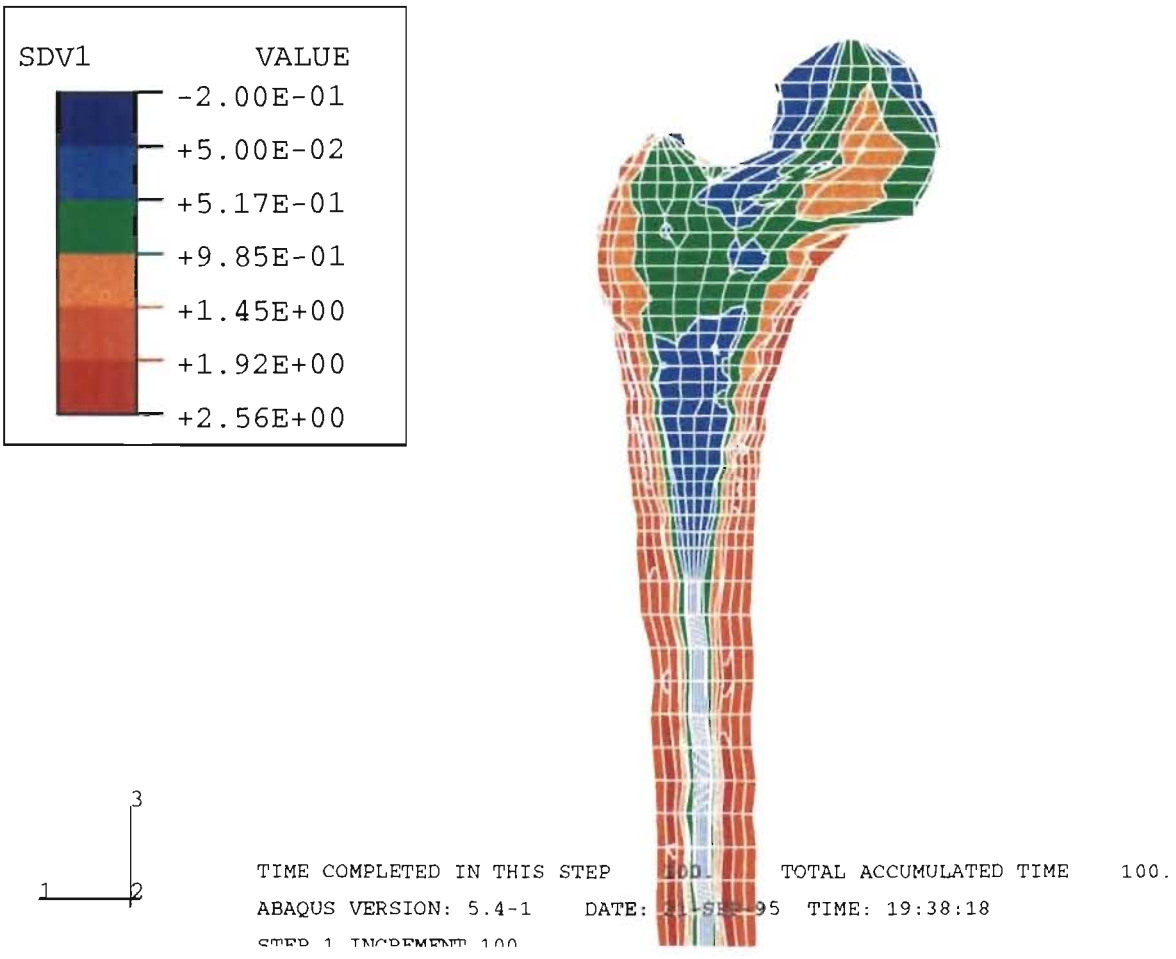

Figure 7.28: Cross-section of three-dimensional proximal femur mesh loaded with a distributed pressure load on the femoral head, remodelling time = 100 increments. Parameters used are $c_1 = 10\,\mu m/day$, $c_2 = 2\,\mu m/day$, $\rho_i = 1.1\,g/cm^3$.

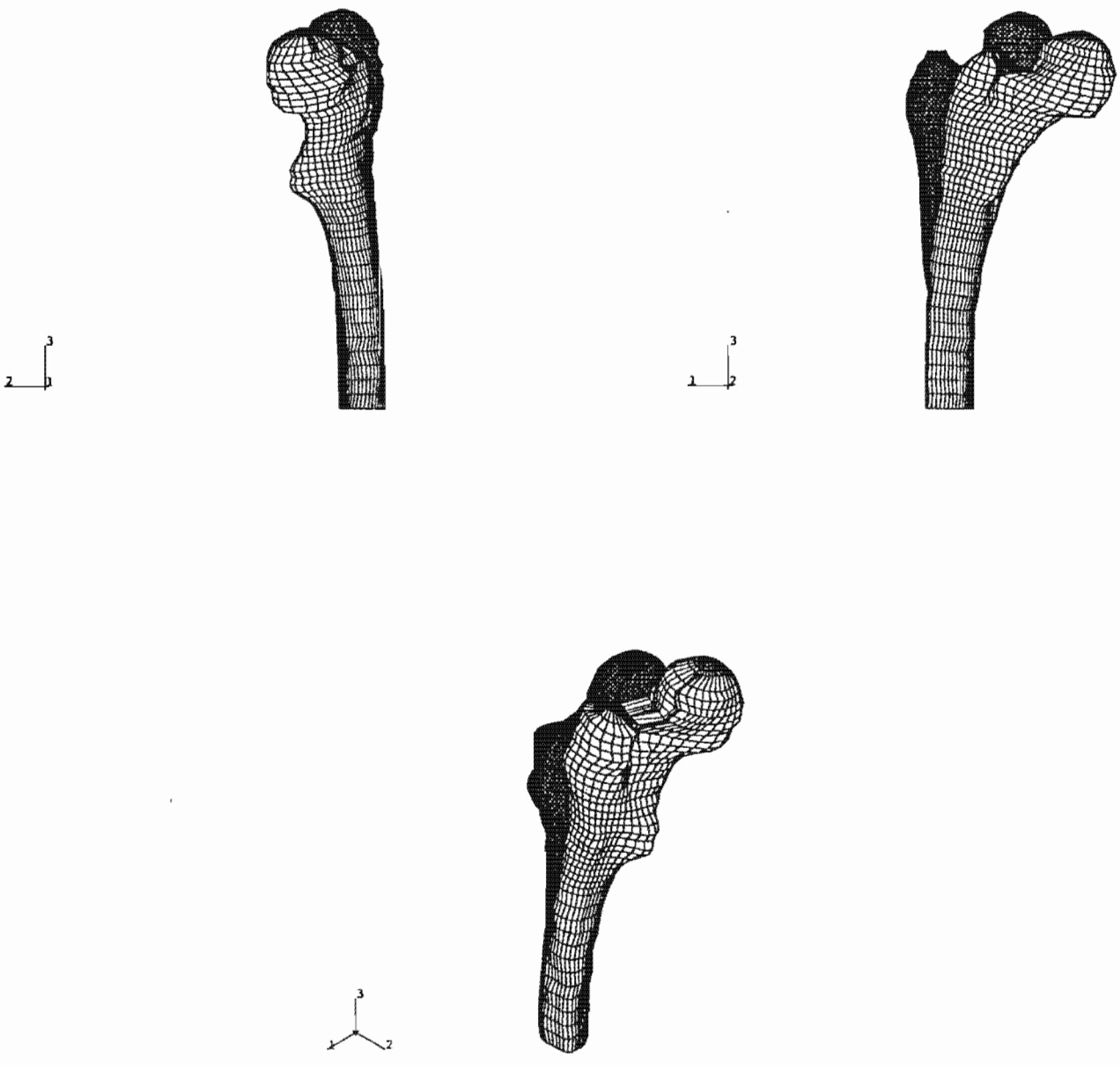

Figure 7.29: Mesh deformation caused by load case one, with the undeformed mesh (dark) in the background.

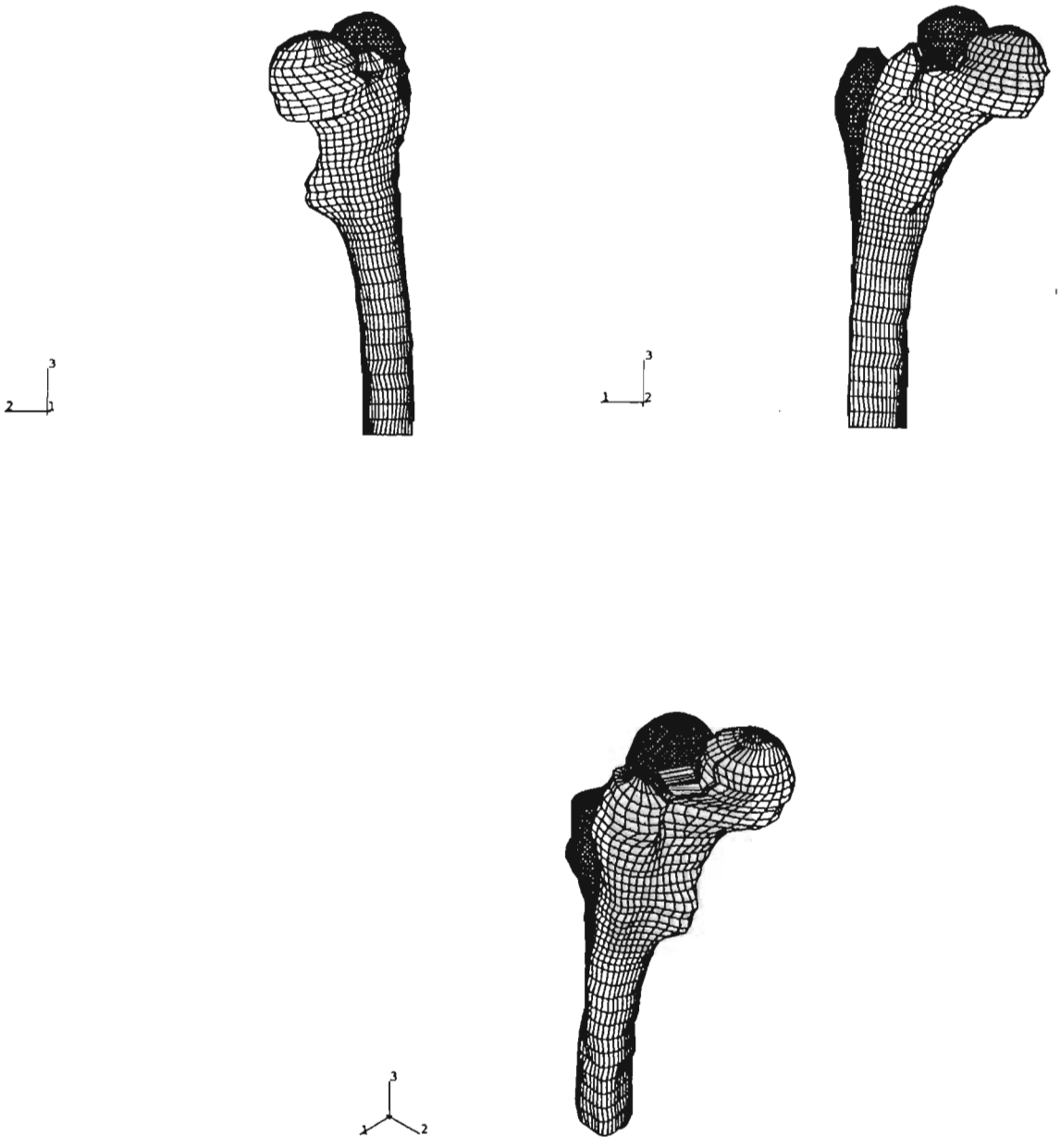

Figure 7.30: Mesh deformation caused by load case two, with the undeformed mesh (dark) in the background.

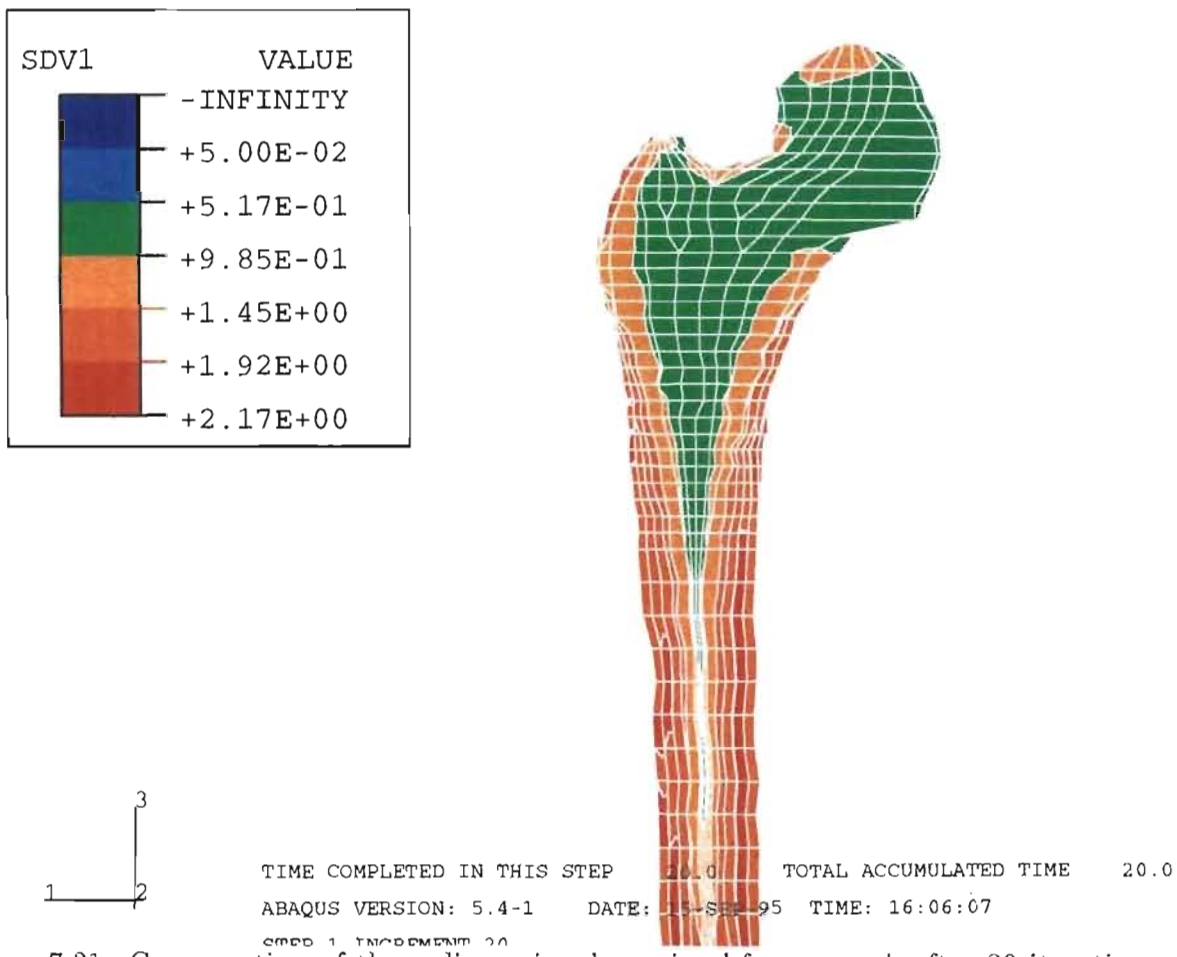

Figure 7.31: Cross-section of three-dimensional proximal femur mesh after 20 iterations. Parameters used are $c_1 = 10\,\mu m/day$, $c_2 = 2\,\mu m/day$, $\rho_i = 1.1\,g/cm^3$.

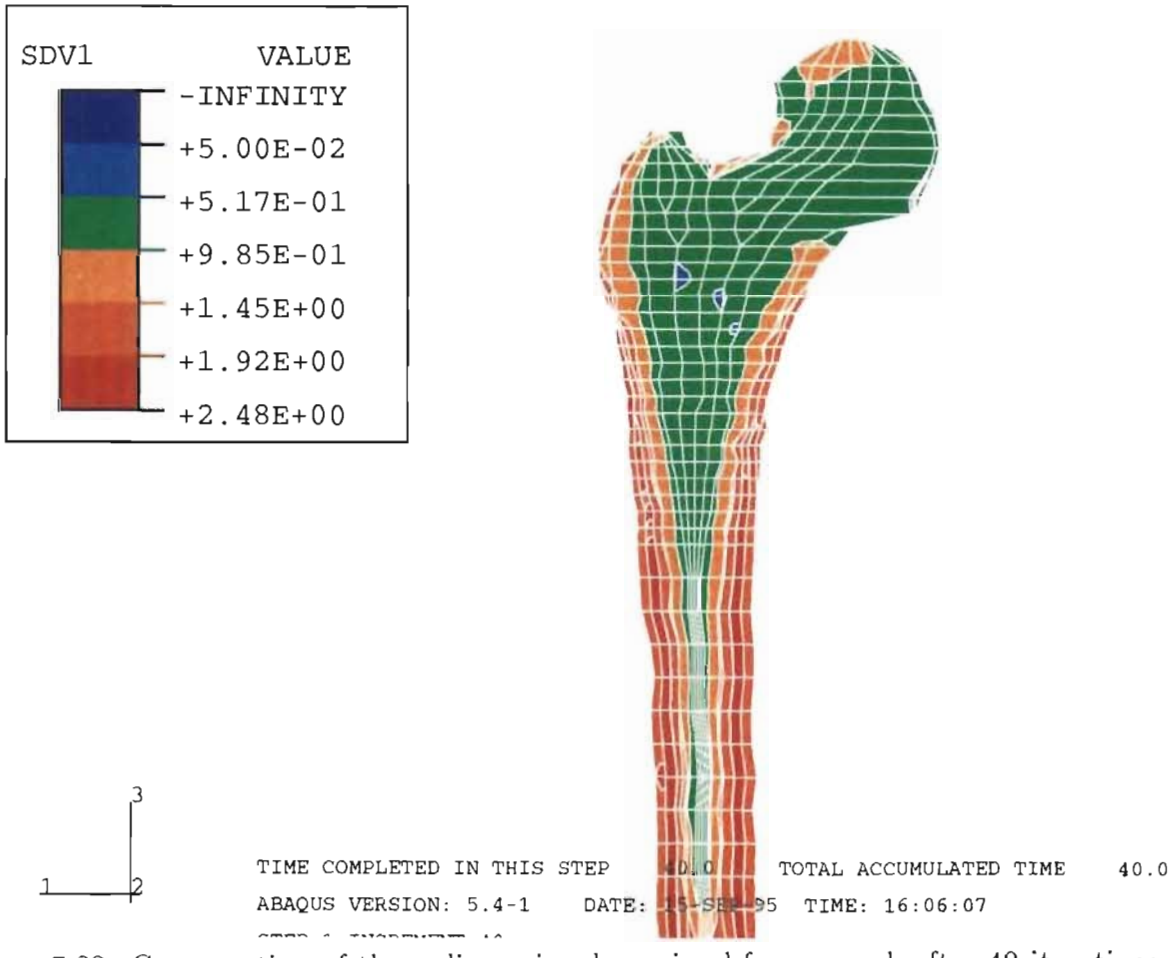

Figure 7.32: Cross-section of three-dimensional proximal femur mesh after 40 iterations. Parameters used are $c_1 = 10\,\mu m/day$, $c_2 = 2\,\mu m/day$, $\rho_i = 1.1\,g/cm^3$.

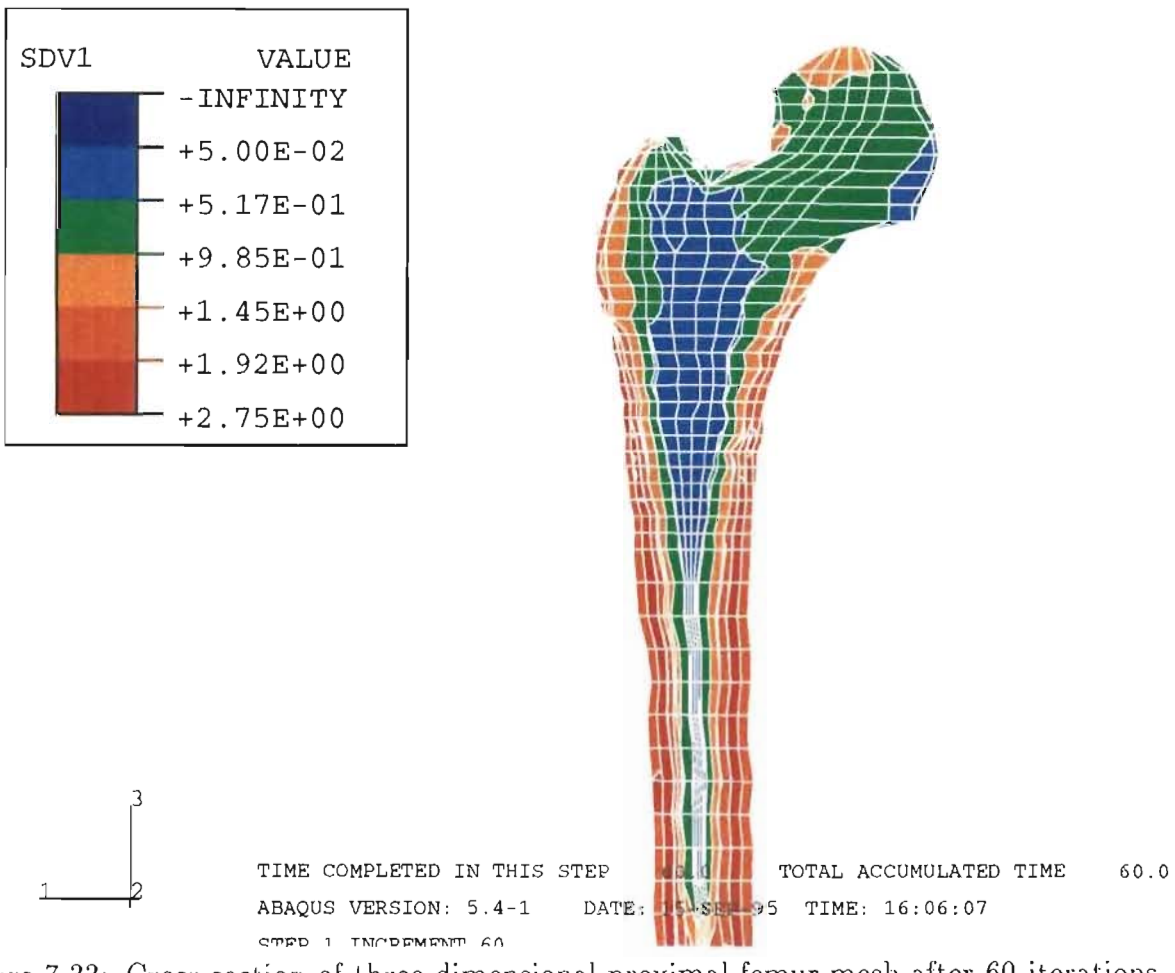

Figure 7.33: Cross-section of three-dimensional proximal femur mesh after 60 iterations. Parameters used are $c_1 = 10\,\mu m/day$, $c_2 = 2\,\mu m/day$, $\rho_i = 1.1\,g/cm^3$.

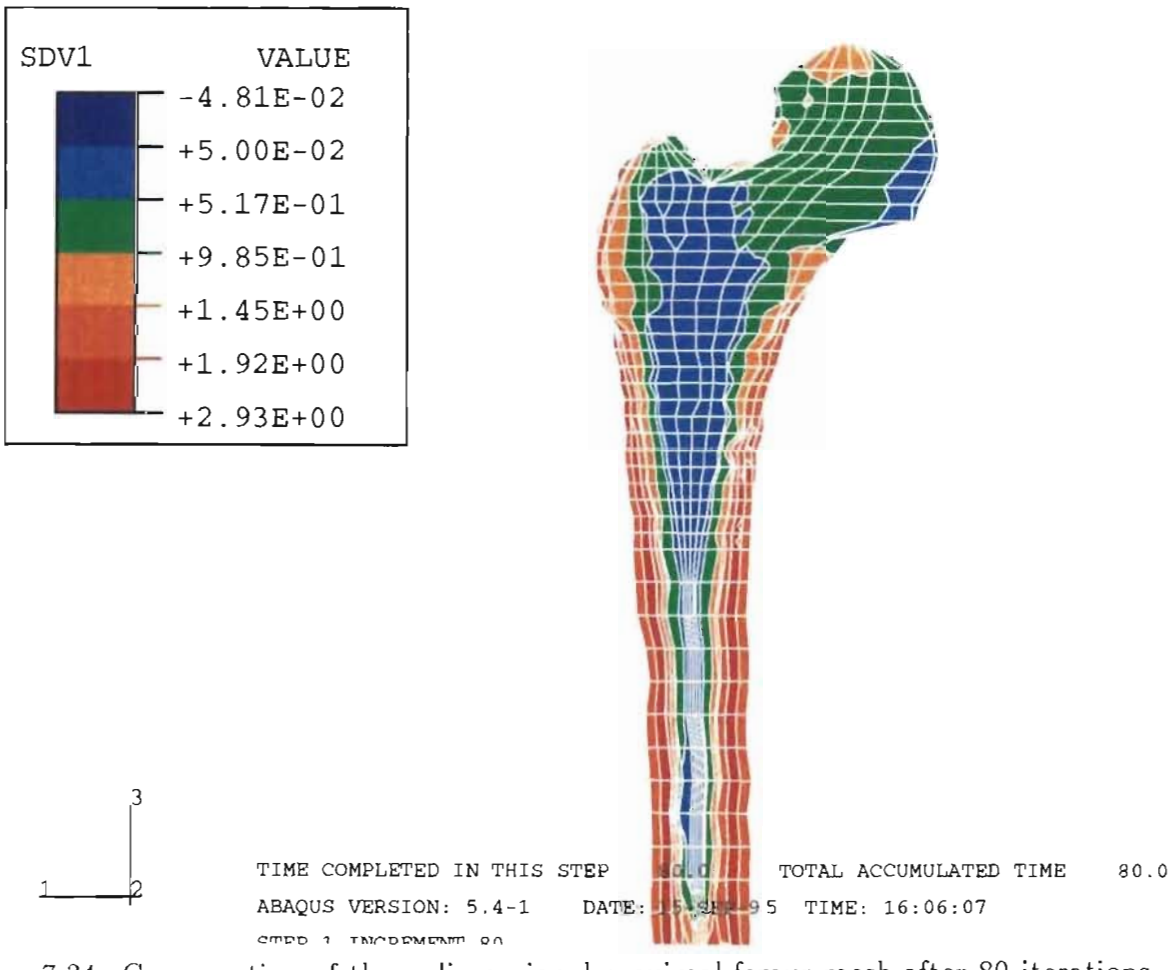

Figure 7.34: Cross-section of three-dimensional proximal femur mesh after 80 iterations. Parameters used are $c_1 = 10\,\mu m/day$, $c_2 = 2\,\mu m/day$, $\rho_i = 1.1\,g/cm^3$.

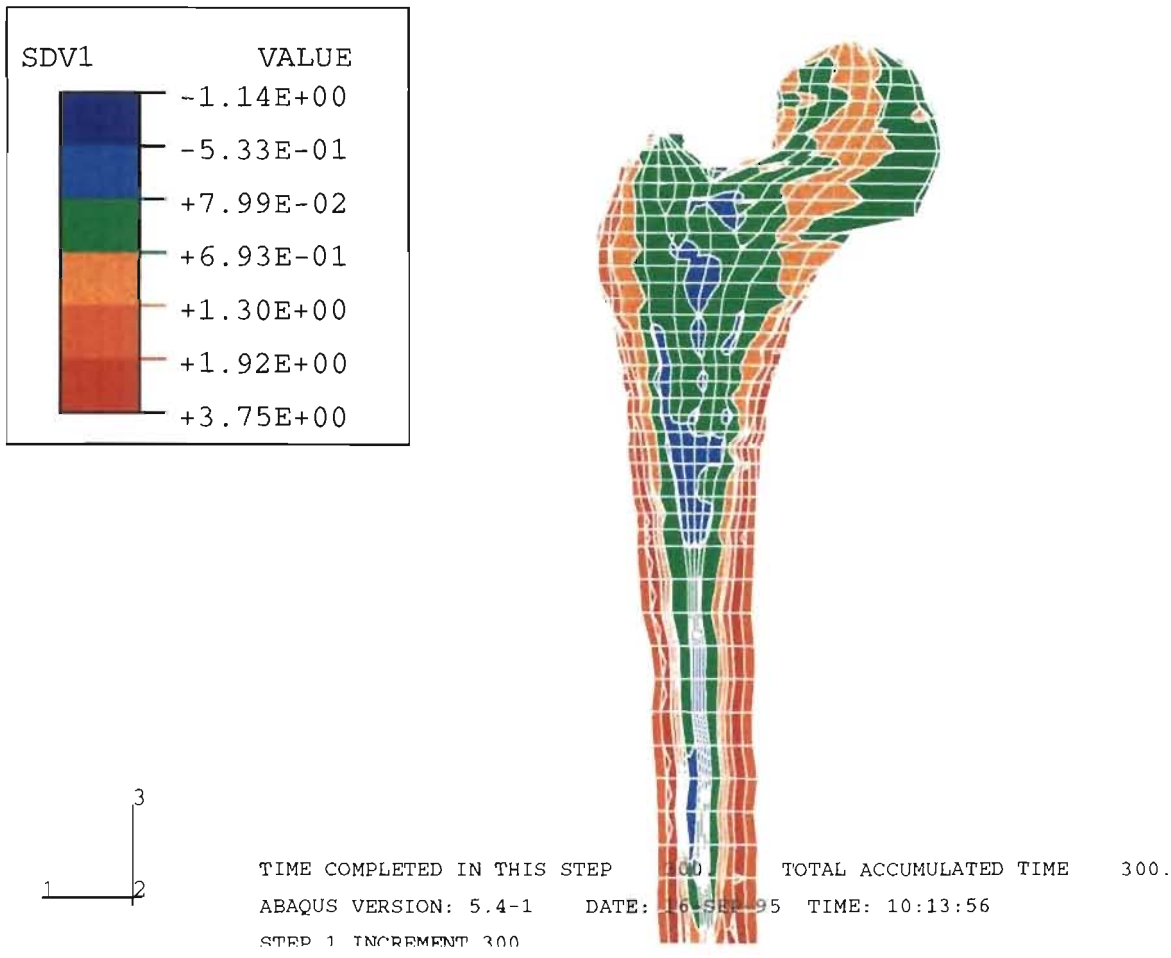

Figure 7.35: Cross-section of three-dimensional proximal femur mesh after 300 iterations. Parameters used are $c_1 = 10\,\mu m/day$, $c_2 = 2\,\mu m/day$, $\rho_i = 1.1\,g/cm^3$.

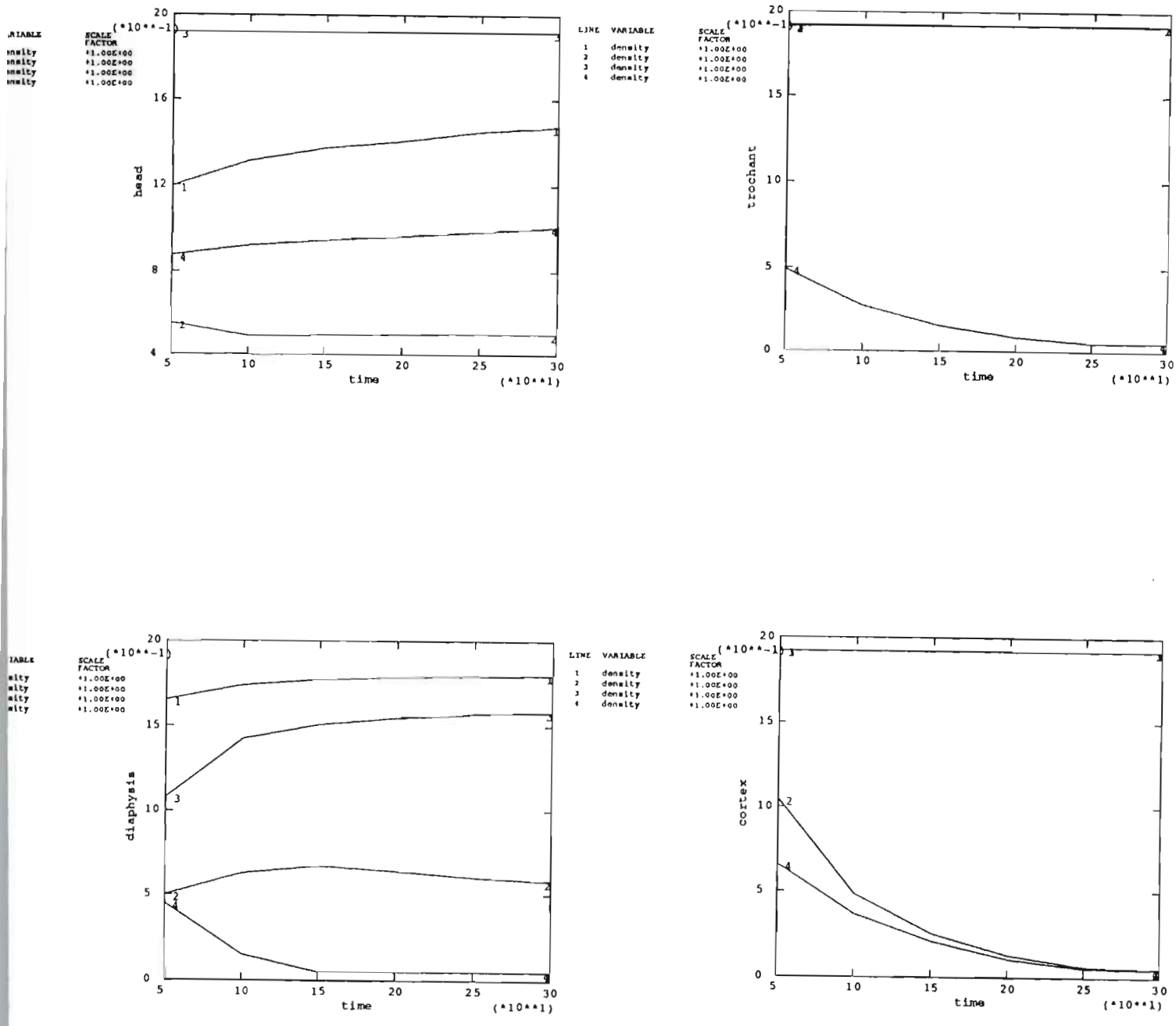

Figure 7.36: History plots of sixteen different elements in the run described above with parameters $c_1 = 10\,\mu m/day$, $c_2 = 2\,\mu m/day$, $\rho_i = 1.1\,g/cm^3$. The elements are grouped into four groups of four elements each, group one representing elements in the femoral head, two elements in the greater trochanter, three in the diaphysis and four in the stem.

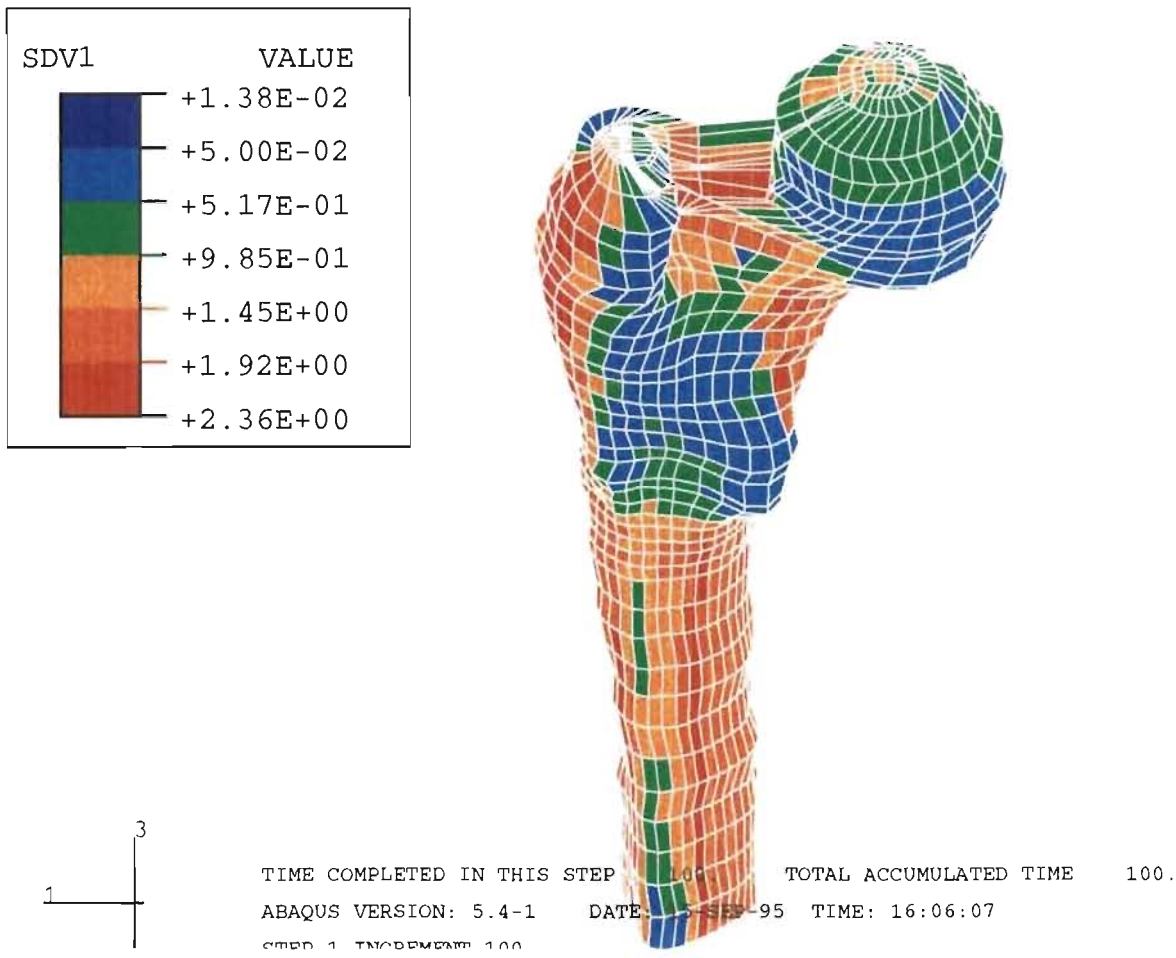

Figure 7.37: Surface density distribution after 100 iterations.

Chapter 8

Discussion and Conclusions

Several different algorithms for bone remodelling have been implemented in both two and three dimensions. The aim of this chapter is to discuss the results, draw conclusions and make suggestions for improvement of the current algorithms, as well as to propose directions for further investigations. As there are a large number of results, the discussion of these follows the same sequence as the presentation of results in Chapter 7.

8.1 Two-Dimensional Implementations

As mentioned in in the introduction to Chapter 7, the two-dimensional density contour plots provide a means of comparing the numerical results with a realistic bone density distribution (see figure 4.6). This Section contains a discussion of the numerous density contour plots presented in section 7.1 as well as the history plots presented in the same section.

8.1.1 Discussion of results obtained with the Stanford model

Effect of a side plate. Figure 7.1 shows the evolution of the density contours with time in a mesh consisting of a front plate as well as a side plate. The most notable feature of this series of contour plots is that, even after 500 iterations, there is no cortical development along the femoral stem. This is because the front plate is shielded from loading by the side plate, which consists of cortical bone and is not permitted to remodel. This shielding depends on the initial density of the front

plate, and it was found that for low densities, there is limited cortical development. Hence the side plate was discarded in all further two-dimensional runs.

Effect of initial density. To establish whether initial density has any effect on the final remodelled density distribution, the final density of the twelve strategically chosen elements shown in figure 7.2 was measured after 500 iterations for initial densities varying from $0.1\,g/cm^3$ to $1.9\,g/cm^3$. These results are depicted by means of line graphs in figure 7.3. The elements are grouped in three groups of four elements each, the first group containing elements from the medial side of the femoral head, the second elements from the lateral side of the head, and the third elements from the femoral stem region. The only elements that show no dependence on initial density are elements 10 and 12 which are situated in the cortical shell of the femoral shaft and retain their cortical density of $\rho = 1.92\,g/cm^3$ throughout. All other elements show a dependence on initial conditions that is smooth, ie. the final density of a particular element varies smoothly with the initial density. For two of the elements (element 1 and 5), the final density decreases as initial density increases, for seven elements (element 2,4,6,7,9 and 11) the final density increases as a function of initial density. For element 3, the final density first increases slightly and then decreases again as the initial density is varied.

As can be seen from this data, the initial conditions play a significant role in this remodelling algorithm. Element 5 exhibited the largest variation of final density as a function of initial density: its density varied by more than $0.6\,g/cm^3$ over the range of initial densities. This corresponds to roughly $\frac{1}{3}$ of the total range of allowed densities ($1.87\,g/cm^3$). Note that the density referred to here as the final density is the density after 500 iterations. This does not preclude further remodelling to occur after 500 increments, it merely provides a reference time. The final density could have been measured after any number of iterations. It will be shown in the discussion of the long-term run that remodelling by no means ceases after 500 iterations.

Density distribution after a large number of iterations. The density contours at several times during a long-term simulation (maximum number of increments = 3000) are shown in figure 7.4. After 100 increments, the density distribution looks physiological in that it bears some resemblence to the radiograph of a proximal femur in cross-section (see figure 4.6). There is a cortical shell surrounding the femoral shaft as well as a trabecular bone distribution in the femoral head that is comparable to the physiological one. After 1000 increments, the trabecular distribution in the femoral head has become irregular, even though the cortex in the shaft is still visible.

Low density regions are specked with small regions of higher density. After 2000 increments, the density distribution looks even more irregular than after 1000, and this does not change much during the last 1000 increments of the analysis. The cortical shell is still visible around the shaft, but some regions of increased density have developed in the shaft. This is because of the resorption that is visible in the femoral head, as the checkered regions of high and lower density trabecular bone transmit some of the load to the femoral shaft cortical shell and some to the region of low density in the medullary shaft. When there is a system of continuous trabecular struts in the femoral head, most of the load is transferred only to the cortical regions in the shaft.

The density history plots of the twelve elements depicted in figure 7.2 are displayed in figure 7.5 and show that out of the twelve elements selected, only one (element 1) has a density different from the minimum allowed density ($0.05\,g/cm^3$) or cortical density ($1.92\,g/cm^3$) after about 1200 iterations. This indicates that the only long-term stable values of density in this algorithm are either the minimum or the maximum allowed densities. The density distribution after 3000 increments in Figure 7.4 seems not to have evolved at all from that after 2000 increments, even though it does not look physiological. Jacobs [47] has shown that even after 3000 increments, the largest change of density between increments is different from zero, hence this steady state is only an apparent steady state.

The results of the three experimental procedures described above have highlighted the weaknesses of the strain energy based algorithm presented by the Stanford group [12] [47], namely the inapplicability of the side plate concept for low initial density simulations, the dependence of the algorithm on the initial conditions and the absence of a long-term steady state. While these are inadequacies that should not be present in such a remodelling algorithm, it must be emphasised that the intermediate density distributions calculated look very similar to the physiological trabecular distribution. The algorithm reaches a physiologically acceptable solution which then turns into a more nonrealistic configuration. Some steps taken to remedy this situation are discussed in Chapter 5, and it will become clear in the discussion in the following Section how these flaws can be at least partially rectified.

8.1.2 Discussion of results obtained with the strain based model

Lengthened femoral shaft. Figure 7.6 shows the stress distribution for an applied bending load for both a short femoral stem as used by Jacobs [48] and an extended femoral stem. In the short stem mesh, the maximum bending stress occurs at the boundary, whereas the bending stress in the lengthened shaft mesh reaches a maximum in the midshaft region and tapers off to a nearly uniform stress distribution at the boundary. The lengthened shaft represents a more realistic model of a long bone such as the femur, since this is a closer approximation to the real geometry. The boundary *in vivo* is the proximal tibia, and stress is transferred from the distal femur to the proximal tibia by axial compression. Hence all subsequent remodelling simulations are carried out using the lengthened femur mesh shown in figure 7.6.

Strain based algorithm with physiologically realistic parameters. Results of an implementation of the strain based algorithm (see Section 5.4) with the parameters $\rho_i = 0.7\ g/cm^3$, $c_1 = 2\,\mu m/day$, $c_2 = 20\,\mu m/day$ are shown in figures 7.7 to 7.10. Figure 7.7 shows some physiological features in that the density increases in both the cortical shell region and the femoral head region where cancellous bone struts are found in figure 4.6. In most regions of the mesh, however, resorption takes place. Note that the maximum density in figure 7.7 is $0.778\,g/cm^3$, which does not exceed the initial density of $0.7\,g/cm^3$ by much. This pattern is continued in figure 7.8, and after 50 iterations (see figure 7.9) shows large patches of resorbed material with a few isolated regions of high density in the vicinity of the femoral shaft. The maximum density in figure 7.9 is $1.52\,g/cm^3$ which means that cortical density has not been reached anywhere. After 150 iterations (see figure 7.10) cortical density has been reached in some small regions, but most of the bone has resorbed to minimum density. The density distribution does not look remotely physiological.

Thus the implementation of the strain based model with double sigmoid remodelling surface velocity function does not work with the parameters determined from a combined pool of knowledge and experimental evidence [37] [63]. As will be shown in further discussion, the algorithm can yield physiological density distributions when the remodelling surface velocities are altered slightly.

Effect of equal remodelling surface velocities. The density evolves differently when one assigns maximal surface remodelling velocities $c = 2\,\mu m/day$ for both resorption and apposition, as shown in figures 7.11 to 7.14. The physiological features of femoral shaft cortex and trabecular struts in the proximal femoral head that start

developing after 10 iterations (see figure 7.11) do not resorb during subsequent iterations, even though cortical density has not been attained anywhere by iteration 100 (see figure 7.13). After 150 iterations, a thin cortical shell has formed on the medial side of the femoral shaft (see figure 7.14) while the trabecular architecture in the femoral head region is retained. The cortical shell on the lateral side of the femural shaft is very thin and this is where this density distributions deviates from the physiological picture. The development of cortical bone on the edges of the femoral shaft can be speeded up by increasing the surface apposition velocity while retaining the surface resorption velocity, as will be demonstrated in further discussions. The results generated from the current set of parameters look promising even though the remodelling surface velocities do not agree with the values gathered experimentally.

Dependence on initial conditions. To assess the dependence on initial conditions of the strain based algorithm, an experiment with the same parameters as above but with an initial density $\rho_i = 1.92\,g/cm^3$ was set up. The results of this run are shown in figures 7.15 to 7.17. Figure 7.15 shows the density distribution after 50 iterations. The bone has resorbed uniformly from cortical density to a density of between $1.31\,g/cm^3$ and $1.43\,g/cm^3$ over almost the entire region. This is because the resorption rate is limited by the maximum surface resorption velocity specified in the double-sigmoid remodelling surface velocity function. If a trilinear remodelling surface velocity as proposed by Jacobs [47] (see figure 4.3) were used, each region would remodel at a different rate. In this model, all regions resorb at the same rate until the remodelling error in some of them reaches the physiological zone shown in figure 5.6, and then they remodel at a different rate than others. This has happened after 150 iterations, as figure 7.16 shows. This density contour plot looks almost identical to the one generated with $\rho_i = 0.7\,g/cm^3$ depicted in fig 7.14. Hence initial conditions do not influence the final density distribution as much as in the remodelling algorithm discussed in the previous section. A history plot of the density in the twelve elements (figure 7.2) shows the uniform decrease in density in all elements until some remodel at different rates than others. Note that some elements have arrived at a density that remains constant in time, ie. a steady state, while the density of others is still changing; the trend of this change indicates convergence to a steady state: the curves are levelling off. After 200 iterations, none of the elements have reached the minimum (resorption) or the maximum (cortical bone) possible density respectively.

Development of physiological structures. Figures 7.18 to 7.21 show the density evolution of the model run with parameters $\rho_i = 1.1\,g/cm^3$, $c_1 = 10\,\mu m/day$, $c_2 = 2\,\mu m/day$, and are included to illustrate the development of physiological structures in the finite element model. The first physiological feature that evolves out of the constant-density bone is the cortex around the femoral shaft, traces of which can already be seen after 20 increments (see figure 7.18). The rest of the bone has resorbed in a uniform fashion to a density between $0.798\,g/cm^3$ and $0.958\,g/cm^3$. After 40 increments, cortical densities have been reached on the medial side of the femoral shaft, and a trabecular strut is beginning to form in the femoral head (see figure 7.19). Some trabecular structure can also be seen to develop in the saddle between the medial and lateral parts of the femoral head. In figure 7.20, which shows the density after 60 increments, cortical bone has formed on both sides of the femoral shaft. The medullary canal is filled with trabecular bone, and the least dense regions are in the mid-epiphysis. The trabecular struts in the medial femural head have grown in density and size. After 80 increments (figure 7.21), the cortex in the femoral shaft as well as the trabecular strut across the femoral head are fully developed. The medullary cavity is filled with bone of density between $0.509\,g/cm^3$ and $0.814\,g/cm^3$. The regions of least density include the edges of the femoral head and part of the greater trochanter. Figure 7.22 shows density history plots of the twelve elements highlighted in figure 7.2; these exhibit density evolution with a general tendency towards resorption even after 200 increments.

Some of the features produced in this remodelling analysis are physiological, like the cortex formed around the femoral shaft and the trabecular distribution in the femoral head, while others, like the cancellous bone in the medullary canal, are not seen in a real bone (see figure 4.6). The latter feature could be due to the inadequacy of the approximation of two-dimensional plane strain. Whether it will vanish in a three-dimensional analysis will be discussed in Section 8.2.

Density distribution after a large number of increments. The results of an experimental run over 3000 increments using the parameters $\rho_i = 1.1\,g/cm^3$, $c_1 = 10\,\mu m/day$, $c_2 = 2\,\mu m/day$ are shown in figures 7.23 to 7.25. Figure 7.23 shows the density distribution after 100 iterations with the well-formed physiological features of the cortex and the trabecular struts in the femoral head as discussed above. This configuration evolves to the density distribution shown in figure 7.24 which retains the basic physiological features of the cortex and the trabecular struts in the medial femoral head. An interesting feature of the element density history plots shown

in figure 7.25 is the change in density evolution at about 600 increments that all elements exhibit. As 3000 increments represents a very long period of remodelling, the timescale in figure 7.25 is compressed somewhat, and this "jump" is made to look more dramatic in than it really is: elements evolve from a low density to a high density or vice versa over a period of 100 increments. Nevertheless the evolution after the 600th increment looks much smoother than before this increment. Most of the results presented above were taken before this jump. The long-term behaviour of this algorithm is more realistic than that of the strain energy based algorithm developed by Jacobs et al. [12] [47] since only four of the twelve monitored elements reach the minimum allowed density. None reach cortical density in the long term. Thus there is proof of the existence of intermediate density steady states for some elements, and the resulting density distribution looks more physiological than that obtained using the strain energy based model.

8.2 Three-Dimensional Implementations

The results discussed in the previous Section showed that, modelling the geometry of the proximal femur using a two-dimensional mesh, some realistic and some non-physiological features are produced. The two-dimensional approach has some limitations that are outlined in Section 4.6, the grossest approximation being the simulation of hoop strains and stresses set up in the cortical shell by using a plane strain constraint. The three-dimensional mesh was designed with the existence of a shell of cortical bone encasing the less dense cancellous bone on the inside in mind, the only complication being that the cortical shell becomes very thin proximally (see Section 6.1). To model the geometry in three dimensions is much more problematic than to mesh the two-dimensional cross-sectional geometry, which can be done using four-noded quadrilateral elements. Some low-order three-dimensional elements such as eight-noded brick elements as well as six-noded wedges were used to construct the mesh in three dimensions (as described in Section 6.1), and the result of these efforts is shown in figure 7.26. Due to the complicated geometry it was unavoidable to have some distorted elements as well as some elements of large aspect ratios and some elements of much larger volume than others. This can be seen when looking at the cross-section of the three-dimensional mesh (see figure 7.31 for example). Since some of the elements in the diaphysis are large in volume compared to elements in the shaft, density contours are not always as smooth as in the two-dimensional mesh, which has a larger number of elements to cover the same cross-sectional area. Also, there

is a discontinuity in the contours whenever a wedge element meets a brick element since the ABAQUS Post-processor uses different procedures to plot contour lines in different types of elements. Even though the three-dimensional approach should guarantee a more valid approximation to the problem, because of the coarseness of the mesh, extracting results out of the three-dimensional density contour plots is not as simple as for the two-dimensional case.

Load application. A further complication that is associated with the three-dimensional setting is the load application, as discussed in Section 6.2. The density contours in figures 7.27 and 7.28 illustrate the different remodelling responses to concentrated and distributed loads, as described in Section 6.3. In the case of a load concentrated over a small area of the femoral head, after 100 remodelling increments, a concentration of cortical bone forms in the center of the medial femoral head (see figure 7.27). In the case of a distributed pressure load, a distribution of trabecular struts similar to those observed in the two-dimensional simulations (see figure 7.21) develops in the femoral head. A cortex in the femoral shaft consisting of high-density bone as well as a medullary cavity are formed identically in both simulations. Hence the density distribution near the load application surface (near-field behaviour) is influenced more than the density further away (far-field behaviour). The remodelling induced by the pressure load actuates a density distribution that is more similar to the physiological density distribution than is the case for the concentrated load, which makes sense because the pelvis exerts a pressure load rather than a concentrated force on the femoral head via the acetabulum of the pelvis bone [55]. Hence in all further analyses presented here, the acetabular load was simulated as a distributed pressure load. The two load cases described in Section 6.2, applied in this manner, produce the displacements shown in figures 7.29 and 7.30 respectively.

Three-dimensional remodelling simulation. Figures 7.31 to 7.35 depict cross-sectional density contours generated by a fully three-dimensional remodelling simulation using the parameters $\rho_i = 1.1\, g/cm^3$, $c_1 = 10\, \mu m/day$, $c_2 = 2\, \mu m/day$. The contour plots are taken after 20, 40, 60, 80 and 300 intervals respectively in order to demonstrate the evolution of physiological features as well as some long-term behaviour of the model. The legend of the density distribution contours for the figures 7.31 to 7.34 is chosen in such a way that dark red represents cortical density and blue represents very low trabecular density. After 20 increments, two thick columns of cortical bone have formed along either side of the stem (see figure 7.31) with a thin region of less dense bone in between. The cortex on the lateral side extends up to

the top of the greater trochanter, which is where the hip abductor force is applied (see Section 6.2). There is some densification at the top of the femoral head as well as in the saddle between the medial and lateral femoral head. After 40 increments, this pattern has changed slightly in that the thickness of the medullary region of low density has increased (see figure 7.32). Figure 7.33 shows the density distribution after 60 increments, and a region of trabecular bone of low density can be seen to have formed in the center of the bone, extending down into the femoral shaft. The cortex is still there, and some resorption has taken place at the medialmost edge of the femoral head. There is a ridge of trabecular bone connecting the top of the femoral head to the cortex in the femoral shaft. In figure 7.34 (remodelling time = 80 increments), the medullary canal has widened further, while all the other features visible in figure 7.33 are still there. The density distribution after 300 increments (see figure 7.35) shows the cortex around a medullary canal of lower density, trabecular struts across the femoral head as well as regions of low density in the center of the bone and at the medialmost side.

The history curves of sixteen elements chosen in a similar fashion as those in figure 7.2 show the evolution of all chosen elements as smooth and having reached a steady state, so it is assumed that the density distribution does not vary much after 300 remodelling increments. Four of the sixteen elements have resorbed completely, five of them have reached cortical density, and the remaining seven an intermediate density. This is very different from the situation depicted in figure 7.5, where eleven out of twelve elements had either resorbed or become cortical. There is evidence of physiological structures such as the cortex of the shaft and the trabecular strut across the femoral head in the cross-sectional view of the three-dimensional mesh, but figure 7.37 shows that the cortex only develops in the anterior-posterior plane section and does not surround the cancellous bone interior completely. There are even some elements visible on the surface of the stem that are resorbed. Also, figure 7.37 shows that no cortex forms in the region of the lesser trochanter. This can be explained by the absence of a muscle attached to the lesser trochanter in the model. In the region of the femoral head, where the distributed pressure load is applied, there is evidence of some densification while no cortical bone is formed. In the real bone, the layer of cortical bone in this region is very thin, so this feature does not mean that the model fails to capture reality. There would be an increase in the area of cortical bone on the bone surface if all muscles attached to the bone *in vivo* were included in the finite element model, but since the muscle attachments are very complex [32], this is very cumbersome to implement.

8.3 Summary

This study is an extension of the work done by the Stanford group, in particular that of Jacobs [47] and Carter [12]. Some of the shortcomings of the model presented by these authors are discussed here, as well as the degree to which these difficulties are improved upon in this study. This is not intended to imply that the work presented by Carter, Jacobs et al. is of inferior quality, but rather that it represents a very useful point of departure for further investigation such as that expounded here. Most of the work in this study is built upon the solid foundation provided by Carter, Jacobs et al.

In order to capture the fundamental mechanical properties of the proximal femur, Jacobs [47] designed a two-dimensional mesh including a front plate and a side plate as depicted in figure 4.7. There are two deficiencies in the design of this mesh; the one is the use of the sideplate as shown in figure 7.1, which, when used with a low initial density, acts as a stress shield and prevents part of the front plate from remodelling. The other is the insufficient stem length which prevents bending stresses from being distributed in a physiological manner, and leads to bending about the pinned boundary (see figure 7.6) for stress distributions in a short and a long stem under bending loads. These deficiencies were easily removed by abandoning the side plate and extending the stem to produce a better bending stress distibution.

Further inadequacies of the proposed strain energy model [47] include the selection of some of the model parameters, such as the remodelling surface velocity and the daily reference stress stimulus (see section 4.2). The remodelling surface velocity parameter c in equation (4.8) has been chosen by Jacobs so that no load at all will result in a remodelling surface velocity of $1\ \mu m/day$. However, using the load cases in his PhD thesis [47], most of the loads induce a remodelling stimulus that is larger than the reference stress stimulus. Because of the linear relation between the remodelling surface velocity $\dot{r}$ and the remodelling error e (see equation (4.8)), the remodelling error produces a surface remodelling velocity that is much larger than $1\ \mu m/day$, and it is doubtful whether this "calibration" of the parameter c is valid. Even when a dead zone as defined in equation (4.9) is added, the remodelling error still induces large remodelling surface velocities. This is because there is no upper limit on the absolute value of remodelling surface velocity: it grows without bound as the remodelling error increases. It is difficult to determine reasonably the width of the dead zone, as no experimental data exist as to how much energy a volume of bone can absorb or release before the remodelling process is initiated. A similar difficulty occurs with determining the reference tissue level stress stimulus ψ_t^*

(see equation (4.7)), which is not a quantity whose value is easily established empirically.

These complications are resolved with the introduction of a strain based remodelling criterion (equation (5.3)) as well as a double sigmoid remodelling surface velocity function (equation (5.5)). The parameters in the strain based model are easier to determine as various experiments using strain gauge techniques (see section 5.1.2) have been carried out to determine remodelling zone width [37] as well as surface remodelling velocity [63] empirically. The double sigmoid remodelling surface velocity function limits the surface remodelling velocity even when the remodelling error is large, thus ensuring that physiologically realistic extreme values are never exceeded.

Another problem with the Stanford remodelling algorithm is that steady-state is never reached in the long term; the density distribution reaches a physiological profile after some time of remodelling, only to end up with an extremely non-smooth and unrealistic distribution after some further remodelling (see figure 7.4). The work done in this study has at least partially solved this problem, as can be observed from figures 7.25 and 7.36, which indicate that not all elements either resorb completely or attain cortical density after a long time, which is the case in figure 7.4. The density distribution in figure 7.24 shows resemblance to the physiological density distribution (figure 4.6), and in the three-dimensional simulation, all elements seem to have reached an equilibrium density after 300 increments (see figure 7.36). This is mainly due to the replacement of the linear remodelling surface velocity (equation (4.8)) function with a double sigmoid one (equation (5.5)), which limits the remodelling surface velocity as discussed in the previous paragraph. Because this is limited, large positive remodelling errors tend to be neutralized slowly, without changing the density so much that large negative remodelling errors occur and vice versa. Hence the whole density evolution is more stable when this approach is utilized.

One point about the three-dimensional model and the finite element mesh in particular is that it is not designed well enough to give information comparable with that provided by the two-dimensional model. This is because the mesh is too coarse and some of the elements are too oblong or too distorted. Also, the loads are simplified greatly, chiefly because studies in the literature such as that presented by Bergmann et al. [8] only investigate the action of one muscle or muscle group, and not the whole musculature acting on the proximal femur. The loads in the two-dimensional model are simplified as well, as only the loads due to the acetabulum and the hip abductor are included.

Even though the model presented here is successful in removing some of the difficulties

experienced with the Stanford model, some peculiarities occurred when the strain based algorithm was implemented. These include the fact that the remodelling velocity parameters c_1 and c_2, when given empirical values provided by Parfitt [63], induced a distinctly non-realistic density distribution with evidence of too much resorption and too little apposition (see figure 7.10). They could be manipulated so that the output looked physiological, however. A possible explanation for this is that when the remodelling error was calculated, only the loading in the current increment was taken into account, whereas real bone has some memory of loading, and loading undergone during previous iterations should also be taken into account when calculating the current remodelling error [54]. As including the bone's loading memory will increase the remodelling stimulus value, it is clear that if the memory is omitted, remodelling error is underestimated, and the net effect will be resorption. Also, daily turnover which occurs in bone [9], and which might affect the net effect of loading as well, was not taken into account.

Another peculiarity was that, even though the two-dimensional long-term simulation eventually reached an equilibrium density distribution, this distribution was reached after a larger change in density of all the monitored elements after about 600 loading increments, as depicted in figure 7.25. The fact that loading and remodelling occur on different timescales could play a role here. A load is applied quasistatically during one increment, whereas the complete remodelling process takes approximately 200 days to complete [9]. Beaupré et al. [6] as well as Cowin [26] have suggested that because of these different time scales, it might be impossible to attain an equilibrium solution to a bone remodelling algorithm such as the one presented here. The shape of the element density history curves for the three-dimensional simulation (figure 7.36), however, suggests that such an equilibrium solution has been reached using this algorithm.

8.4 Conclusion and Motivation for Further Work

In conclusion, the strain based algorithm presented here uses input parameters that can be determined from experiment and have very clear meaning in a physiological context. In particular, the parameters c_1, c_2, ϵ_{rem} and w have been measured and documented in numerous experiments [37] [63]. Other parameters such as m and n are less well documented and thus more difficult to determine in the setting of the strain based algorithm. Physiological density distributions are generated in both two and three dimensions even after a long time of remodelling, while the problem of generating a stable equilibrium

solution has been solved at least partially. A suggestion for further investigation is to do a parametric study involving the parameters c_1, c_2 and n to see how these influence the outcome of long-term iterations.

An obvious oversimplification is the assumption that bone is an isotropic material; further investigation should include the fabric tensor (see section 2.4.3) in order to predict an anisotropic trabecular and density distribution. However, this will again introduce the problem of determining parameter values that are not derivable from physiological considerations.

Another oversimplification is the scaling of strain from the tissue to the continuum level. In this study, it was assumed that the strain is the same on both levels (see equation (5.2)), but according to Ashby and Gibson [2], compressive elastic strain on the continuum level is converted to a superposition of axial and bending strain on the tissue level for a cellular solid like bone. To quantify this superposition correctly is the subject of the literature on homogenization [5] [39], and this is a whole theory that has not been referred to here at all. Including this in the current strain based model is another avenue for further investigation.

A third oversimplification is the assumption that remodelling at a particular increment depends only on the load experienced during that increment. As discussed above, bone has some memory of loading applied in the past, and this could also possibly contribute to the remodelling stimulus [54]. If one included this in the model, perhaps the remodelling surface velocities producing a physiological distribution would correspond to those measured [63].

There are a large number of factors to be taken into account when designing a bone remodelling model, and the focus in this work has been on obtaining physiologically reasonable answers while using parameters that can be determined easily from physiological considerations. Emphasis has also been placed on implementing this model in the correct setting, namely choosing the best possible configuration in two dimensions and constructing a fully three-dimensional finite element mesh. Even though a number of factors influencing bone remodelling have been omitted (examples are strain rate dependence, frequency dependence, remodelling memory etc.), the results generally look physiologically realistic, and exhibit the important property of long-term stability.

Bibliography

[1] Ascenzi, A., Biomechanics and Galileo Galilei, *J. Biomechanics*, **26**, pp95-100 (1993)

[2] Ashby, Gibson, *Mechanics of Cellular Solids*, Chapter 11, Pergamon Press, Oxford, New York, Beijing, Frankfurt, São Paolo, Sydney, Toronto, Tokyo (1988)

[3] Ashman, R.B., Cowin, S.C., Van Buskirk, W.C., Rice, J.C., A continuous wave technique for measurement of the elastic properties of cortical bone, *J. Biomechanics*, **17**, pp349-361 (1984)

[4] Barysenko, M., Besinger, T., *Functional Histology*, published by Little, Brown and Co, Boston (1984)

[5] Beaupré, G.S., Hayes. W.C., Finite element analysis of a three-dimensional open-celled model for trabecular bone, *J. Biomechanical Engineering*, **107**, pp249-256 (1985)

[6] Beaupré, G.S., Orr, T.E., Carter, D.R., An approach for time-dependent bone modeling and remodeling - theoretical development, *J. Orthopaedic Research*, 8, pp651-661 (1990)

[7] Beaupré, G.S., Orr, T.E., Carter, D.R., An approach for time-dependent bone modeling and remodeling - application: a preliminary remodeling simulation, *J. Orthopaedic Research*, 8, pp662-673 (1990)

[8] Bergmann, G., Graichen, F., Rohlmann, A., Hip joint loading during walking and running, measured in two patients, *J. Biomechanics*, **26**, pp969-991, (1993)

[9] Burger, E.H., Notes taken at the workshop on bone cell and tissue mechanics, Coordinated by S.C. Cowin at CISM, Udine, Italy, 10-14 July 1995

[10] Burnett, D.S. *Finite Element Analysis: From Concepts to Applications*, Addison-Wesley, New York (1988)

[11] Carter, D. R., mechanical loading histories and cortical bone remodeling, *Calcif Tissue Int*, **36**, S36-44 (1984)

[12] Carter, D.R., Fyhrie, D.P., Whalen, R.T., Trabecular bone density and loading history: regulation of connective tissue biology by mechanical energy, *J. Biomechanics*, **20** , pp785-794 (1987)

[13] Carter, D.R., Orr, T.E., Fyhrie, D.P., Relationships between loading history and femoral cancellous bone architecture, *J. Biomechanics*, **22**, pp231-244 1989

[14] Chadwick, P. *Continuum Mechanics*, George Allan & Unwin, Norwich (1976)

[15] Charnley, J., Factors in the design of an artificial hip joint, *Proc Instn Mech Engrs*, **181** Pt 3 f (1966-67)

[16] Cook, R.D., Malkus, D.S., Plesha, M.E., *Concepts and Applications of Finite Element Analysis, 3rd Edition*, Wiley & Sons, New York (1989)

[17] Cowin, S.C., Bone remodeling I: theory of adaptive elasticity, *J. Elasticity* **6**, pp313-326 (1976)

[18] Cowin, S.C., Van Buskirk, W.C., Internal bone remodeling induced by a medullary pin, *J. Biomechanics* **11**, pp269-275 (1978)

[19] Cowin, S.C., Van Buskirk, W.C., Surface bone remodeling induced by a medullary pin, *J. Biomechanics*, **12**, pp269-276 (1979)

[20] Cowin, S.C., Hart, R.T, Balser, J.R., Kohn, D.H., Functional adaptation in long bones: establishing *in vivo* values for surface remodeling rate coefficients, *J. Biomechanics*, **18**, pp665-684 (1985)

[21] Cowin, S.C., The relationship between the elasticity tensor and the fabric tensor, *Mechanics of Materials*, **4**, pp137-147 (1985)

[22] Cowin, S.C., Wolff's law of trabecular architecture at remodelling equilibrium, *J. Biomechanical Engineering*, **108**, pp83-88 (1986)

[23] Cowin, S.C., Mehrabadi, M.M., Identification of the elastic symmetry of bone and other materials, *J. Biomechanics*, **22**, pp503-515 (1989)

[24] Cowin, S.C. , Sadegh, A.M. , Luo, G.M., Constitutive equations for the evolution of trabecular architecture, *AMD*-**120**, *pp279-282, 1991 Biomechanics Symposium ASME* (1991)

[25] Cowin, S.C., Sadegh, A.M.,Luo, G.M., An evolutionary Wolff's law for trabecular architecture, *J. Biomechanical Engineering*, **114**, pp129-136 (1992)

[26] Cowin, S.C., Notes taken at the workshop on bone cell and tissue mechanics, Coordinated by S.C. Cowin at CISM, Udine, Italy, 10-14 July 1995

[27] Crowninshield, R.D., Implant design and total hip arthroplasty, *The Art of Total Hip Arthroplasty*, Grune & Stratton (1987)

[28] Currey, J.D., Brear, K., Hardness, Young's modulus and yield stress in mammalian mineralized tissues, *Journal of Materials Science: Materials in Medicine*,1, pp14-20 (1990)

[29] Currey, J.D., Notes taken at the workshop on bone cell and tissue mechanics, Coordinated by S.C. Cowin at CISM, Udine, Italy, 10-14 July 1995

[30] Dalstra, M., Huiskes, R., Odgaard, A., van Erning, L., Mechanical and textural properties of pelvic trabecular bone, *J. Biomechanics*, **26**, pp523-535 (1993)

[31] Dhate, G., Touzot, G., Chapter 5: Numerical Procedures, *The Finite Element Method Displayed*, Wiley (1984)

[32] Dostal, W.F., Andrews, J.G.,, A three-dimensional biomechanical model of hip musculature, *J. Biomechanics*, **14**, pp803-812 (1981)

[33] Field, R.E., Kenyon, C.M., A mathematical analysis for the modeling of trabecular bone, *J. Biomedical Engineering*, **11**, pp384-389 (1989)

[34] Gibson, L.J., The mechanical behaviour of cancellous bone, *J. Biomechanics*, **18**, pp317-328 (1985)

[35] Goodship, A.E., Notes taken at the workshop on bone cell and tissue mechanics, Coordinated by S.C. Cowin at CISM, Udine, Italy, 10-14 July 1995

[36] Gordon, J.E., *Structures or Why Things Don't Fall Down*, Pelican Books, Penguin, London (1978)

[37] Martin, R.B., Burr, D.B., *Structure, Function and Adaptation of Compact Bone Chapter 6: Mechanical Adaptation*, Raven Press, New York (1989)

[38] Harrigan, T.P., Mann, Fabric tensors, *J. Materials Science*, **19**, pp761-767 (1984)

[39] Hollister, S.J., Fyhrie, D.P., Jepsen,K.J., Goldstein, S.A, Application of homogenization theory to the study of trabecular bone mechanics, *J. Biomechanics*, **26**, pp825-839 (1993)

[40] Huiskes, R., Chao, E.Y.S., A survey of finite element analysis in orthopaedic biomechanics: the first decade, *J. Biomechanics*, **16**, pp385-409 (1983)

[41] Huiskes, R., Vroemen, W., A standardized finite element model for routine comparative evaluations of femoral hip prostheses, *Acto Orthop. Belg.*, **52**, pp258-261

[42] Huiskes,R., Weinans,H., Van Rietbergen,B., The relationship between stress shielding and bone resorption around total hip stems and the effects of flexible materials, *Clinical Orthopaedics and Related Research*, **274**, pp124-134 (1992)

[43] Huiskes, R., Hollister, S.J., From structure to process, from organ to cell: recent developments in finite element analysis in orthopaedic biomechanics, *J. Biomechanical Engineering* **115** pp520-527 (1993)

[44] Huiskes, R., Bone remodeling around implants can be explained as an effect of mechanical adaptation, in *Total Hip Revision Surgery*, Raven Press Ltd, New York (1995)

[45] Huiskes, R., Notes taken at the workshop on bone cell and tissue mechanics, Coordinated by S.C. Cowin at CISM, Udine, Italy, 10-14 July 1995

[46] Inman, V.T., Ralston, H.J., Todd, F., *Human Walking*, Ed: JC Lieberman, Williams & Wilkins, Baltimore, London (1981)

[47] Jacobs, C.R., Numerical simulation of bone adaptation to mechanical loading, *PhD Dissertation, Department of Mechanical Engineering, Stanford University*, 1994

[48] Jacobs, C.R., Levenston, M.E., Technical Note: Numerical instabilities in bone remodeling simulations: the advantages of a node-based finite element approach, *J. Biomechanics*, **28** , pp449-459 (1995)

[49] Klein-Nulend, vd Plas, Semeins, Ajubi, Frangos, Nijweide, Burger, Sensitivity of osteocytes to biomechanical stress in vitro, *FASEB Journal*, **9**, pp441-445, (1995)

[50] Lai W.M., Rubin, D., Krempl, E., *An Introduction to Continuum Mechanics*, Pergamon, Oxford, **17** (1978)

[51] Lanyon, L.E., Goodship, A.E., Pye, C.J., MacFie, J.H., Mechanically adaptive bone remodeling, *J. Biomechanics*, **15** , pp141-154 (1982)

[52] Lanyon, L.E., Rubin, C.T., Static vs dynamic loading as an influence on bone remodeling, *J. Biomechanics*, **17**, pp897-905 (1984)

[53] Lanyon, L.E., Functional strain as a determinant for bone remodeling, *Calcif Tissue Int*, **36**:S56-S61 (1984)

[54] Levenston, M.E., Beaupré, G.S., Jacobs, C.R., Carter, D.R., The role of loading memory in bone adaption simulations, *Bone*, **15**, pp177-186 (1994)

[55] Li, G., Genda, E., Sakamoto, M., Chao, E.Y.S., Surface pressure distribution in articular joint under static load, *BED-28, 1994 Advances in Bioengineering*, pp139-140, ASME (1994)

[56] Lipschutz, S., Theory and Problems of Linear Algebra, *Outline Series in Mathematics*, McGraw Hill, London (1987)

[57] Lubuma, M.S., Introduction to Sobolev Spaces, *National Mathematical Centre Abuja - Nigeria* (1989)

[58] Marti, J.T., *An Introduction to Sobolev Spaces and Finite Element Solutions of Boundary Value Problems*, Academic Press, London(1986)

[59] Martin, R.B., The effects of geometric feedback in the development of osteoporosis, *J. Biomechanics*, **5**, pp447-455 (1972)

[60] Martin, R.B., porosity and specific surface of bone, *CRC Critical Reviews in Biomedical Engineering*, pp179-222, CRC Press, Boca Raton, FL (1984)

[61] Müller, M.E., Lessons of 30 years of total hip arthroplasty, *Clinical Orthopaedics and Related Research* , **274**, pp12-21, (1992)

[62] Noble, P.C., Scheller, A.D., Tullos, H.S., Levy, R.N., Turner, R.H., Applied design criteria for total hip prostheses, *The Art of Total Hip Arthroplasty*, Grune & Stratton (1987)

[63] Parfitt, A.M., The cellular basis of bone remodelling: the quantum concept reexamined in the light of recent advances in cell biology of bone, *Calcif Tissue Int*, **36**:S37-S45 (1984)

[64] Pauwels, F., *Biomechanics of the Locomoter Apparatus*, Springer, Berlin 1980

[65] Perlis, S., *Theory of Matrices*, Addison-Wesley, Reading (Massachusetts), (1958)

[66] Pollack, S.R., Petrov, N., Salzstein, R., Brankov, G., Blagoeva, R., Anatomical model for streaming potentials in ostons, *J. Biomechanics*, **17**, pp627-636 (1984)

[67] Poss, Robertson, Walker, Reilly, Ewald, Thomas, Sledge, *Non-Cemented Total Hip Arthroplasty Ch 30: Anatomic Stem Design for Press-Fit and Cemented Application*, ed: R. Fitzgerald Jr, Raven Press, New York (1988)

[68] Roesler, H., The history of some fundamental concepts in bone biomechanics, *J. Biomechanics*, **20**, pp1025-1034 (1987)

[69] Rubin, Lanyon, L.E., Limb mechanics as a function of speed and gait: A study of functional strains in the radius and tibia of horse and dog, *J Experimental Biology*, **101**, pp187-211 (1982)

[70] Rubin, C.T., Lanyon, L.E., Regulation of bone formation by applied dynamic loads, *J. Bone & Joint Surg*, 66A(3) pp897-905 (1984)

[71] Simo, J.C., Ju, J.W., Strain and stress based continuum damage formulations, *Int.J.Solids Struct.*, **23** pp821-869 (1987)

[72] Starkebaum, W.S., Pollack, S.R., Korostoff, E., Microelectrode studies of stress-generated potentials in four-point bending of bone, *Journal of Biomedical Materials Research*, **13**, pp729-751 (1979)

[73] Turner, C.H., Yield behaviour of bovine cancellous bone, *J. Biomech. Eng.*, **111**, pp256-260 (1989)

[74] Turner, C.H.,Cowin, S.C., Rho, J.Y. ,Ashman, R.B , Rice, J.C., The fabric dependence of the orthotropic elastic constants of cancellous bone, *J. Biomechanics*, **23**, pp549-561 (1990)

[75] Van Rietbergen, B., Weinans, H., Huiskes, R., Odgaard, A., A new method to determine trabecular bone elastic properties and loading using micromechanical finite element models, *J. Biomechanics*, **28**, pp69 (1995)

[76] Van Rietbergen, B.,Huiskes, R., Weinans, H., Odgaard, A., Kabel, J., The role of trabecular architecture in the anisotropic mechanical properties of bone, *Proceedings of Workshop Coordinated by S.C. Cowin at CISM*, Udine, Italy, 10-14 July 1995

[77] Turner, C.H., On Wolff's law of trabecular architecture, *J. Biomechanics*, **.25** pp1-9 (1992)

[78] Weinans, H., Huiskes, R., Grootenboer, H.J., The behaviour of adaptive bone-remodeling simulation models, *J. Biomechanics*, **25** , pp1425-1441 (1992)

[79] Weiss, L. , *Cell and Tissue Biology: A Textbook of Histology. (Sixth Edition.)*, Urban & Schwarzenberg, Baltimore, Munich (1991)

[80] Williams, Lissner, *Biomechanics of Human Motion (2nd ed)*, Edited by LeVeau, Saunders Co, Philadelphia, London, Toronto (1977)